
THE UNIVERSITY *of* EDINBURGH


# Synthesis, Structure and Properties of High Pressure and Ambient Pressure Ternary Vanadium Oxides

**Mikael Markkula**

**For the degree of Doctor of Philosophy**

**School of Chemistry**
**University of Edinburgh**

**2013**

# Abstract

Transition metal oxides have been extensively studied during past decades. The purpose of this research was to synthesize new or little characterised transition metal oxides using high-pressure/high-temperature (HPHT) techniques. Various ternary vanadium oxides have been synthesised at ambient and high pressure conditions. All compounds have been studied by neutron and laboratory X-ray powder diffraction and magnetisation measurements. In some cases resistivity and synchrotron X-ray powder diffraction measurements were also carried out.

The $MnVO_3$ perovskite containing localized $3d^5$ $Mn^{2+}$ and itinerant $3d^1$ $V^{4+}$ states has been synthesised at 8 GPa and 1100°C. $MnVO_3$ crystallises in *Pnma* space group ($a$ = 5.2741(6) Å, $b$ = 7.4100(11) Å, and $c$ = 5.1184(8) Å at 300 K) and is metallic at temperatures of 2 – 300 K and at pressures of up to 67 kbar. Synchrotron X-ray powder diffraction study on the combined sample of several high pressure products showed slight variation in the stoichiometry of $MnVO_3$. Incommensurate Mn spin order was discovered in the neutron powder diffraction measurements, which reveal a (0.29 0 0) magnetic vector below the 46 K spin ordering transition, and both helical and spin density wave orderings are consistent with the diffraction intensities. Electronic structure calculations show large exchange splittings of the Mn and V 3d bands, and ($k_x$ 0 0) crossings of the Fermi energy by spin up and down V 3*d* bands may give rise to Ruderman-Kittel-Kasuya-Yosida coupling of Mn moments, in addition to their superexchange interactions.

The new compound $CoVO_4$ has been discovered in a high pressure synthesis experiment. Magnetic susceptibility measurement, synchrotron X-ray and neutron powder diffraction studies were carried out. Refinements of the synchrotron X-ray and neutron data show $CoVO_4$ to crystallise in space group *Pbcn* ($a$ = 4.5012(2) Å, $b$ = 5.5539(3) Å, and $c$ = 4.8330(2) Å at 300 K (synchrotron X-ray data)). The magnetic susceptibility measurement reveals that $Co^{3+}$ is most likely in a low spin state in $CoVO_4$.

Monoclinic brannerite type $CoV_2O_6$ was synthesised in ambient pressure. Neutron powder diffraction measurements were carried out and an antiferromagnetic order with an $a$ x $b$ x $2c$ supercell was observed below $T_N$ = 15 K. High spin $Co^{2+}$

moments of magnitude 4.77(4) $\mu_B$ at 4 K lie in the *ac* plane and are ferromagnetically coupled within chains of edge-sharing $CoO_6$ octahedra parallel to *b* axis. No structural transition is observed down to 4 K, but a magnetostriction accompanying antiferromagnetic order at $T_N$ = 15 K was discovered. A field-induced 1/3 magnetisation plateau and corresponding changes in the magnetic structure were studied by carrying out neutron powder diffraction measurements at 2 K in applied magnetic fields of 0, 2.5 and 5.0 T. Three collinear magnetic phases were observed as field increases; the above antiferromagnetic state with propagation vector (0 0 ½), a ferrimagnetic (⅓ 1 ⅓) phase, and a (0 0 0) ferromagnetic order. $Co^{2+}$ moments of 4.4 - 5.0 $\mu_B$ have a large orbital component and are aligned close to the *c*-axis direction in all cases. Spin-lattice coupling leads to a magnetostriction and volume expansion as field increases. The ferrimagnetic phase accounts for the previously reported 1/3 magnetisation plateau, and demonstrates that monoclinic $CoV_2O_6$ behaves as an accidental triangular antiferromagnetic lattice in which further frustrated orders may be accessible.

Orthorhombic columbite-type $NiV_2O_6$ and $CoV_2O_6$ compounds were synthesised at 6 GPa and 900°C. Metamagnetism and magnetic transitions were found in magnetic measurements. Powder neutron diffraction studies in zero and applied field were carried out. Both compounds were refined in space group *Pbcn* and the following lattice parameters were obtained at 300 K, $CoV_2O_6$: *a* = 13.4941(20) Å, *b* = 5.5736(9) Å, and *c* = 4.8082(8) Å and $NiV_2O_6$: *a* = 13.3725(17) Å, *b* = 5.5344(7) Å, and *c* = 4.8162(7) Å. Neutron powder diffraction studies in zero field did not reveal any magnetic peaks for either of the compounds but magnetic order emerges in applied fields between 1 and 4 T.

# Declaration

I declare that this thesis was composed by me and the work contained herein is my own except where stated otherwise in the text. This work has not been submitted for any other degree or professional qualification. Prior to submission some work reported in this thesis has been published elsewhere as listed in the Appendix.

15.7.2013 Mikael Mankkula

# Acknowledgements

First and foremost I would like to thank my supervisor Professor Paul Attfield for all his guidance and encouragement during these three years. I was fortunate to have a very experienced and knowledgeable supervisor.

The members of the Attfield group have contributed considerably to the progress of my studies. I am grateful to Jenny for teaching me how to do high pressure synthesis, Mark for teaching how to use GSAS and X-ray diffractometer, Angel for helping with the experiments at ILL, ESRF and ISIS and with several software and magnetic structure related problems and Anya for teaching how to do resistivity and magnetisation measurements.

I am thankful to Dr. Clemens Ritter, Dr. Pascal Manuel and Dr. Winfried Kockelmann for providing help with the data collection at the ILL and ISIS respectively.

I would also like to acknowledge EPRSC for providing me with the funding for these studies.

# Contents

# Chapter 1. Introduction

## 1.1. Transition metal oxides

Transition metal oxides have been extensively studied during past decades. The unusual electric and magnetic properties of transition metal oxides are due to the unique nature of the outer d electrons. Transition metal oxides crystallize in a variety of structures, the metal-oxygen bonding varying anywhere from nearly ionic to metallic. Thus both metallic and insulating behaviour exist among transition metal oxides. The useful and interesting properties of transition metal oxides include multiferroics, ferroelectricity, ionic and spin polarized conductivity, colossal magnetoresistance and superconductivity. Transition metal oxides are generally very durable due to the strongly bonded, extended structures. Intrinsic and extrinsic defects play an important role in the properties of transition metal oxides [1,2].

## 1.2. Magnetic properties of transition metal oxides

### 1.2.1. Magnetic susceptibility

Oxides with positive magnetic susceptibility are called paramagnetic, while those with negative magnetic susceptibility are called diamagnetic. Dilute paramagnetic oxides generally follow the Curie law

$$\chi_M = \frac{M}{H} = \frac{C}{T}$$

Equation 1.1.

where M is the magnetization, H the magnetic field, $\chi_M$ the molar susceptibility and C the Curie constant. When interaction between atomic moments is present, giving rise to an internal field in the oxide, the susceptibility at high temperatures is generally described by the Curie-Weiss law

$$\chi_M = \frac{C}{T - \theta}$$

Equation 1.2.

where θ denotes a Weiss temperature. The sign of θ depends on the nature of magnetic interaction (ordering): ferromagnetic compounds have positive and antiferromagnetic negative θ. Both the orbital magnetic moment and electron spin contribute to the magnetic properties except in the case of the quenching of the orbital moment which occurs due to the inhomogeneous crystal field interacting with the smaller metal cation's d orbitals.

### 1.2.2. Magnetic ordering

Magnetism in transition metal oxides is considerably more complex than in isolated atoms because of the interaction (coupling) between atomic moments. Electron spins can order ferromagnetically or antiferromagnetically below Curie and Neel temperatures respectively.

A pair of electrons of like spin, localized on an atom, is lower in energy than a pair with opposite spin by an amount called the intra-atomic exchange energy. This phenomenon is called exchange [1].

#### 1.2.2.1. Exchange interactions

Exchange interactions are electrostatic interactions, arising because charges of the same sign cost energy when they are close together and save energy when they are apart [3]. One can distinguish two classes of exchange. Direct exchange occurs between the moments of atoms that are close enough to have significant overlap of their wave functions: exchange coupling is strong but decreases rapidly with the increasing interatomic distance. In indirect exchange the moments couple over relatively large distances. It can act through an intermediary nonmagnetic ion (superexchange) or through itinerant electrons (RKKY coupling).

Superexchange generally occurs in insulators. If the half-filled orbitals of the cations are connected at 90 degrees to the bridging non-magnetic anion or cannot overlap well with the same intermediate anion orbital, the interaction is usually

ferromagnetic. In the case of a good overlap an antiferromagnetic interaction occurs [1].

Double exchange differs from superexchange by electrons moving between the positive ions via the intermediate ligand. This results in metallic behaviour [1].

RKKY (Ruderman, Kittel, Kasuya, and Yoshida) coupling is important in metals. A localized magnetic moment spin-polarizes the conduction electrons and this polarization in turn couples to a neighbouring localized magnetic moment. The exchange interaction is thus indirect because it does not involve direct coupling between magnetic moments. The interaction is long range and has an oscillatory dependence on the distance between the magnetic moments. Hence depending on the separation it may be either ferromagnetic or antiferromagnetic. RKKY interaction is also called itinerant exchange [3].

#### 1.2.2.2. Types of magnetic ordering

##### a) Ferromagnetism

A ferromagnetic solid is spontaneously magnetized even in the absence of the magnetic field. To maximize its magnetostatic energy, a crystalline ferromagnet divides into domains that are spontaneously magnetized nearly to saturation. The moment of each domain, however, is oriented so as to produce a zero net moment. An external field changes the size of the domains, enlarging those of favourable orientation at the expense of others, which results in net resultant (Figure 1.1). The important characteristic of ferromagnets is the hysteresis in magnetization. With increasing temperature, the thermal energy increases, becoming comparable to and eventually exceeding the exchange energy. Spontaneous magnetization thus decreases with temperature and disappears at the Curie temperature. Above Curie temperature an ideal ferromagnet becomes a paramagnet obeying the Curie-Weiss law [1].

##### b) Antiferromagnetism

Antiferromagnetism, like ferromagnetism, is characterized by the long-range ordering of the identical spontaneous moments. But since the moments of

neighbouring atoms are exactly opposed, there is no overall spontaneous magnetization (Figure 1.1). Below Neel temperature an antiferromagnet can be regarded as consisting of two identical interpenetrating sublattices with the result that the spins of one sublattice are opposed to those of the other. Most antiferromagnets are insulating solids, but antiferromagnetism is known among metals and alloys as well. Above Neel temperature the antiferromagnetic materials become paramagnetic [1]. In canted antiferromagnets the direction of the magnetic moments in sublattices are not antiparallel but canted (Figure 1.1).

### c) Ferrimagnetism

Ferrimagnetism requires two or more chemically different magnetic species, which occupy two kinds of lattice site, producing two sublattices, A and B. The moments of ions in each sublattice are ferromagnetically coupled, but the coupling between the moments of A and B is antiferromagnetic (Figure 1.1). Since the net moments of A and B are different, there is a resultant spontaneous magnetization [1].

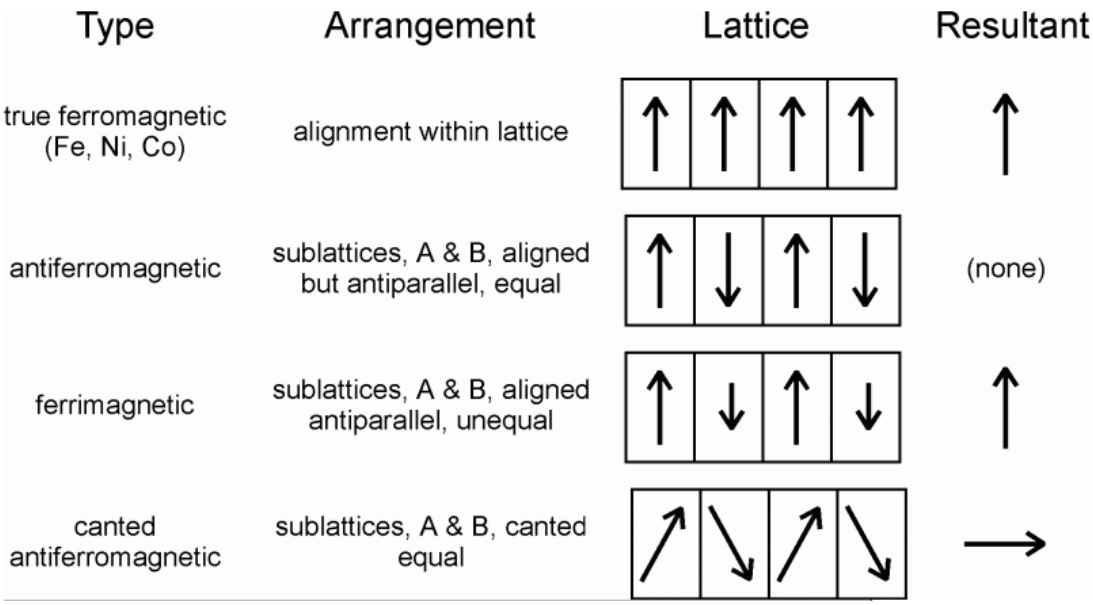


**Figure 1.1.** Different types of magnetic ordering

### d) Incommensurate magnetism

The direction of the moments can sometimes be periodically modulated. When the modulation period is unrelated to the underlying periodicity of the lattice, the structure is called incommensurate. Helical, cycloidal and helicoidal orderings (Figure 1.2) are examples of this magnetic structure type. The magnitude of the moment rather than its direction can sometimes be periodically modulated. This type of structure is called sinusoidally modulated (Figure 1.2) [4].

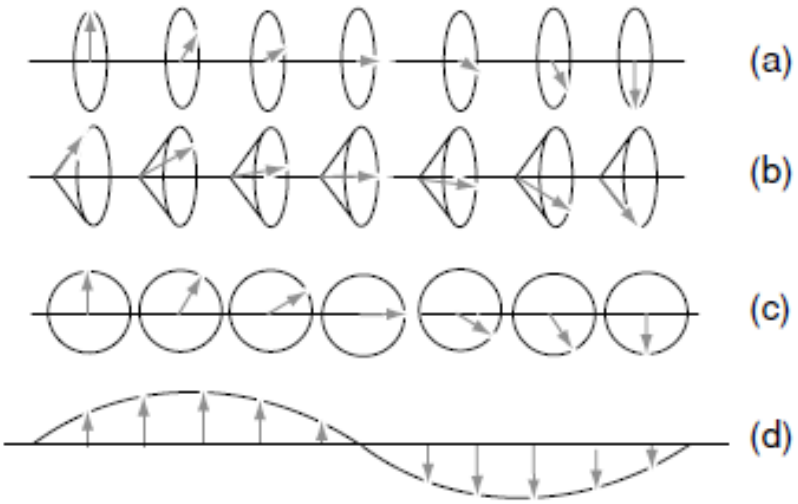


**Figure 1.2.** Some incommensurate magnetic structures: (a) helical, (b) cycloidal, (c) helicoidal and (d) sinusoidally modulated. Only (b) has a net ferromagnetic moment.

## 1.3. Further magnetic phenomena

### a) Low dimensional magnetism

In low-dimensional magnets the interaction between the metal centres is not equal in the three directions but may be confined to one or two directions. Low-dimensional magnetic oxides attract an increasing interest from the scientific community because of their peculiar magnetic properties related to their crystalline

structure. Low dimensional magnets are also interesting in terms of applications: e.g. in the field of high density magnetic recording and spin-electronic devices. Their structure is usually composed of linear magnetic chains (1-dimensional) or planes (2-dimensional). Consequently, such compounds exhibit unusually strong magnetic anisotropies and stepped magnetization variations corresponding to magnetic field-induced transitions [5].

A one-dimensional line of spins is known as a spin chain. The individual spins can be constrained to lie parallel or antiparallel to a particular direction (Ising spins), or may be free to point anywhere in a fixed plane (XY spins) or be free to point in any direction (Heisenberg spins). Spin chains can be approximately realized in crystals, if the crystal structure is such so as to keep the chains reasonably far apart. The single ion anisotropy due to the crystal field may lead to the magnetic moments behaving as Ising spins, XY spins, Heisenberg spins or somewhere in between [3].

### b) Magnetoresistivity

The change in resistance of a material under an applied magnetic field is known as magnetoresistance. It is a technologically useful quantity because magnetoresistive sensors are extensively used in applications. Colossal magnetoresistivity (CMR) is a property of some materials, mostly manganese-based perovskite oxides (e.g. $La_{1-x}Sr_xMnO_3$) that enables them to change their electrical resistance up to 99 % in the presence of a magnetic field. These materials are used extensively in the read heads in modern hard drives and magnetic sensors.

### c) Frustrated magnets, spin liquids and spin glass

Frustrated magnets are materials in which localized magnetic moments, or spins, interact through competing exchange interactions that cannot be simultaneously satisfied, leading to a large degeneracy of the system's ground state. A triangle of Ising spins (meaning the only possible orientations of the spins are "up" and "down"), which interact antiferromagnetically, is a simple example for frustration. In the ground state, two of the spins can be antiparallel but the third one cannot. This leads to an increase of possible orientations (six in this case) of the spins in the ground state, enhancing fluctuations and thus suppressing magnetic ordering.

Under certain conditions magnetic frustration can lead to the formation of fluid-like states of matter, so-called spin liquids, in which the constituent spins are highly correlated but still fluctuate strongly down to a temperature of absolute zero. The fluctuations of the spins in a spin liquid can be classical or quantum and show remarkable collective phenomena such as emergent gauge fields and fractional particle excitations. This exotic behaviour is now being uncovered in the laboratory, providing insight into the properties of spin liquids and challenges to the theoretical description of these materials [6]. The state is referred to as a "liquid" as it is a disordered state in comparison to a ferromagnetic spin state, much in the way liquid water is in a disordered state compared to crystalline ice. However, unlike other disordered states, a quantum spin liquid state preserves its disorder to very low temperatures.

A spin glass is a disordered magnet with frustrated interactions, characterized by a random, yet cooperative, freezing of spins at a well-defined temperature $T_f$ (the freezing temperature), below which a metastable frozen state appears without the usual magnetic long-range ordering. Above the spin glass transition temperature, the spin glass exhibits typical magnetic behaviour. If a magnetic field is applied as the sample is cooled to the transition temperature, magnetization of the sample increases as described by the Curie law. Upon reaching $T_f$ (the freezing temperature), the sample becomes a spin glass and further cooling results in little change in magnetization. The randomness inherent in a spin glass is important, but equally important is the presence of competing interactions. The distribution of distances between moments in a random-site spin glass leads to competing interactions because the interactions are of RKKY-type and therefore their sign (ferromagnetic or antiferromagnetic) depends on the distance between the spins. Another contributing feature is the magnetic anisotropy, due to single-ion anisotropy or Dzyaloshinsky-Moriya interactions [3].

### e) Magnetostriction

Magnetostriction is the deformation of a material body when it is magnetized, either when crossing down the magnetic ordering temperature or when a magnetic field is applied. Magnetostriction is also observed in the paramagnetic regime, and is useful when we want to remove exchange effects, leaving only the crystal electric field effect. Magnetostriction occurs in all pure substances. However, even in strongly magnetic substances, the effect is usually small [7].

### f) Pauli paramagnetism

In metals the paramagnetism of the conduction electrons is called Pauli paramagnetism or weak spin paramagnetism. The conduction electrons each have a spin magnetic moment of one Bohr magneton. One would therefore expect them to make a sizable paramagnetic contribution. This does not happen, however, because the conduction electrons of a metal occupy energy levels in such a way that an applied field can reorient the spins of only a very small fraction of the total number of electrons. The resulting paramagnetism is very weak and does not vary much with temperature [7].

### g) Metamagnetism

Metamagnetism is a term used loosely in physics to describe a sudden increase in the magnetization of a material with a small change in an externally applied magnetic field. The metamagnetic behavior may have quite different physical causes for different types of metamagnets. Antiferromagnets with a large anisotropy may undergo a first-order transition to a phase in which there exists a net magnetic moment [8].

## 1.4. About this thesis

Transition metal vanadates are of great interest because they offer a variety of structural types (as shown in the results chapters) displaying 1, 2 and 3-dimensional magnetic properties. Vanadium (V) in particular can adopt a range of coordinations. Vanadium (V) acts as a diamagnetic spacer but the unpaired d-electron of vanadium (IV) can contribute to magnetic order or give rise to itinerant electron conductivity.

In the following chapters of the thesis the experimental methods will be first introduced after which the magnetic and other properties of various ternary transition metal vanadates will be reported.

## 1.5. References

1. C. N. R. Rao, Transition Metal Oxides, 2. Edition, John Wiley & Sons, (1998).
2. A. R. West, Basic Solid State Chemistry, John Wiley & Sons, (1984).
3. S. Blundell, Magnetism in Condensed Matter, Oxford University Press, (2001).
4. J. M. D. Coey, Magnetism and Magnetic Materials. Cambridge University Press, (2010).
5. M. Lenertz, J. Alaria, D. Stoeffler, S. Colis and A. Dinia, J. Phys. Chem. C **115**, 17190 (2011).
6. L. Balents, Nature **464** (7286) 199–208, (2010).
7. B. D. Cullity and C. D. Graham, Introduction to Magnetic Materials, 2. edition, John Wiley & Sons, (2009).
8. R. L. Carlin, Magnetochemistry, Springer-Verlag Berlin Heidelberg, (1986).

# Chapter 2. Experimental methods and instruments

## 2.1. High-pressure/high-temperature (HPHT) synthesis

HPHT synthesis allows unusual chemical substitution (bigger/smaller atoms) and favours high oxidation states and coordination numbers. In high pressures the outer-shell electronic orbits are distorted and atoms and molecules change in character. There is a general tendency toward more metallic behaviour as the electrons become less strongly fixed to particular atoms. High-pressure experiments take place between 0.1 and 500 GPa using a variety of experimental devices which can be separated into two broad classifications: “dynamic” techniques, creating high-pressure in the microsecond range and “static” techniques where the conditions are maintained for an arbitrary length of time. In both cases, the generated pressure can be classified as hydrostatic (directed anywhere), uniaxial (directed to a particular direction) or quasi-hydrostatic (both components). In dynamic pressure techniques, one or multiple shock waves are sent through the sample either by detonating an explosive or by allowing a hyper-velocity projectile to slam into a plate on which the sample is mounted. Despite the requirements of space, equipment and financial resources, this dynamic experimental technique is invaluable, since it is the only way to reach pressures significantly above 500 GPa in combination with very high temperatures and large sample volumes. In contrast, static high-pressure apparatuses enable reproducible conditions under nearly hydrostatic conditions in a wide pressure range depending on the sample volume [1].

### 2.1.1. Precursors

Precursors are commonly used in the HPHT synthesis. In this project they are prepared by grinding the reagents in a mortar and then pelletising the powder before heating it in the furnace. Since the solid state reaction involves complete disruption of the structure, high temperatures (above 400˚C) are required. Substantial thermal energy is required to overcome lattice energy and to increase the rate of diffusion.

Grinding ensures homogeneous mixing and decreases the particle size. By mechanical grinding it is possible to reduce the particle size up to 0.1 μm. Pelletising reduces the inter-particle void space thereby providing more interfaces for the reactions to take place [2].

### 2.1.2. Walker multianvil HPHT module

This is the press used in all the projects presented in this thesis. It provides high pressures and temperatures with large sample volume at a reasonable cost. With a Walker module it is possible to reach 26 GPa pressures but then the amount of sample gained is only 1 $mm^3$. With the assembly used at the School of Chemistry at the University of Edinburgh 5-8 $mm^3$ sample is attained at 11-16 GPa pressures. Temperatures up to 1500˚C are reached using graphite as a heater material, and these conditions can be maintained for several hours.

The sample is loaded into a boron nitride capsule and surrounded by graphite resistance heaters and MgO plugs to centre the sample. The zirconia sleeve is used as a thermal insulation. The heaters are contacted with molybdenum on both ends to allow the current to pass through. This set-up is then loaded into a sintered Cr-MgO octahedron. Eight truncated tungsten carbide cubes, which are kept apart from each other through pyrophyllite gaskets, are then arranged around the octahedron (Figure 2.1). The 14/8 assembly means that the octahedral edge length (OEL) is 14 mm and truncation edge length (TEL) 8 mm. Next the assembled set-up of 8 cubes is loaded into the containment ring with the steel wedges (Figure 2.2). The pressure distribution plate is placed on the top of the containment ring and the module is pushed into the press and positioned directly under the hydraulic ram. A current is directed to the cell via a small square of copper on either side of the cube.

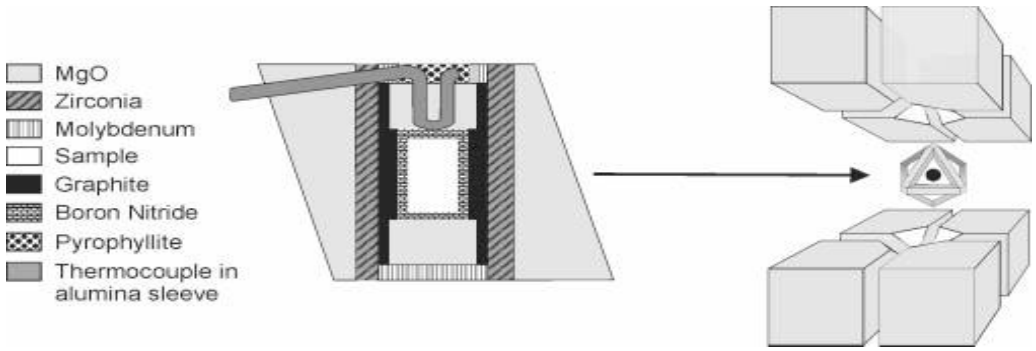


**Figure 2.1.** The cross section of the octahedral pressure cell

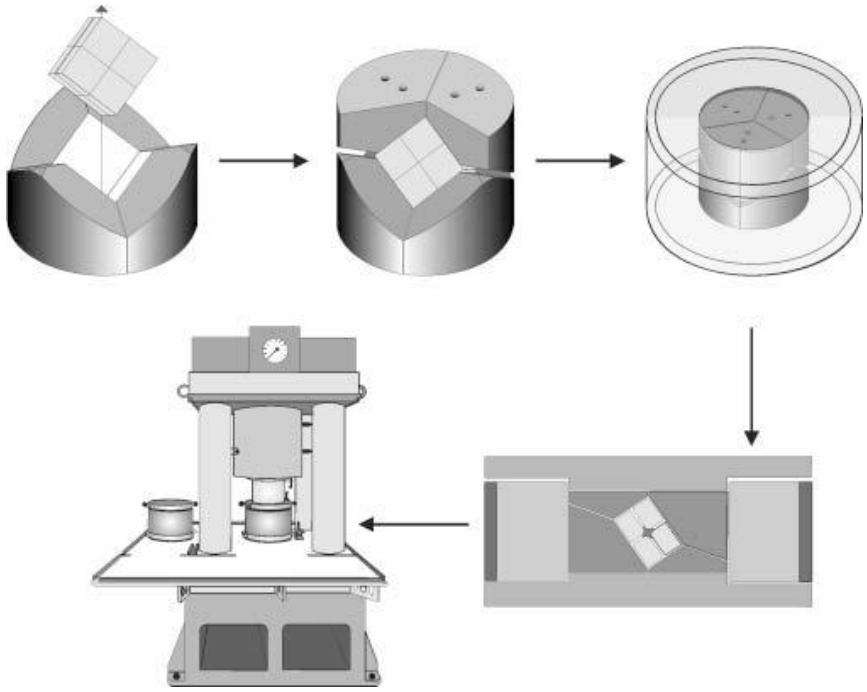

**Figure 2.2.** The assembly of the Walker module

## 2.2. Powder Diffraction Techniques

When all the atoms of the same type scatter a beam of radiation in the same way, the process is called coherent scattering. In neutron diffraction different isotopes may scatter differently or the scattering depends on the relative orientation of the magnetic moment of the neutron. Scattering is elastic when the wavelength and energy of the radiation remain unchanged during the scattering process [3].

The scattering of X-rays and neutrons obeys the same principles. The scattered waves interfere with each other constructively or destructively. In the powdered sample, which is also called as polycrystalline sample, all the crystalline domains are randomly oriented and, in the ideal case, equally represented. Solving the Bragg's equation, $n\lambda = 2d\sin\theta$ (Figure 2.3), gives the d-spacing between the crystal lattice planes of atoms that produce the constructive interference.

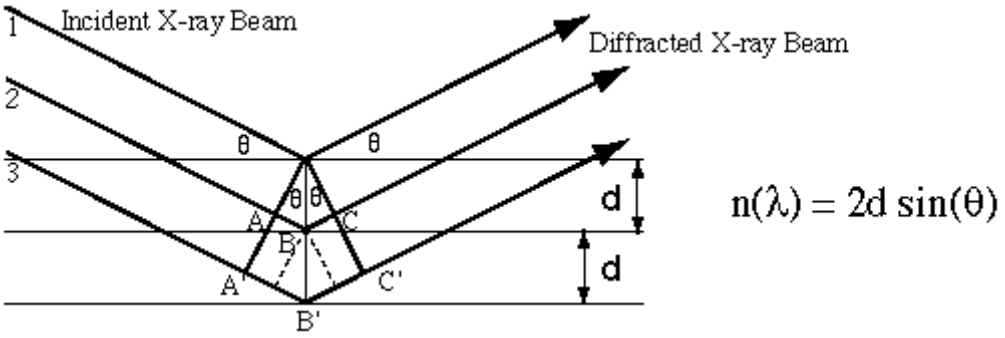


**Figure 2.3.** The Bragg's law.

Lattice planes are labelled by assigning three numbers known as Miller indices (hkl). The relation of d-spacing, lattice parameters and Miller indices is given by an equation which depends on the related structure of the compound. For example for the orthorhombic and cubic unit cells the following equations can be used [4]:

$$\frac{1}{d_{hkl}^2} = \frac{h^2}{a^2} + \frac{k^2}{b^2} + \frac{l^2}{c^2}$$ Equation 2.1.

for the orthorhombic unit cell and

$$\frac{1}{d_{hkl}^2} = \frac{h^2 + k^2 + l^2}{a^2}$$ Equation 2.2.

for the cubic unit cell.

### 2.2.1. X-ray Powder Diffraction

When X-ray photons collide with electrons, some photons from the incident beam will be deflected away from the direction in which they originally travel. If the wavelength of these scattered x-rays did not change, the process is called elastic scattering (Thomson Scattering). These are the X-rays that we measure in diffraction experiments as the scattered X-rays carry information about the electron distribution in materials. X-rays primarily interact with electrons in atoms. The atomic scattering factor of an atom is directly proportional to its atomic number. That is why X-ray diffraction does not give accurate information about the positions of the light atoms. Powder diffraction data can be collected using either transmission or reflection geometry, as shown in Figure 2.4. Because the particles in the powder sample are randomly oriented, these two methods will yield the same data except for the angle-dependent absorption in the transmission geometry.

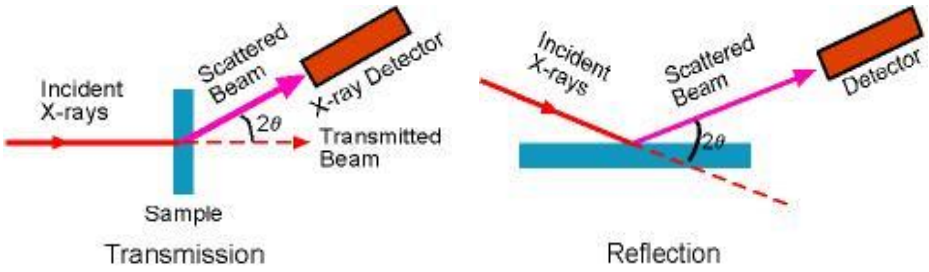


**Figure 2.4.** The data collection in X-ray powder diffraction

#### 2.2.1.1. Laboratory X-ray Powder Diffraction

Laboratory X-ray powder diffraction is a powerful and rapid technique for the identification of an unknown crystalline material. Its strengths include minimal sample preparation and straightforward data interpretation. Laboratory X-ray diffractometers consist of the three basic elements: X-ray tube, a sample holder and a X-ray detector. X-rays are generated in a cathode ray tube by heating a filament to produce electrons, accelerating the electrons toward a target by applying a voltage and bombarding the target material with electrons. When electrons have sufficient energy to dislodge inner shell electrons of the target material, characteristic X-ray spectra are produced. X-ray wavelengths are on the same scale as interatomic distances so they can be used to characterise the crystallographic structure and the crystallite size of the powdered solid samples.

#### 2.2.1.2. Synchrotron X-ray Powder Diffraction

The electromagnetic radiation emitted when charged particles are accelerated radially is called synchrotron radiation. It is produced in synchrotrons (cyclic particle accelerator) using bending magnets, undulators and/or wigglers. Almost all modern synchrotron radiation sources employ a dedicated storage ring. The basic principles of the operation of such sources are simple. Electrons are accelerated and injected into the storage ring; they are kept at a fixed energy within the orbit of the accelerator by application of a constant magnetic field. The synchrotron radiation is emitted tangentially from the beam orbit into a very small angle called the photon opening angle. The energy lost from the beam due to emission of the electromagnetic radiation is replenished by radio frequency power provided by a klystron. The synchrotron radiation provides the following major advantages in X-ray powder diffraction studies:

(i) The high intensity allows data to be collected rapidly allowing time dependent processes (e.g. phase transitions and solid state reactions) to be studied. In addition the intensity of the synchrotron beam allows small samples (of a few milligrams) to be studied.

(ii) The tunability of the source confers an advantageous flexibility in the choice of the optimum wavelength for an experiment and allows us to exploit the phenomenon of anomalous dispersion which is based on the variation of the real and imaginary parts of the X-ray scattering power at wavelengths close to the absorption edge.

(iii) The collimation of the beam results in very narrow Bragg peaks with well-defined peak shapes. With narrow, well-defined Bragg peaks, the field of high resolution powder diffraction (HRPD) is opened up. In traditional work with laboratory sources, the structural information, other than cell dimensions, available from X-ray powder diffraction is very limited [5].

### 2.2.2. Neutron Powder Diffraction

Neutron powder diffraction is a method by which neutrons are used to determine the atomic and/or magnetic structure of a material. It can be equally well applied to study crystalline solids, gases, liquids or amorphous materials.

Beam of neutrons can be produced by two mechanisms. The first one is to generate neutrons in a nuclear reactor in fission reactions. These reactions are catalysed by other neutrons, and slowed down by collisions with atoms in the moderator. Neutrons of constant wavelength are obtained from a reactor neutron source. The other source of neutrons is called a spallation source. In this case the neutrons are generated when a beam of high-energy protons fired into a heavy-metal target strike the nuclei and knock neutrons off. Like the neutrons created in fission reactions, these neutrons also need to be slowed down by passing through a moderating material. Usually in the spallation sources a pulsed beam of neutrons with a spectrum of wavelengths is produced though it is possible to generate a beam of constant wavelength neutrons [3]. Experiments using neutrons with various wavelengths is an example of a wavelength-dispersive diffraction where the detector $2\theta$ angle is fixed and wavelength is systematically changed.

Samples sizes required are large compared to those used in X-ray diffraction and the technique is therefore mostly performed as powder diffraction but there are also plenty of single crystal neutron diffraction studies. In the case of a neutron

scattering the fundamental scattering body in most atoms is the nucleus and not the electron, except for magnetic materials where the electronic scattering is also appreciable [6].

Within a factor of 2 or 3, most atoms scatter neutrons equally well, in contrast to the rapid increase with atomic number of the X-ray scattering amplitude (Figure 2.4). For example, the neutron scattering amplitude of a lead atom is only about 50 per cent greater than that of a carbon atom, in contrast with a ratio of approximately 20 : 1 for the X-ray scattering amplitudes of the two atoms. Not only does the neutron scattering amplitude show no regular or rapid increase with atomic number but it also shows no variation with the angle of incident radiation (Figure 2.5). This isotropic nature of the scattering is due to the fact that the dimensions of the nucleus, unlike those of the cloud of extranuclear electrons, are small in comparison with the wavelength of 1 Å. Consequently the ‘form factor' for neutron scattering is a straight line. Nor is there any angularly dependent polarization factor which occurs when using X-rays and which depends on the direction of the incident electromagnetic vibration. However, the magnetic materials may in magnetic fields show polarization effects depending on the direction of the neutron spin [6].

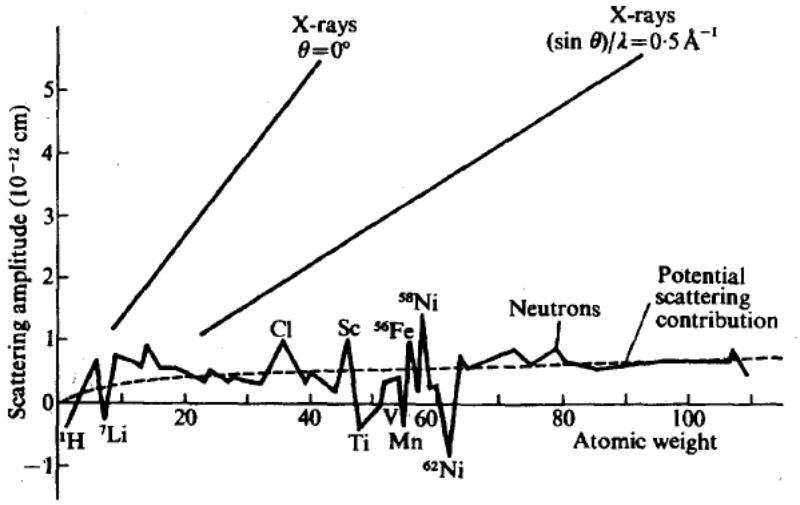


**Figure 2.4.** The comparison of the scattering amplitude of different atoms for neutrons and X-rays. Figure taken from ref. 6.

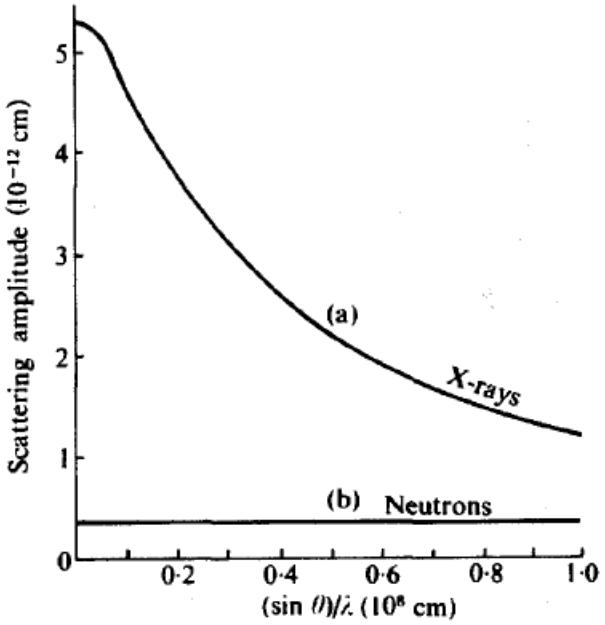


**Figure 2.5.** X-ray and neutron scattering amplitudes for a potassium atom as a function of a wavelength of the incident radiation. Figure taken from ref. 6.

Neutrons can be scattered by nuclear spins I and any unpaired electron spins. Magnetic scattering differs from the nuclear scattering as magnetic moment is a vector quantity. The scattering is dependent on the moment's direction and magnitude. There are a number of small interactions between neutrons and the electric charges in an atom, quite apart from the magnetic effect in which the neutron interacts with any atom which possesses a magnetic moment. However, these interactions are vastly smaller than the main interaction of the neutron with the nucleus [6].

A paramagnet gives an incoherent, diffuse diffraction pattern because it has random, fluctuating spins. Ordered magnetic structures give sharp, coherent peaks. Ferromagnets have all spins parallel, and the unit cell is same as the crystal structure cell. In the case of antiferromagnets the unit cell is sometimes doubled or increased by another factor in one or more directions [6].

By neutron powder diffraction it is possible to distinguish neighbouring (in the periodic table) elements over the different structural sites and locate the light atoms.

Neutrons penetrate into solid samples and thus are not sensitive to the surface reactions [7] or roughness and graininess like X-rays.

### 2.2.3. Instruments used

#### a) **Laboratory X-ray Powder Diffraction instruments**

For the initial check of the products a Bruker D2 Phaser desktop X-ray diffraction tool was used. It uses both Cu K $\alpha_1$ (1.5406 Å) and Cu K $\alpha_2$ (1.5443 Å) wavelengths. For long scans a Bruker AXS D8 powder diffractometer with Cu K $\alpha_1$ radiation and Ge (111) monochromator was used.

#### b) ID31 synchrotron X-ray powder diffraction instrument

ID31 is the beam line dedicated to high resolution powder diffraction at the ESRF in Grenoble. Its operational energy range is from 5 to 60 keV. The X-rays are produced by three 11-mm-gap ex-vacuum undulators, which cover the entire energy range from 5 keV to 60 keV (2.48 Å. to 0.21 Å in wavelength). The beam is monochromated by a cryogenically cooled double-crystal monochromator, with a choice of Si 111 crystals (Figure 2.6) for standard operation) or Si 311 crystals for higher energy resolution. The first monochromator crystal is side cooled by copper blocks through which liquid nitrogen flows. The second crystal is cooled by thermally conducting braids that link to the first crystal, and has electrical heaters to maintain its temperature stable to -60 ± 0.05ºC. Water-cooled slits define the size of the beam incident on the monochromator and of the monochromatic beam transmitted to the sample. In routine operation, a bank of nine detectors is scanned vertically to measure the diffracted intensity as a function of $2\theta$. Measurements of the flux at the sample yield, for example, 1.5 x $10^{12}$ photons $mm^{-2}$ $s^{-1}$ at 0.43 Å wavelength and 6.1 x $10^{12}$ photons $mm^{-2}$ $s^{-1}$ at 0.85 Å. This high intensity is excellent for a wide range of powder diffraction measurements [8].

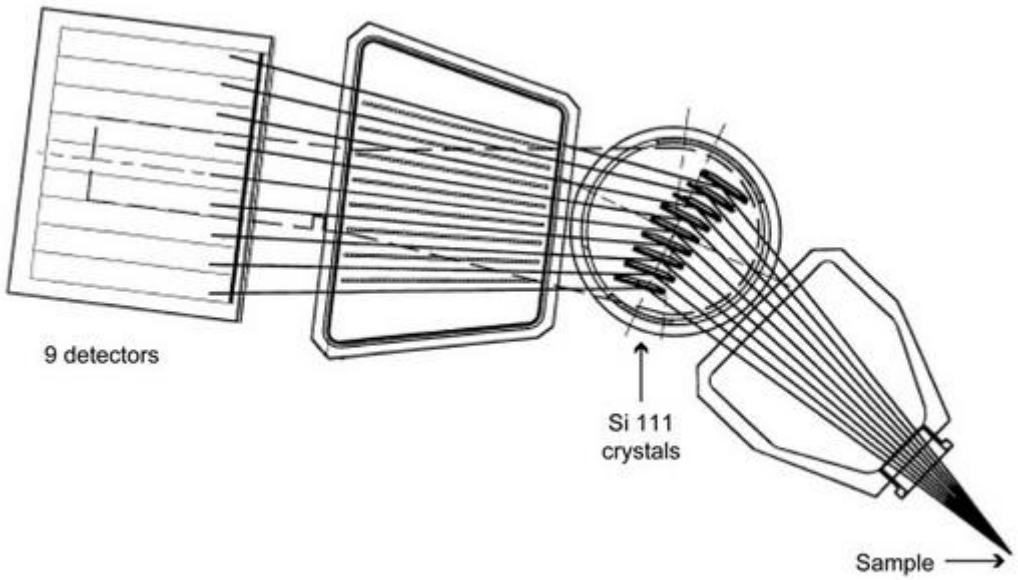


**Figure 2.6**. The path of radiation from the sample through double-crystal monochromator to the detector in ID31 instrument. Figure taken from ref. 8.

### c) D20 high flux neutron diffractometer

The neutron diffractometer D20 (Figure 2.7), based at the high-flux reactor of the Institut Laue-Langevin (ILL), is a medium to high resolution two-axis diffractometer capable of producing a neutron flux of $10^8$ $s^{-1}$ $cm^{-2}$ at the sample position. The 1536 detection cells of its curved linear position sensitive detector (PSD) cover a continuous $2\theta$ range of 153.6° over a total solid angle of 0.27 sr. This combination of a high incident neutron flux and a large detector solid angle provides D20 with the fastest counting rate, at a given resolution, of any reactor-based neutron diffractometer. The D20 instrument has several dedicated or D20-specific sample environments: a large vacuum vessel to reduce air-scattering for room-temperature experiments, an Orange cryostat (1.7 K to 300 K) with a choice of $\varphi$25 mm and $\varphi$50 mm vanadium tails, a top-loading furnace with either vanadium ($T$ < 1150 °C) or niobium ($T$ < 1500 °C) heating elements, and an Eulerian cradle 4-circle sample goniometer (room temperature). In addition, various sample environments from the ILL 'pool' can be used at D20, including standard gas and clamp pressure cells, a

new 100 kbar Paris-Edinburgh cell, a cryofurnace (1.7 K to 500 K) and cryomagnets (typically 6 T) [9].

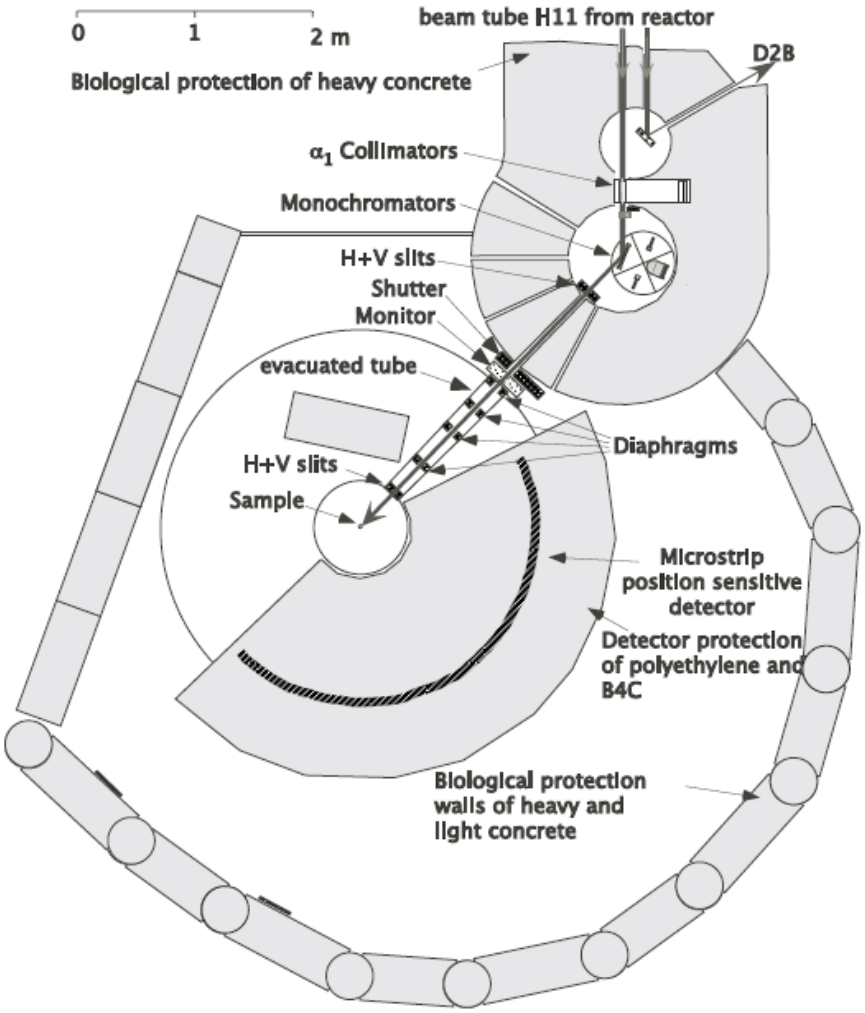


**Figure 2.7.** Schematic top-view of the D20 neutron diffractometer. Figure taken from ref. 10.

### d) D2B high-resolution neutron diffractometer

D2B at ILL in Grenoble is a very high-resolution powder diffractometer designed to achieve the ultimate resolution, limited only by powder particle size ($\Delta d/d$ $5x10^{-4}$), but is was built so that an alternative high flux option, with resolution comparable to that of D1A, but much higher intensity, could be chosen at the touch of a button. The diffractometer D2B is characterised by the very high take-off angle (135°) for the monochromator (Figure 2.8). A complete diffraction pattern is obtained after about 25 steps of 0.05° in $2\theta$, since the 128 detectors are spaced at 1.25° intervals. Such scans take typically 30 minutes; they are repeated to improve statistics. Apart from the work on superconductors, D2B is particularly well suited for the Rietveld refinement of relatively large structures, such as zeolites with absorbed molecules. It has, as well, proved successful for the solution of some of the new 'quasi-crystalline' materials. With the new 2D-detector, the efficiency of D2B has increased by an order of magnitude, and it is now possible to measure very small samples of about 200 mg with high resolution. D2B was also designed for work on magnetism and high resolution of very large d-spacings using wavelengths of between 2.4 Å and 6 Å. A large graphite filter can be switched in to provide a very clean beam at 2.4 Å, and a cold Be-filter can be used for longer wavelengths [11].

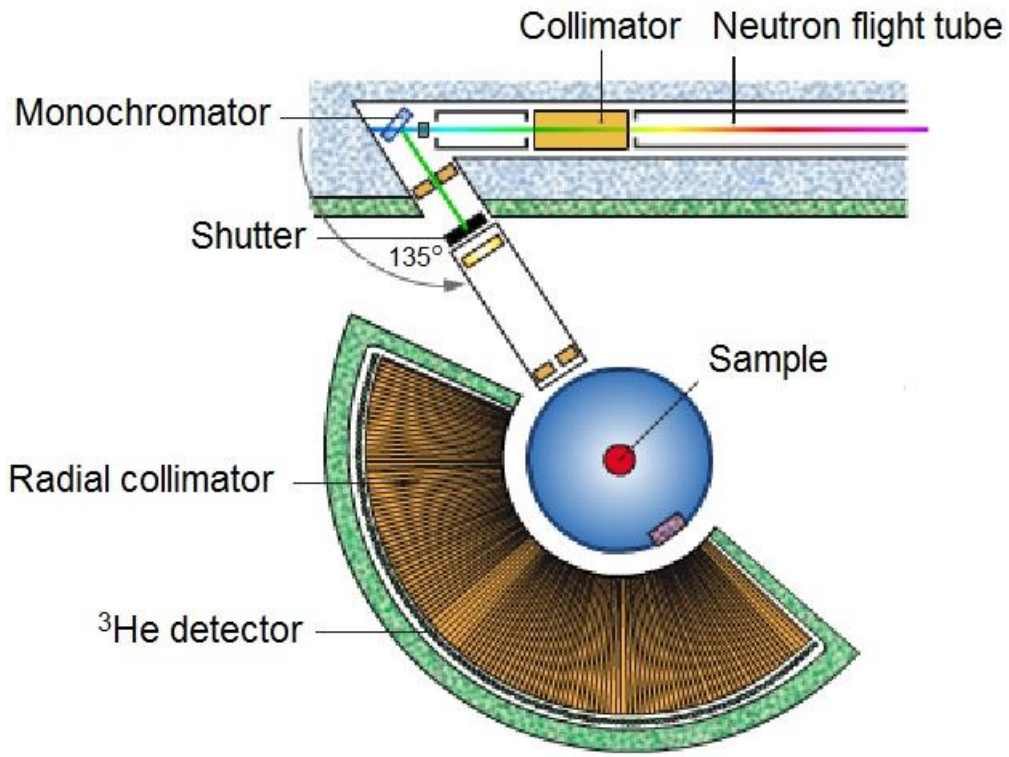


**Figure 2.8.** Schematic view of the D2B neutron diffractometer. Figure taken from ref. 11.

### e) GEM high intensity, high resolution neutron diffractometer

GEM at ISIS pulsed neutron source can be used to perform high intensity, high resolution experiments to study the structure of disordered materials and crystalline powders. The GEM detectors cover a scattering angle range from 1.1° to 169.3°. The GEM vacuum vessel is made of 25 mm grade 304 stainless steel, and is designed to attain pressures as low as $1x10^{-6}$ mbar. The GEM beam-stop weighs about 80 tonnes, with a canister of boron carbide at the centre to absorb neutrons [12].

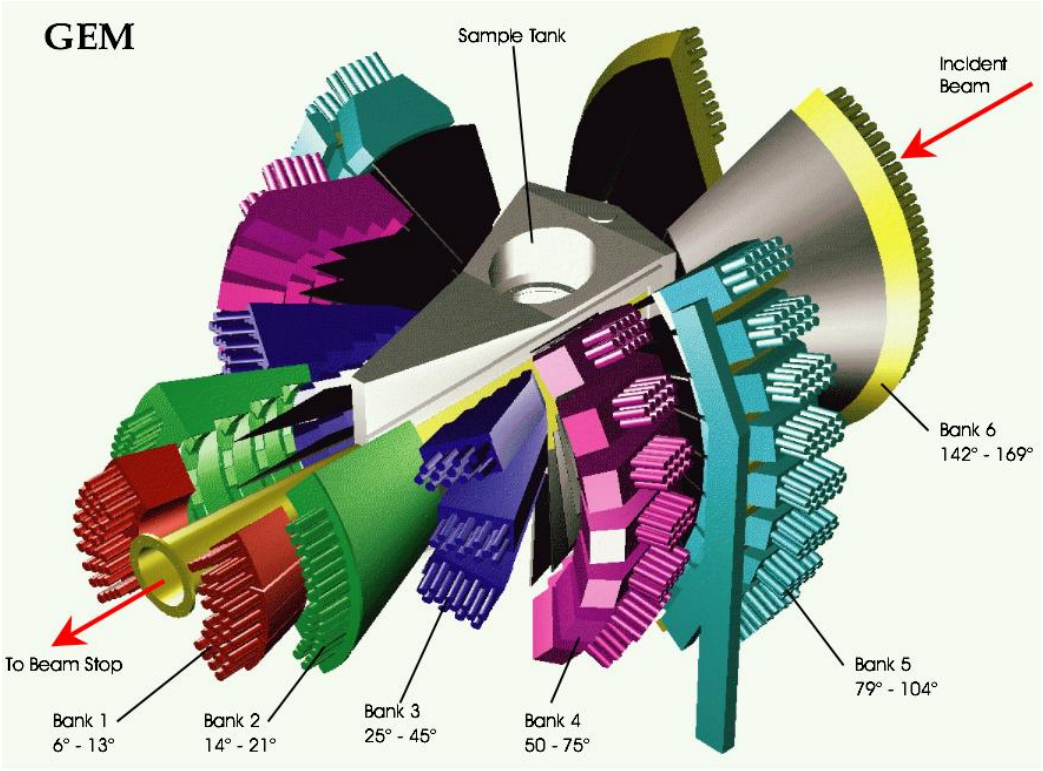


**Figure 2.9.** Detector banks and the sample tank of GEM neutron diffractometer. Figure taken from ref. 12.

### f) WISH long-wavelength neutron diffractometer

WISH (Figure 2.10) at the ISIS pulsed neutron source is a long-wavelength diffractometer primarily designed for powder diffraction at long d-spacing in magnetic and large unit cell systems, with the option of enabling single-crystal and polarised beam experiments. High-resolution cold-neutron powder diffraction excels when multiple nearly overlapping Bragg peaks occur at long d-spacing. In this case, sheer flux is not sufficient to extract all the available information, and much better results can be obtained with a high-resolution diffractometer such as WISH, even at the cost of losing some flux. WISH provides high resolution data over a d-spacing range of 0.7-17 Å with a single frame bandwidth of 8 Å. WISH uses $^{3}$He detectors covering scattering angles from 10 to 170 degrees [13].

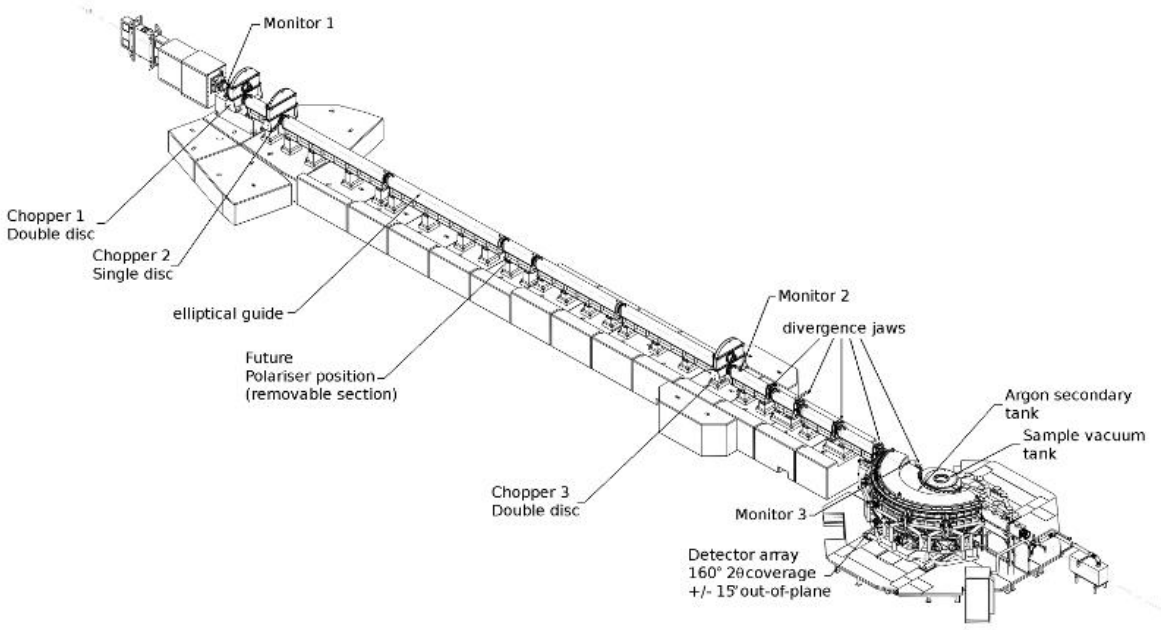


**Figure 2.10.** WISH neutron diffractometer beamlime. Figure taken from ref. 13.

### 2.2.4. Rietveld refinement

In response to the need to develop enhanced procedures for obtaining structural information from powder samples Rietveld proposed in the late 1960s a method for analysing the more complex patterns obtained from low-symmetry materials by means of a curve-fitting procedure. The least-squares refinement minimizes the difference between the observed and calculated profiles, rather than individual reflections. In the first instance, this procedure was carried out with constant wavelength neutrons, rather than X-rays because of the simpler peak shape of the Bragg reflections. With constant wavelength neutrons it can normally be assumed that the reflections are Gaussian in shape, and the calculated intensity at each point on the profile is obtained by summing the contributions from the Gaussian peaks that overlap at that point. In addition to the conventional parameters in the least-squares procedure (i.e. scale factor, atomic coordinates and temperature factors), additional parameters are required: the lattice parameters (which determine the positions of the reflections), a zero-point error for the detector, and three parameters that describe the variation of the Gaussian half-width (full width at half maximum intensity) with scattering angle. The technique has been applied to a wide

range of solid-state problems and has been reviewed by several authors [7,14] during the last 25 years. The application of the Rietveld method to neutron data in the early 1970s was soon followed by its extension to laboratory X-ray diffractometer data. The problem of the more complex peak shape was resolved by employing alternative peak-shape functions, such as the Lorentzian and the pseudo-Voigt. Other problems that can plague X-ray studies include preferred orientation and poor powder averaging (graininess), both of which arise from the fact that X-rays probe a smaller sample volume than do neutrons. These problems were addressed by paying a closer attention to the data collection strategy. The Rietveld method is a powerful tool, but it is limited by the same drawback that affects powder methods in general: the loss of information that arises from the compression of the three-dimensional diffraction pattern into a single dimension. It is also important to underline the fact that the Rietveld method, though an excellent technique for refining structures, requires a good starting model if it is to converge successfully and does not, by itself, constitute a method for structure determination**.** The role of powder diffraction in the structural characterization of materials has expanded dramatically during the last 30 and the advent of the Rietveld refinement method has played an important role in that [15].

The quality of the refinement's fit is measured by R values. The weighted-profile R value, $R_{wp}$, is defined as

$$R_{wp} = \left\{ \sum_i w_i [y_i(\text{obs}) - y_i(\text{calc})]^2 / \sum_i w_i [y_i(\text{obs})]^2 \right\}^{1/2}$$

Equation 2.3.

Ideally, the final $R_{wp}$ should approach the statistically expected R value, $R_{exp}$

$$R_{\text{exp}} = \left[ (N - P) / \sum_i^N w_i y_i(\text{obs})^2 \right]^{1/2}$$

Equation 2.4.

$R_{exp}$ reflects the quality of the data (i.e. the counting statistics). Thus, the ratio between the two

$$\chi^2 = (R_{wp}/R_{exp})^2 \qquad \text{Equation 2.5.}$$

which is also quoted quite often in the literature, should approach 1. If the data have been 'over-collected' (i.e. errors are no longer dominated by counting statistics), $R_{exp}$ will be very small and $\chi^2$ for a fully refined structure much larger than 1. Conversely, if the data have been 'under-collected' (i.e. collected too quickly), $R_{exp}$ will be large and $\chi^2$ could be less than 1 [7].

## 2.3. Magnetic Measurements

The Magnetic Property Measurement System (MPMS) used in the magnetic measurements utilises Superconducting Quantum Interference Device (SQUID) technology. The modular MPMS design integrates a SQUID detection system, a precision temperature control unit residing in the bore of a high-field superconducting magnet, and a sophisticated computer operating system. The cryostat enables measurements over the temperature range of 1.9 – 400 K [16].

A direct current SQUID (Figure 2.11), which is used at CSEC, is the most sensitive device for detecting the magnetic flux. It consists of two Josephson junctions connected in parallel. When the SQUID is biased with a current greater than the critical current, the voltage across the SQUID is modulated with the flux treading the SQUID. Therefore, the SQUID is a flux-to-voltage transducer. This special flux-to-voltage characteristic enables the detection of small magnetic field, current, voltage, inductance and magnetic susceptibility etc [17]. A Josephson junction is made up of two superconductors, separated by an insulating layer so thin that electrons can pass through. A SQUID consists of tiny loops of superconductors employing Josephson junctions to achieve superposition: each electron moves simultaneously in both directions. DC SQUIDs demonstrate resistance in response to

even tiny variations in a magnetic field, which is the capacity that enables detection of such minute changes.

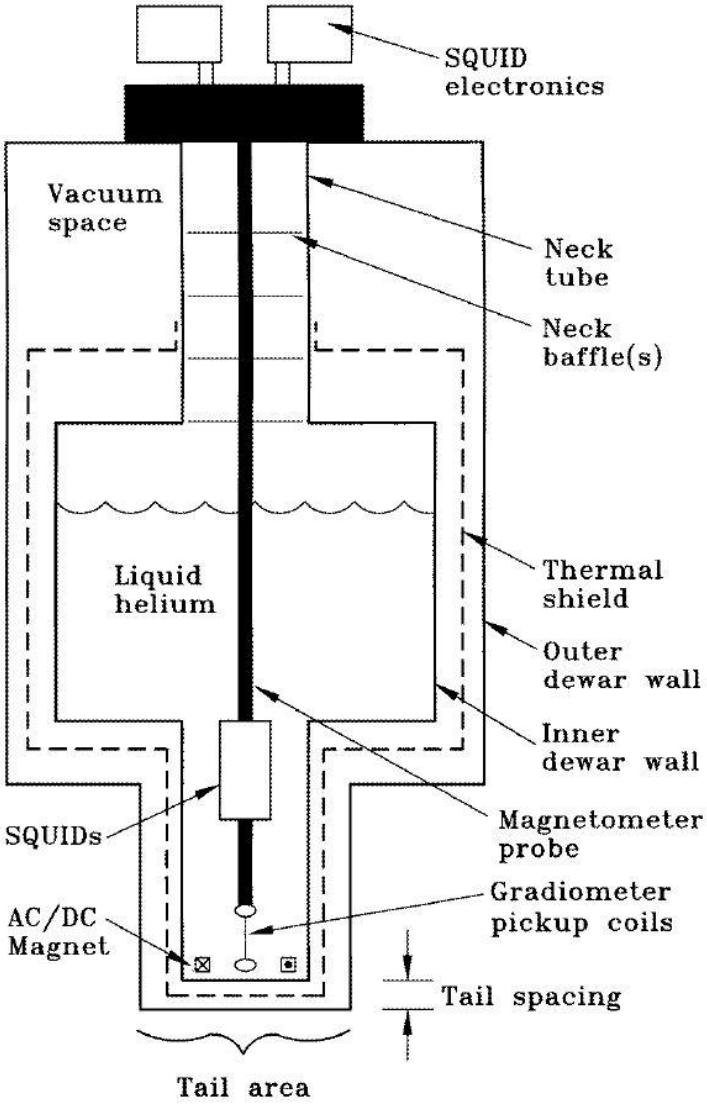


**Figure 2.11**. A cross sectional schematic of a simple low-$T_c$ SQUID gradiometer system. The SQUID and input coil, housed in a superconducting niobium cylinder, are inductively coupled to an axial gradiometer near the tail of the Dewar. The Dewar is filled with liquid helium (boiling point 4.2 K) to cool the superconducting SQUID, niobium shield and pick-up coils. The Dewar is insulated by a vacuum space between the inner and outer walls. Figure taken from ref. 18.

## 2.4. Resistivity measurements

### 2.4.1. Ambient pressure resistivity measurements

Ambient pressure resistivity measurements were carried out in a PPMS (Physical Property Measurement System). PPMS is a variable temperature-field system, designed to perform a variety of automated measurements. Sample environment controls include fields up to ± 16 Tesla and temperature range of 1.9 - 400 K. PPMS has four independent channels for performing DC resistivity.

A four-point wiring set-up on polycrystalline sample pellets was used (figure 2.12) for the temperature range 2 – 300 K. The outer two wires are used to apply a current, while the inner two wires are used to measure the voltage drop across the sample. This set-up allows for the cancellation of the internal resistances of the wires as well as the contact resistances between the wires and the sample, and provides accurate measurement of the resistance of the sample under study.

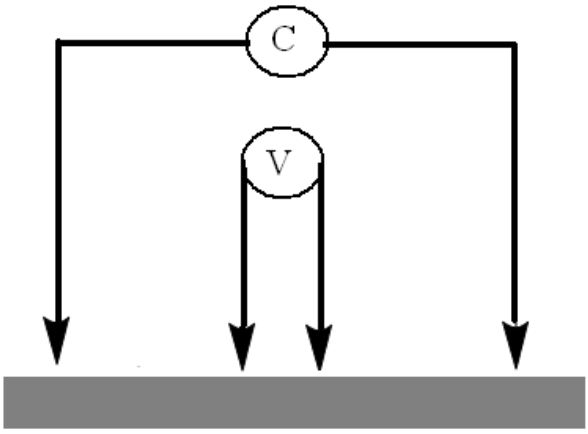


**Figure 2.12.** The 4-point wiring set-up of the current (I) and voltage (V) wires on the sample.

### 2.4.2. Pressure-cell measurements

High pressure resistivity measurements were carried out using a diamond anvil cell. The cell consists of the following main components (Figures 2.13 and 2.14): a) upper locknut, b) cell body, c) the wires enter/leave the cell through special slits, d) lower locknut, e) diamond anvils, f) metallic gasket, g) upper anvil holder, h) – j) various pressure spacers. All metallic parts of the pressure cell are made of hardened Be-Cu material, which provides mechanical stability, but also is non-magnetic and facilitates studies in a magnetic field.

The basic operation of the pressure cell involves the application of a force load to the anvils. The force is applied and locked by the rotation of the upper locknut and is transmitted through the various spacers and the upper anvil holder to the high pressure sample space. The high-pressure sample space is located between the two diamond anvils and the sample hole in the metallic gasket. The gasket is indented prior to the experiment to ensure that the deformation of the gasket helps maintain the high pressure within the central hole in the gasket. The thickening of the gasket immediately outside the high-pressure region provides lateral support to the anvils, a function that contributes to the pressure generation in the sample space.

For electrical experiments the gasket is covered with an additional insulating layer, to avoid the shorting of the electrodes to the gasket. The insulation consists of a mixture of Stycast resin 1266 mixed with alumina $Al_2O_3$ powder in the ratio 2 : 3 by weight for greater hardness. In these experiments the pressure transmitting medium was the insulation of the gasket. The various pressure spacers consist of disks made of a variety of different materials, ranging from hardened Be-Cu to soft Teflon, and function to minimise thermal contraction and expansion of the pressure cell parts to avoid large changes in the pressure as the temperature changes.

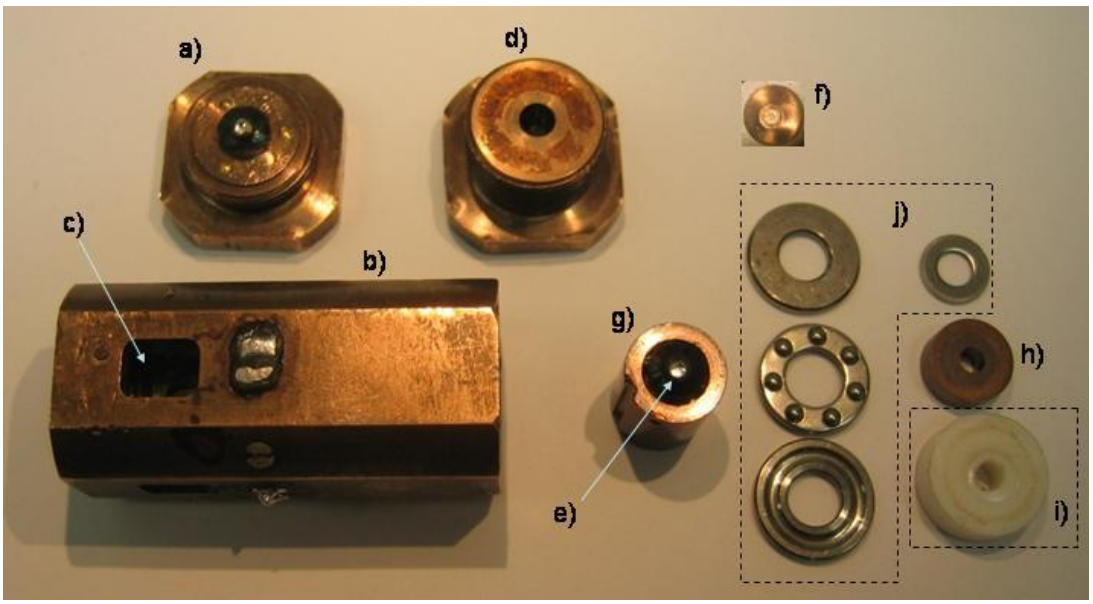


**Figure 2.13.** Main components of the diamond anvil cell.

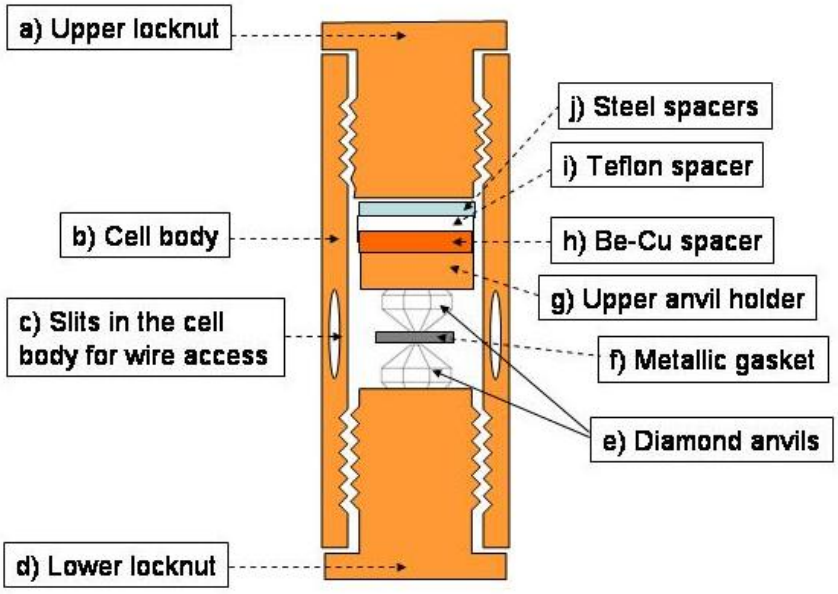


**Figure 2.14.** Schematic cross-section of the DAC pressure cell.

The set-up of the experiment consists of the following steps:

1. The diamond anvils are cleaned with cotton buds soaked in ethanol and the gasket is cleaned in an acetone solution inside an ultrasonic bath.
2. The gasket is positioned on top of the lower diamond anvil and held in place by a ring of Apiezon grease, forming a ring around the sloping side of the anvil. The side of the gasket is marked with either a marker or a small scratch to assure replacing of the gasket in the same place each time it is removed.
3. The cell is closed and a force is applied in small increments to avoid breaking the anvils. The gasket is indented to an approximate thickness of ~ 100 μm, whereas the unindented thickness of the gasket is ~ 300 μm.
4. After the indentation, the gasket is removed from the anvil and a hole is drilled in the centre of the indentation. The hole depends on the culet size of the anvils. For a culet size of 800 μm, the hole size is between 300 – 400 μm.
5. For electrical measurements, the gasket is then insulated with a mixture of two-part Stycast resin 1266, mixed with alumina powder $Al_2O_3$. The powder grains in the alumina powder have to be approximately 1-3 μm in diameter for optimal results.
6. Once the insulation is cured the completed gasket is again secured on top of the lower diamond anvil. This time it is glued with Araldite resin to the lower locknut in order to allow more stability.
7. Four gold wire leads were glued using GE-varnish on the top of the insulation of the gasket, and positioned in the appropriate manner on the sample, where the current leads are touching the sides of the sample and the voltage leads are touching the upper surface with approximately 100 – 150 μm separation (Figures 2.15 and 2.16). Gold wire is used because of its good conductivity but also because it is soft and flows well.
8. When the force is applied to the pressure cell, and the pressure locked inside the cell by rotation of the upper locknut the gold leads will be pressed against the sample creating an electrical connection. This is an advantage of using the solid pressure medium, as was done in this case. The disadvantages are the larger pressure gradients that ensue in the high-pressure sample space.

**Figure 2.15.** Be-Cu gasket: the gasket was indented to ~ 100 μm thickness, and the sample space hole was ~ 300 μm diameter, for diamond anvils with culets of 800 μm.

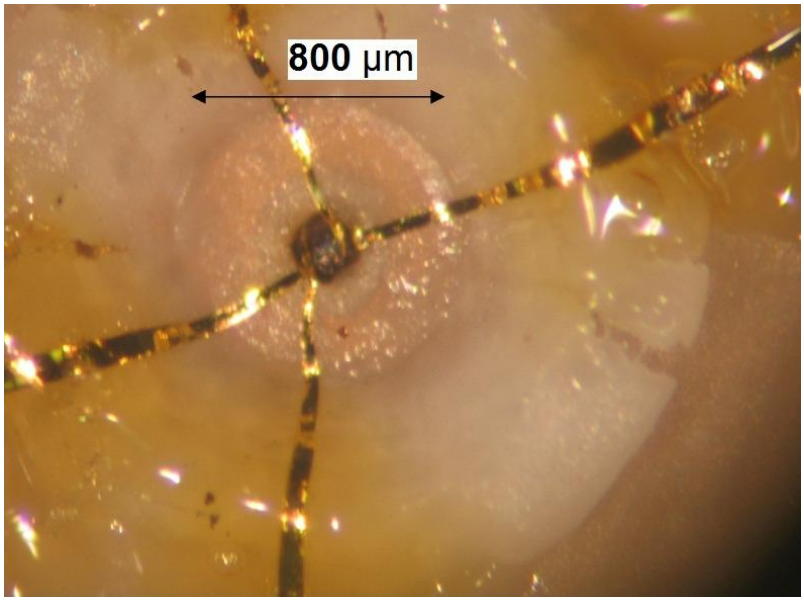


**Figure 2.16.** Sample prepared for pressure measurements. The Be-Cu gasket is insulated with a Stycast 1266 and $Al_2O_3$ mixture. Gold leads are touching the sample on the side for the current leads and on the top of the sample for the voltage leads. The application of a load between the anvils will pressurise the gold leads to the surface of the sample, forming an electrical contact.

Sections 2.4.1 and 2.4.2 were written together with Dr. Anna Kusmartseva.

## 2.5. References


1. H. Huppertz, Zeitschrift Fur Kristallographie, **219**, 330-338, (2004).
2. A. R. West, Basic Solid State Chemistry, John Wiley & Sons, (1984).
3. M. T. Dove, Structure and Dynamics, Oxford University Press, (2003).
4. Integrating Research and Education website http://serc.carleton.edu/research_education/geochemsheets/techniques/XRD.html
5. Applications of synchrotron radiation, Edited by C.R.A. Catlow and G.N. Greaves, Chapman and Hall, (1990).
6. G. E. Bacon, Neutron Diffraction, 3. Edition, Clarendon Press, Oxford, (1975).
7. L. B. McCusker, R. B. Von Dreele, D. E. Cox, D. Louer and P. Scardi, *J. Appl. Cryst.*, **32**, 36-50, (1999).
8. http://www.esrf.eu/UsersAndScience/Experiments/StructMaterials/ID31
9. T. C. Hansen, P. F Henry, H. E Fischer, J. Torregrossa and P. Convert, Meas. Sci. Technol. **19,** 3, 034001, (2008).
10. P. Convert, T. Hansen and J. Torregrossa, Mater. Sci. Forum, **321–324,** 314–9, (2000).
11. http://www.ill.eu/?id=13299
12. http://wwwisis2.isis.rl.ac.uk/disordered/gem/gem_home.htm
13. http://www.isis.stfc.ac.uk/instruments/wish/science/wish-science6445.html
14. J. E. Post and D. L. Bish, Reviews Mineral. and Geochem., **20**, 277-308, 1989.
15. A. K. Cheetham, Chapter 2, Structure Determination from Powder Diffraction Data, edited by W. I. F. David *et al*. (2002).
16. http://www.qdusa.com/products/mpms.html
17. H. Yang, J. Chen, S. Wang, C. Chen, J. Jeng, J. Chen, C. Wu, S. Liao and H. Horng, Tamkang, J. Science and Engineering, **6**, 1, 9-18, (2003).
18. W. G. Jenks, S. S. H. Sadeghi and J. P. Wikswo, J. Phys. D: Appl. Phys. **30,** 293–323, (1997).

# Chapter 3. Synthesis, properties and incommensurate spin order of the metallic perovskite $MnVO_3$

## 3.1. Introduction

Ideal perovskites (Figure 3.1) have the general formula $ABX_3$. They have a primitive cubic structure with space group $Pm\bar{3}m$ in which the bond lengths are related to the unit cell dimensions by the following equation

$$a = \sqrt{2}r_{A\text{-}X} = 2r_{B\text{-}X} \qquad \text{Equation 3.1.}$$

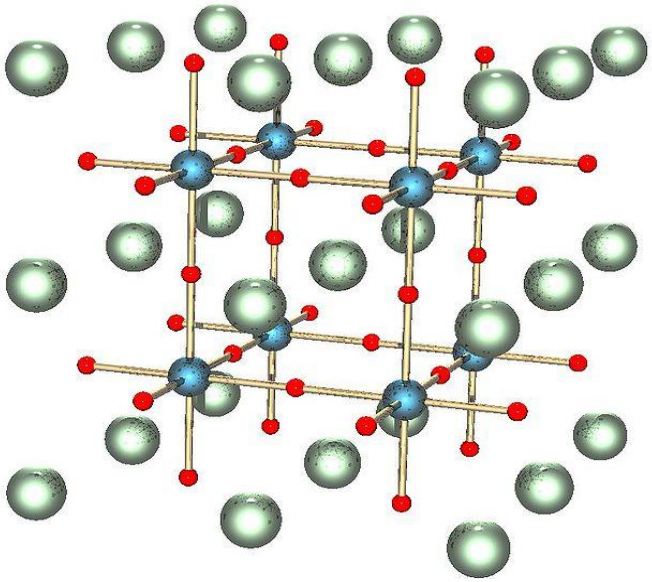

**Figure 3.1.** The ideal perovskite $ABX_3$ structure. The red spheres are *X*-atoms (usually oxygens), the blue spheres *B*-atoms (smaller metal cation) and the green spheres the *A*-atoms (larger metal cation).

The *A* atom is in 12-fold coordination (cuboctahedral) and the *B* atom in 6-fold (octahedral) coordination. In the ideal perovskite the large *A* cation is surrounded by eight $BX_6$ octahedra. Perovskite crystals are constructed of $BX_6$-octahedra which

share all of their corners with the neighbouring octahedra. In the ideal $ABX_3$ structure the anions and *A* cations form a cubic close-packed array. Within this structure the smaller cations occupy one quarter of the octahedral interstices in sites not adjacent to the *A* cations [1].

The degree to which the sizes of a distorted perovskite departs from the ideal structure is given by a tolerance factor *t*

$$t = \sqrt{2}r_{A\text{-}X}/2r_{B\text{-}X} \qquad \text{Equation 3.2.}$$

Cubic perovskite forms with *t* in the range $0.9 < t < 1.0$. For ideal cubic structures *t* is unity. For the greater values hexagonal closed-packed structures are usually favoured over the cubic structures [1].

The stability of the perovskite structure depends on the relative sizes of the *A* and *B* elements as well as on the electronic configuration of the *B* sites ions. The perovskite structure is found for *t* values ranging from 0.8 to about 1.1. For the *t* value greater than 1, the space available for the *B* ion in its "$X_6$" octahedron is so large that it can rattle. Small r values ($t < 0.8$) correspond to *A* and *B* ions of similar size, leading to more close-packed structures such as ilmenite [2]. The distortion of an ideal perovskite can lead to lower symmetry orthorhombic, tetragonal, rhombohedral, monoclinic or triclinic structures.

A combination of X-ray and neutron diffraction data is useful in determining the crystal structure of perovskite type compounds. Long-range order and lattice constants are generally best determined by X-ray single crystal or powder diffraction methods, whereas anion positions, bond lengths and displacement (or thermal) parameters are best obtained by powder neutron diffraction [1].

In the cubic perovskites all *B-X-B* bonds are 180° which leads to strong connections and unusual physical properties like colossal magnetoresistivity, superconductivity and ferroelectrics.

The perovskite structure is ideally suited for the study of 180° cation-anion-cation interaction of octahedral site cations. The possibility of cation-cation interaction is remote because of the large interaction distance along the face diagonal. The variety in the properties of perovskites is illustrated by the following

examples: $BaTiO_3$ is ferroelectric, $SrRuO_3$ is ferromagnetic, $LaFeO_3$ is weakly ferromagnetic, and $BaPb_{1-x}Bi_xO_3$ is superconducting, $LaCoO_3$ shows a nonmetal-to-metal transition and $La_{1-x}Sr_xMnO_3$ exhibits colossal magnetoresistivity. There are several metallic perovskite oxides, for example $ReO_3$, $A_xWO_3$, $AMoO_3$ (A = Ca, Sr, Ba), $SrVO_3$ and $LaNiO_3$. Metallic conductivity in perovskites arises entirely due to the strong cation-anion-cation interaction [2].

The majority of the synthetic $ABX_3$ perovskite group compounds are distorted derivatives of the ideal cubic structure. There are three main distortion mechanisms: two cation displacement mechanisms (first and second order Jahn-Teller effects) and the tilting of the octahedra which usually has a far greater effect on lattice parameters [3].

1. First-order Jahn-Teller distortion of $BX_6$ octahedra when *B*-cation has odd number of *d*-electrons in the $e_g$-orbitals. This results in the degeneracy of the $e_g$-orbitals of *B*-site cations and the distortion of the octahedron along a tetrad axis with the formation of two long bonds or short bonds on opposite sides of the octahedron. $LaMnO_3$ is one example of perovskites with this type of distortion [1].

2. Second-order Jahn-Teller effects on the *A* and *B* cation polyhedra reflecting mixing of the molecular orbitals and/or lone pair effects. Interactions between a non-degenerate ground state and a low-lying excited state result in the displacements of *A*- and *B*-cations from the centre of the coordination polyhedra. Displacement of *B*-cations from the centre is the cause of the ferroelectric properties of some perovskites, e.g. $BaTiO_3$ [1].

3. Rotation or tilting of distortion-free $BX_6$ octahedra arising from the too small size of the *A* cation for the 12-fold site within the $BX_6$ framework (e.g. $LaFeO_3$) [1]. To accommodate the too small *A* cations the octahedra tilt about pseudocubic axes in order to achieve the lowest energy mode for the crystal. Tilting results in 1) changes in *A*-*X* bond lengths so that they are no longer equal, 2) changes in the *A*-site coordination and 3) the concomitant reduction in symmetry.

Perovskites of orbitally degenerate transition metal cations synthesized under high pressure and temperature are often far from equilibrium when recovered to ambient conditions, and this thermodynamic instability may be expressed through unusual electronic phenomena. For example, $SrCrO_3$ undergoes an orbitally driven

electronic phase separation at low temperatures [4,5,6] and $PbRuO_3$ shows an unusual symmetry reversing transition associated with orbital order [7,8] that is not observed in other $A$RuO$_3$ ruthenates. $A$VO$_3$ perovskites of $3d^1$ $V^{4+}$ have been synthesized at ambient pressure for $A$ = Ca and Sr and at high pressures (4 – 7 GPa) for $A$ = Cd, Pb, and Mn. High pressure conditions are needed to stabilize the smaller cations at the perovskite A site. The ambient pressure perovskites $CaVO_3$ and $SrVO_3$ are metallic [9,10] and $CaVO_3$ shows a well-defined Fermi surface arising from itinerant $3d^1$ $V^{4+}$ states [11]. $CdVO_3$ is also metallic and Pauli paramagnetic [12]; however, $PbVO_3$ is an antiferromagnetic, ferroelectric insulator with coupled, off-centre distortions of the $Pb_{2+}$ and $V^{4+}$ ions [13,14]. Thin films of $PbVO_3$ have been grown at ambient pressures, and piezoelectric and nonlinear optical activity were reported [15,16]. $MnVO_3$ perovskite was reported in 1970 by Syono *et al.* [17] but was not subsequently characterized. It was reported to be a Curie-Weiss paramagnet with a relatively low electric resistivity [17]. The physical properties of this phase are of interest, because $Mn^{2+}$ is smaller than the other A cations, which is expected to reduce the width of the V *d*-band and increase electron–electron correlation, and the $S$ = 5/2 $3d^5$ $Mn^{2+}$ moments may couple to the $3d^1$ $V^{4+}$ states, leading to complex magnetic order.

The resistivity measurements under pressure were done in collaboration with Dr. Anna Kusmartseva. The propagation vector to index the magnetic peaks in section 3.3.4.b) was found in collaboration with Dr. Clemens Ritter from ILL and the other results mentioned in the same section were obtained in collaboration with Dr. Angel Arevalo-Lopez. Figures 3.10 and 3.11 were also done in collaboration with Dr. Angel Arevalo-Lopez. The band structure calculations were done in collaboration with Dr. Hua Wu from Fudan University, Shanghai.

## 3.2. Experimental

Syono *et al.* [17] had earlier synthesised $MnVO_3$ by mixing MnO and $VO_2$ and heating at 900 - 1200°C and at 4.5 – 8 GPa. This method was tried but it did not produce desired results this time.

It had been discovered in earlier experiments by the Attfield group that $Mn_2V_2O_7$ is reduced to $MnVO_3$ under the HPHT conditions. The precursor $Mn_2V_2O_7$ was synthesised by heating ground and pelletised MnO and $V_2O_5$ for 12 hours at 750°C. The precursor was then pressed in the Walker module (see section 2.1.2) at 7 GPa or 8 GPa and 1100°C. Heating was applied for 15 min, 30 min or 1 hour with quenching and 30 min with slow cooling. The fit (Figure 3.2) to the data from

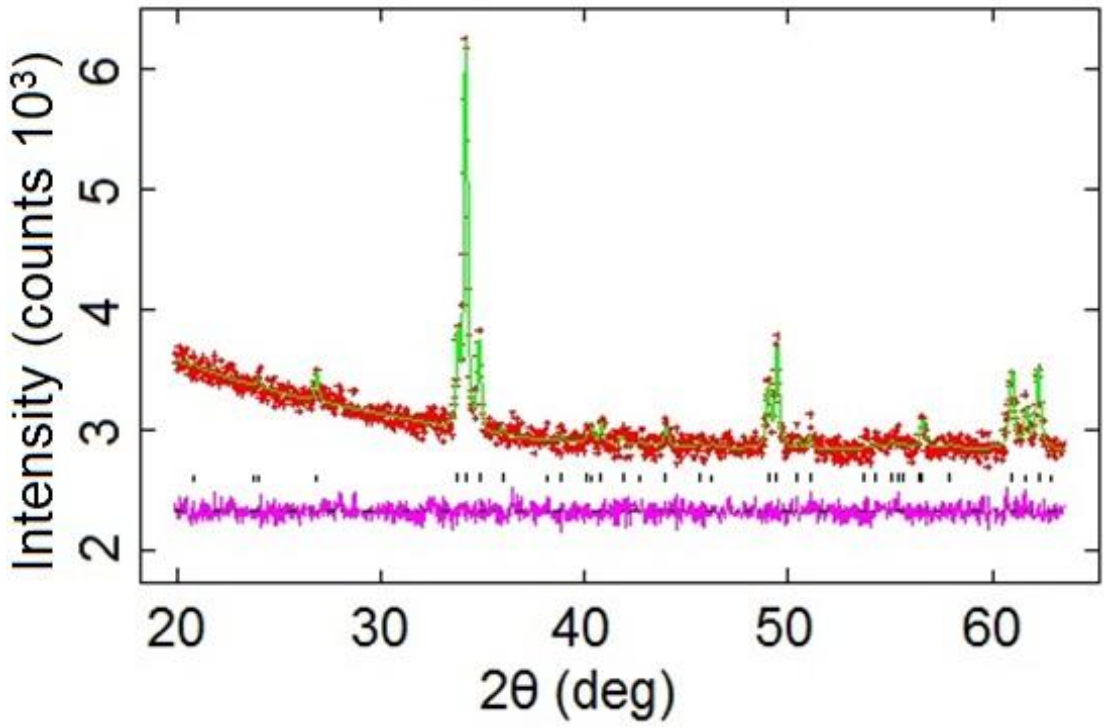


**Figure 3.2.** Laboratory powder X-ray diffraction profile for $MnVO_3$ perovskite.

laboratory powder x-ray diffraction measurements (see section 2.2.3) was made in an earlier reported [17] space group *Pnma* and showed the optimum conditions to be 1100°C under 8 GPa of pressure for 30 min, followed by a quench to ambient temperature and depressurization. Six high-pressure products were combined to give

a 77 mg $MnVO_3$ sample for synchrotron x-ray and neutron powder diffraction measurements.

The resistivity measurement at ambient were performed on a PPMS (Physical Property Measurement System) using a four-point probe set-up (see section 2.4.1) and the measurements under pressure using a diamond anvil cell (see section 2.4.2) Magnetisation measurements were carried out using a DC-SQUID (see section 2.3) in a 0.1 T field.

The synchrotron x-ray powder diffraction studies were carried out at ESRF on ID31 (see section 2.2.3) high resolution powder diffraction beamline using 0.399 Å wavelength. The data were collected at 4 K, 10 K, 20 – 60 K in 10 K steps and 80 – 300 K in 20 K steps. The refinement was done using GSAS software package [18].

Neutron diffraction data were collected on two different instruments. A high-resolution neutron diffraction profile collected at room temperature from instrument D2B (see section 2.2.3) at the Institut Laue-Langevin (ILL) at a wavelength of 1.594 Å was used to refine the crystal structure of $MnVO_3$. The refinement was done using the GSAS software package. Further neutron data were collected between 1.7 and 60 K in 1-K steps from the ILL's high flux instrument D20 (see section 2.2.3) at a wavelength of 2.418 Å to explore the spin order in $MnVO_3$.

## 3.3. Results

### 3.3.1. Resistivity measurements

The measurements at ambient pressure did not give consistent and reliable results. The results mostly showed $MnVO_3$ to be slightly semiconducting.

However measurements under pressure gave consistent results showing metallic conductivity with a residual resistivity of $\rho_0 \approx 300\ \mu\Omega cm$ (Figure 3.3). The temperature dependence of the resistivity is described well by a conventional Fermi liquid $\rho = \rho_0 + CT^2$ variation at low temperatures, and enhanced phonon or electronic correlations are not apparent. This behaviour does not change significantly up to 67 kbar of pressure, and no electronic transitions are evident down to 2 K in this pressure range, showing that the metallic state is robust and no proximity to a metal-

insulator phase boundary is manifest. A small positive magnetoresistance up to 5 % is observed at low temperatures (2 - 10 K) in applied fields of 9 T. The magnitude increases on cooling and at 100 K magnetoresistance has almost disappeared. This is characteristic of the normal (Lorentz force) magnetoresistance of a metal, and the absence of resistance and magnetoresistance (Figure 3.4) discontinuities at the 46 K magnetic transition shows that the conductivity is not strongly coupled to the spin order, in contrast to metallic *B*-site manganites, e.g., $La_{1-x}Ca_xMnO_3$, which show colossal magnetoresistance.

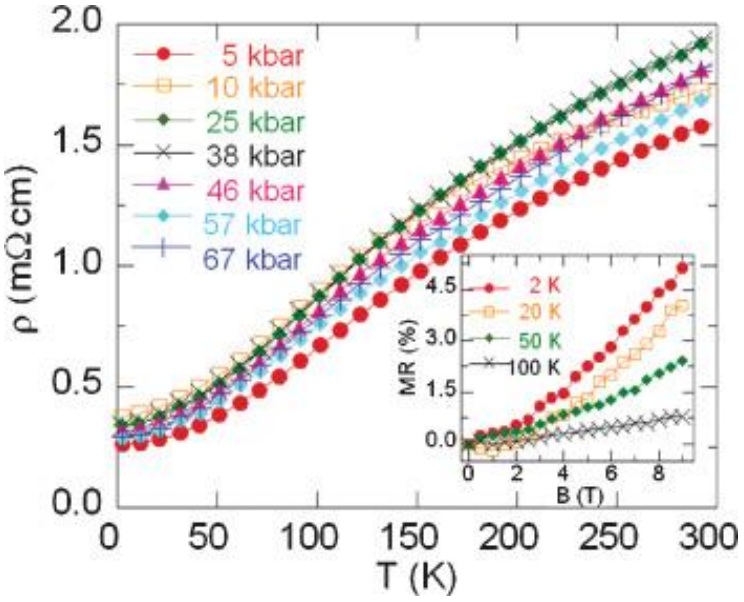


**Figure 3.3.** Resistivity of a ~150-$\mu$m $MnVO_3$ pellet fragment at pressures of 5 – 67 kbar. The inset shows the field dependence of magnetoresistance at 2 – 100 K under 5 kbar of pressure.

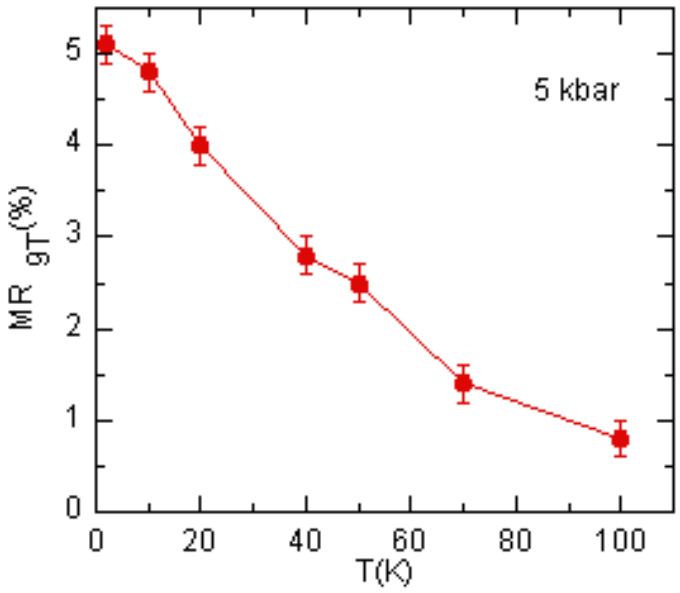


**Figure 3.4.** Resistivity of a ~150-$\mu$m $MnVO_3$ pellet fragment at 5 kbar pressures in 9 T field as a function of temperature.

### 3.3.2. Magnetisation measurements

The measurement in 0.1 T reveal an ordering transition at $T_N$ = 46 K (figure 3.5) and Curie-Weiss paramagnetism at higher temperatures. The linear fit to inverse susceptibility data between 120 and 200 K, $\chi^{-1} = 36.7 + 0.24T$, gives a paramagnetic moment of 5.80 $\mu_B$, which is close to the theoretical value of 5.91 $\mu_B$ for localized $S$ = 5/2 $Mn^{2+}$, and a Weiss temperature of $\theta = -154$ K, showing that antiferromagnetic spin–spin interactions are dominant and partly frustrated ($|\theta|/T_N \approx 3$). Syono *et al.* [17] reported the transition temperature of 65 K and $\mu_{eff}$ of 7.0 $\mu_B$ for the same compound. Hysteresis measured at 5 K is presented in the Figure 3.6. Measurement shows a small ferromagnetic, symmetric hysteresis loop.

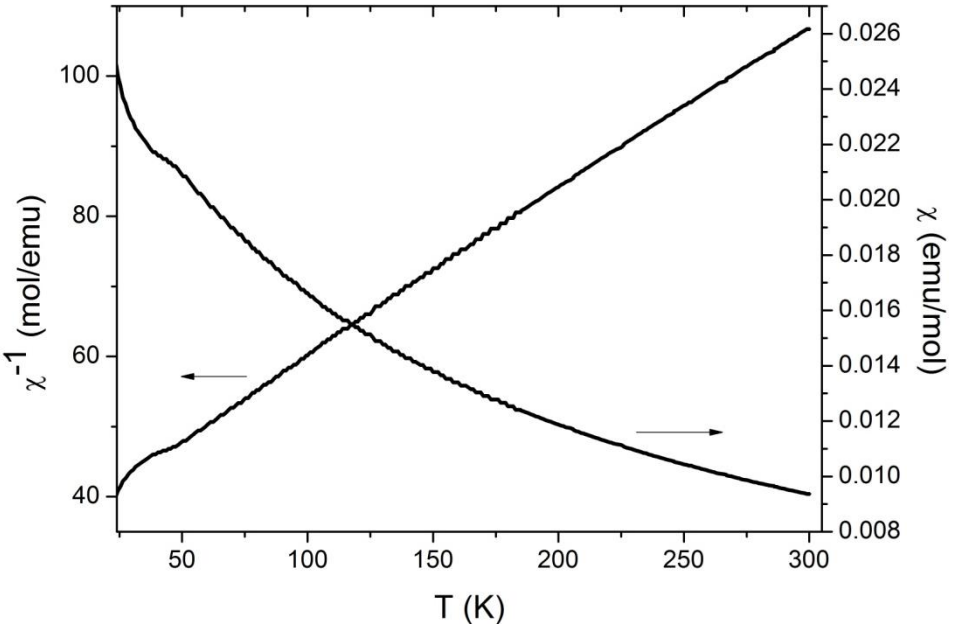


**Figure 3.5.** Plots of magnetic susceptibility and inverse magnetic susceptibility against temperature in 0.1 T for the $MnVO_3$ perovskite

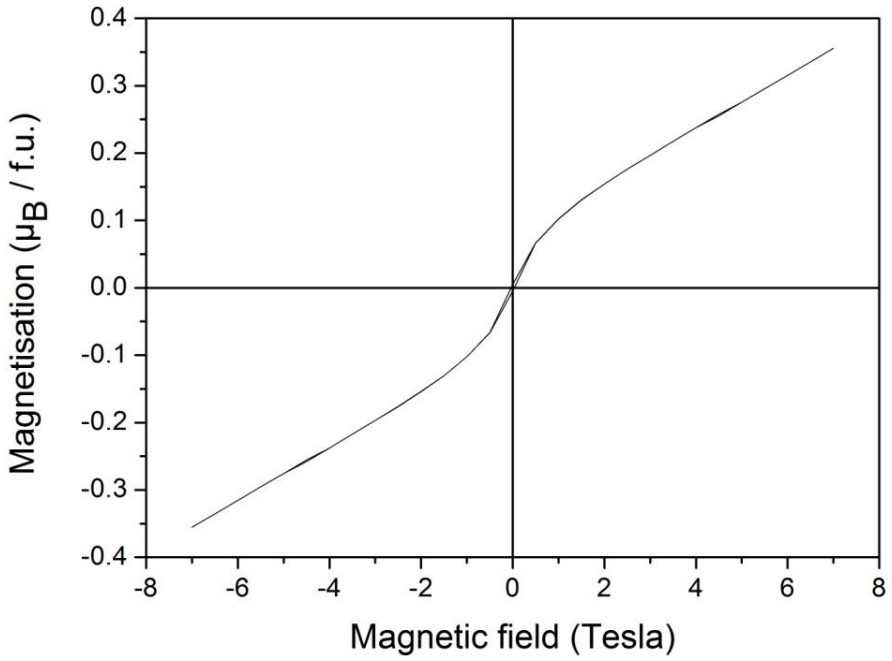


**Figure 3.6**. Hysteresis measured at 5 K for the $MnVO_3$ perovskite showing a small ferromagnetic, symmetric hysteresis loop.

### 3.3.3. Synchrotron X-ray Powder Diffraction

The results confirmed that $MnVO_3$ adopts an orthorhombic *Pnma* perovskite superstructure. The data showed that the combined sample from the several syntheses contained two $MnVO_3$ phases or components (i.e. unexpected peak splitting) (Figures 3.7 and 3.8 and Table 3.1). The phase with the slightly smaller lattice parameters was dominant with 67 % proportion. The existence of two phases could be due to some of the high-pressure products being non-stoichiometric. No Mn/V disorder was found in the Rietveld refinement but $VO_2$ impurity of ~ 11%, which was refined in a space group F222, was present. The likely structure of the material would then be $MnV_{1-x}Mn_xO_3$. No further lattice distortions, structural transitions or anomalies were observed between 4 and 300 K. The refined structural parameters were in agreement with those from neutron analysis which is described later.

**Table 3.1.** Lattice parameters for the two phases of $MnVO_3$ at 4 and 300 K.

| | | a | b | c | volume |
|---|---|---|---|---|---|
| 4 K | phase 1 | 5.1037(1) | 5.2634(1) | 7.3783(1) | 198.20(1) |
| | phase 2 | 5.1182(2) | 5.2677(3) | 7.4164(3) | 199.95(2) |
| 300 K | phase 1 | 5.1183(1) | 5.2714(2) | 7.4021(2) | 199.71(2) |
| | phase 2 | 5.1259(2) | 5.2777(3) | 7.4194(3) | 200.72(2) |

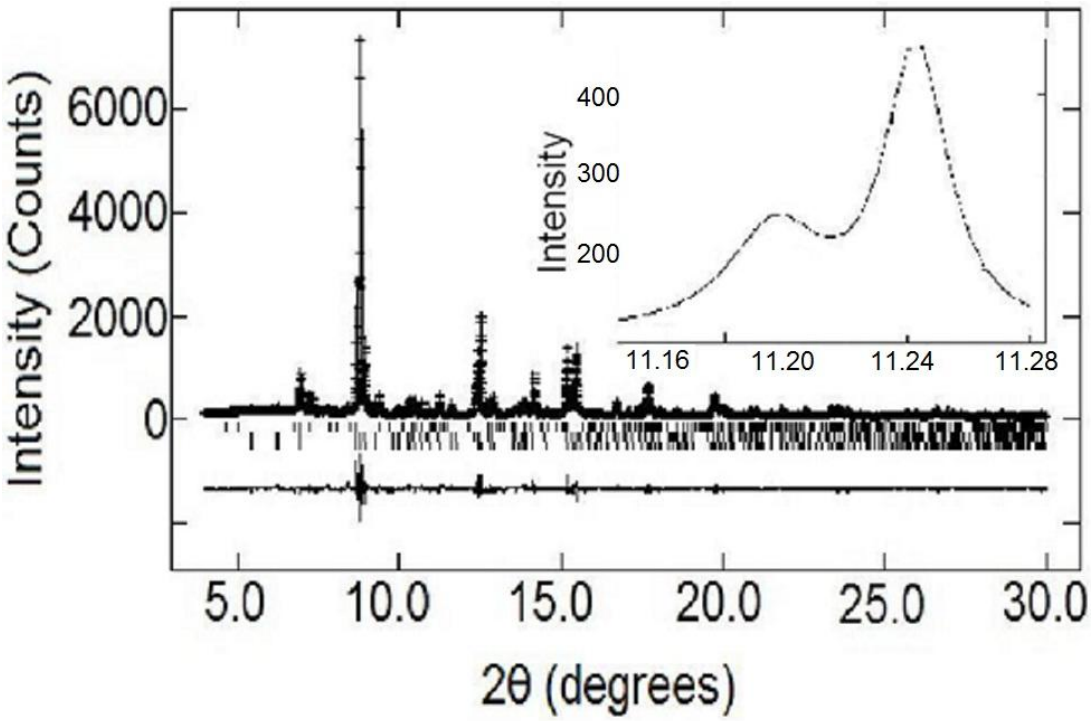


**Figure 3.7.** X-ray diffraction profile at 4 K for the $MnVO_3$ perovskite with an expansion showing the existence of two $MnVO_3$ phases.

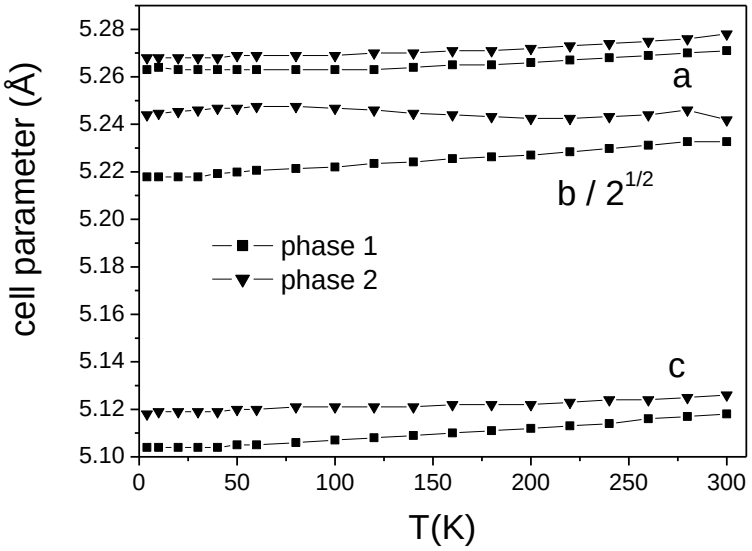


**Figure 3.8.** The variation in the lattice parameters in temperature range 4 – 300 K for the two phases of $MnVO_3$ perovskite.

### 3.3.4. Neutron powder diffraction

#### a) Room temperature measurements at instrument D2B

Results of the refinement (Figure 3.9) including lattice and thermal parameters and atomic positions are presented in Tables 3.2 and 3.3. The structure adopts a highly distorted *Pnma* arrangement in which the 12 *A*-*O* distances, which are equivalent in a cubic perovskite, are split into sets of four short (2.2 Å), four medium (2.4–2.6 Å), and four long (3.1–3.4 Å) Mn-O bonds (Table 3.4). The $VO_6$ octahedra are tetragonally compressed with two short (1.88 Å) and four long (1.95–1.98 Å) V-O distances, in contrast to $CaVO_3$ and $SrVO_3$, where the octahedra are nearly regular. This would be consistent with an orbital ordering of localized $3d^1$ $V^{4+}$ states if $MnVO_3$ were insulating, but because this material is metallic it more likely reflects the intrinsic distortions caused by the mismatch between the Mn-O and the V-O distances. The $ABO_3$ perovskite tolerance factor $t = D(A - O)/\sqrt{2}D(B - O)$ has an ideal value of $t = 1$ for a cubic structure, but orthorhombic $MnVO_3$ has $t = 0.89$.

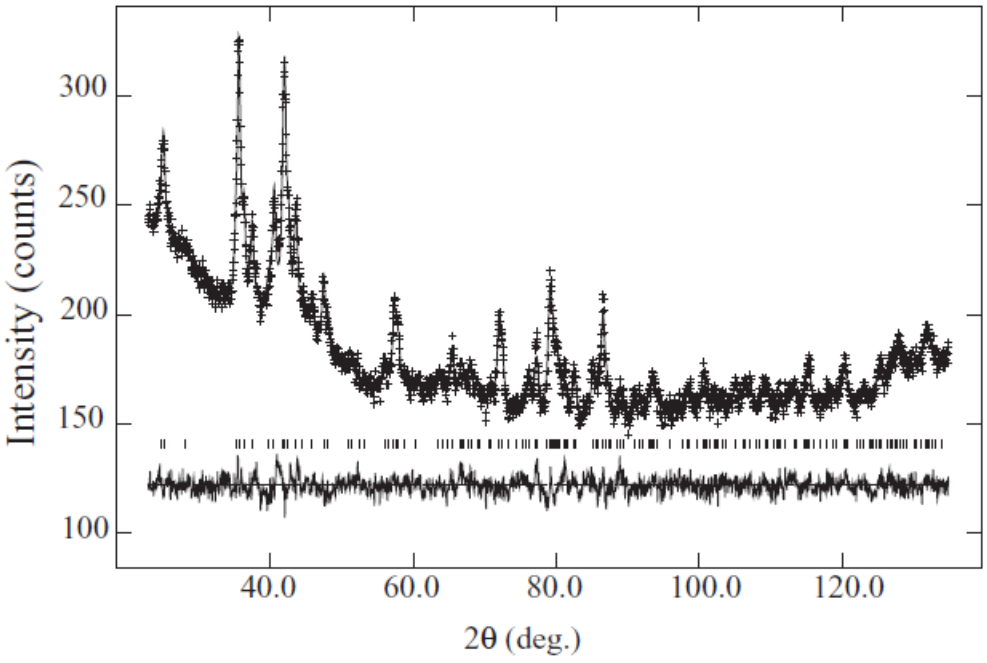


**Figure 3.9.** Fit to the neutron diffraction profile of $MnVO_3$ perovskite collected at 300 K on instrument D2B.

**Table 3.2.** Refined lattice parameters, atomic coordinates and thermal displacement parameters from refinement of the $MnVO_3$ perovskite at 300 K at instrument D2B. Fitting residuals, $R_{wp}$, and $\chi^2$, were 0.021 and 1.652 respectively.

| a (Å) | b (Å) | c (Å) | Volume (Å$^3$) | |
|---|---|---|---|---|
| 5.2741(6) | 7.410(1) | 5.1184(8) | 200.03(6) | |
| Atom | x | y | z | $U_{iso}$(Å$^2$) |
| Mn | 0.0630(21) | 0.25 | 0.4853(22) | 0.0169(25) |
| V | 0 | 0 | 0 | 0.0169(25) |
| O1 | 0.4551(12) | 0.25 | 0.6074(12) | 0.0085(16) |
| O2 | 0.2983(9) | 0.0582(6) | 0.1842(8) | 0.0100(10) |

**Table 3.3.** Selected interatomic distances and angles for the perovskite $MnVO_3$ at 300 K.

| Bond | Length (Å) | Angle | Degrees |
|---|---|---|---|
| Mn1 − O1 | 3.266(11) | V1 - O1 - V1 | 144.19(34) |
| Mn1 − O1 | 2.161(11) | V1 - O2 - V1 | 143.74(25) |
| Mn1 − O1 | 3.086(11) | O1 - V - O1 | 180 |
| Mn1 − O1 | 2.161(11) | O1 - V - O2 (×2) | 91.43(24) |
| Mn1 − O2 (×2) | 2.436(9) | O1 - V - O2 (×2) | 87.59(26) |
| Mn1 − O2 (×2) | 2.173(9) | O1 - V - O2 (×2) | 92.41(26) |
| Mn1 − O2 (×2) | 2.605(6) | O1 - V - O2 (×2) | 88.57(24) |
| Mn1 − O2 (×2) | 3.422(10) | O2 - V - O2 (×2) | 180 |
| V1 − O1 (×2) | 1.9468(19) | O2 - V - O2 (×2) | 90.56(8) |
| V1 − O2 (×2) | 1.884(4) | O2 - V - O2 (×2) | 89.44(80 |
| V1 − O2 (×2) | 1.982(40 | Mn1 - O1 - Mn1 | 152.2 (6) |

**b) Low temperature measurements at instrument D20**

Magnetic diffraction peaks appear below 46 K (Figure 3.10.(a)) and are all indexed by propagation vector $k$ = ($k_x$ 0 0). The magnitude of the orthorhombic structural distortion is sufficient to enable alternative vectors, e.g., (0 $k_y$ 0) or (0 0 $k_z$), to be excluded because they do not match the peak positions. $k_x$ varies slightly with temperature, from $k_x$ = 0.2903(4) at 1.7 K to $k_x$ = 0.3015(9) at 43 K. The

incommensurate magnetic structure was refined using representation analysis within the FULLPROF software package [19] The ($k_x$ 0 0) order of *A*-site spins within a *Pnma* perovskite has previously been analyzed for $TbMnO_3$ [20,21,22] and below we use the corepresentation analysis from ref. 21 (Table 3.5), where the application of an antiunitary operator for inversion of the propagation vector gives a fuller symmetry description than conventional irreducible representations.

**Table 3.5.** Magnetic (axial vector) corep modes for the perovskite *A* site (*RE* in the case of *RE*$MnO_3$) associated with the four type of irreducible corepresentations for space group *Pnma* and propagation vector $k_7$= ($\mu$,0,0). By construction, these modes are invariant by application of the antiunitary operator *KI*, where *I* is the inversion at the origin of the coordinate system and *K* is the complex conjugation. $\epsilon = e^{+i\pi\mu}$ and $\epsilon^*$ is its complex conjugate. Table taken from ref. 21.

| | | $RE(1)=x,\frac{1}{4},z$ | $RE(2)=x+\frac{1}{2},\frac{1}{4},-z+\frac{1}{2}$ | $RE(3)=-x+\frac{1}{2},\frac{3}{4},z-\frac{1}{2}$ | $RE(4)=-x+1,-\frac{1}{4},-z+1$ |
|---|---|---|---|---|---|
| $D_1$ | $m_y$ | 1 | $\epsilon^*$ | 1 | $\epsilon^*$ |
| | $m'_y$ | 1 | $\epsilon^*$ | $-i$ | $-i\epsilon^*$ |
| $D_2$ | $m_x$ | 1 | $-\epsilon^*$ | $-1$ | $\epsilon^*$ |
| | $m'_x$ | 1 | $-\epsilon^*$ | $i$ | $-i\epsilon^*$ |
| | $m_z$ | 1 | $\epsilon^*$ | 1 | $\epsilon^*$ |
| | $m'_z$ | 1 | $\epsilon^*$ | $-i$ | $-i\epsilon^*$ |
| $D_3$ | $m_x$ | 1 | $\epsilon^*$ | 1 | $\epsilon^*$ |
| | $m'_x$ | 1 | $\epsilon^*$ | $-i$ | $-i\epsilon^*$ |
| | $m_z$ | 1 | $-\epsilon^*$ | $-1$ | $\epsilon^*$ |
| | $m'_z$ | 1 | $-\epsilon^*$ | $i$ | $-i\epsilon^*$ |
| $D_4$ | $m_y$ | 1 | $-\epsilon^*$ | $-1$ | $\epsilon^*$ |
| | $m'_y$ | 1 | $-\epsilon^*$ | $i$ | $-i\epsilon^*$ |

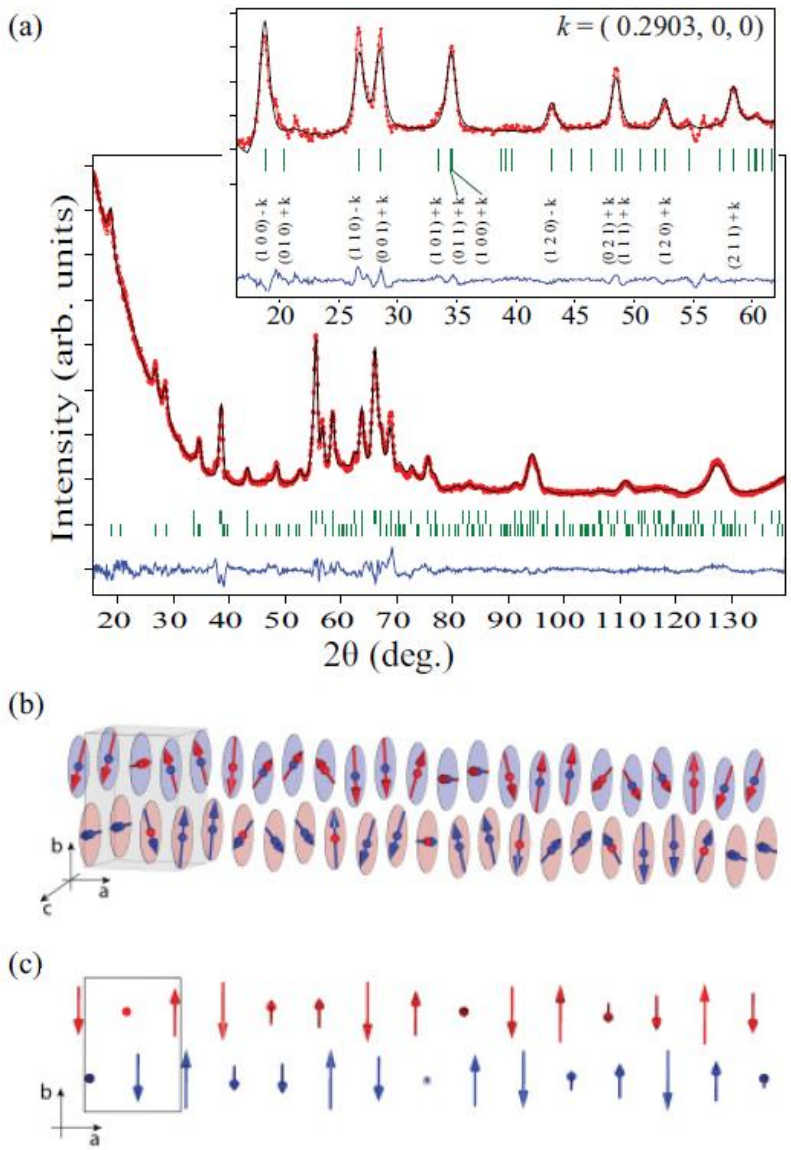


**Figure 3.10.** Incommensurate magnetic order of $MnVO_3$. (a) Fit of the nuclear and magnetic structures (upper and lower tick marks) to the D20 neutron powder diffraction profile of $MnVO_3$ at 1.7 K. The inset difference between 1.7 and 60 K patterns shows magnetic satellite reflections indexed by the propagation vector $k$ = (0.2903 0 0). Two ordering models give equivalent fits to the neutron data: (b) a helimagnetic spiral, in which all Mn moments have an equal magnitude of 3.5 $\mu_B$, and (c) a SDW of collinear moments parallel to the [011] plane, with an amplitude of 4.9 $\mu_B$.

The magnetic neutron diffraction intensities of $MnVO_3$ are not described well by a single spin corepresentation, but a good fit was obtained using a combination of $D_3(m_z)$ and $D_4(m_y)$ vectors of equal magnitude 3.45(14) $\mu_B$ at 1.7 K (Independent refinement gave insignificantly different values of 3.45(18) and 3.46(16) $\mu_B$ for the respective vectors, without improvement to the profile fit.) Each describes a sine-wave spin component, but the fits are inherently insensitive to the phase difference between the two vectors, leading to two descriptions of the spin structure (Figures 3.10.(b) and 3.10.(c)). An out-of-phase combination (e.g. $D_3 + iD_4$) generates a helical spin structure with a constant ordered Mn moment of 3.5(1) $\mu_B$ at 1.7 K, but an in-phase sum (e.g., $D_3 + D_4$) describes a sinusoidal spin density wave (SDW) of collinear moments with an amplitude of $\sqrt{2}\times 3.5 = 4.9(2)$ $\mu_B$, corresponding to the $Mn^{2+}$. Hence, both spin ordering ideal moment of 5 $\mu_B$ for $S = 5/2$ possibilities are physically realistic. The equal magnitudes of the $m_y$ and $m_z$ components suggest a helical order but do not exclude an SDW in the (011) plane. The ordered moment has the theoretical value for an SDW of $Mn^{2+}$ spins, but a reduced value of 3.5(1) $\mu_B$ is plausible in a helimagnet as spin order is partly frustrated. The fit of a critical law $m(T) = m(0)[1 - (T/T_N)]\beta$ to the magnetic moment $m$ in the temperature range $T_N/2 < T < T_N$ (Figure 3.11) gives $T_N = 46.3(6)$ K and $\beta = 0.32(3)$. The critical exponent agrees well with the theoretical value of 0.34 for a three-dimensional *xy*-magnet, which is appropriate to $MnVO_3$ because spins are constrained to lie in the *yz*-plane in both ordering descriptions. No *B*-site spin order was observed, but the possibility of a small ordered component at the V sites is not excluded by the present powder neutron diffraction measurements.

Helical spin structures are of interest because they can break inversion symmetry and generate coupled electrical and magnetic polarizations (multiferroicity), e.g., in the *B*-site manganite $TbMnO_3$ [20,21,22] However, the symmetry constraints for electrical polarization in Table 3.6 from ref. 21 show that the $D_3 + iD_4$ corepresentation of $MnVO_3$ belongs to the nonpolar point group 222, so no ferroelectric polarization is predicted from the helical model in Figure 3.10.(b). The observed metallic conductivity of $MnVO_3$ precludes measurement of electrical polarization.

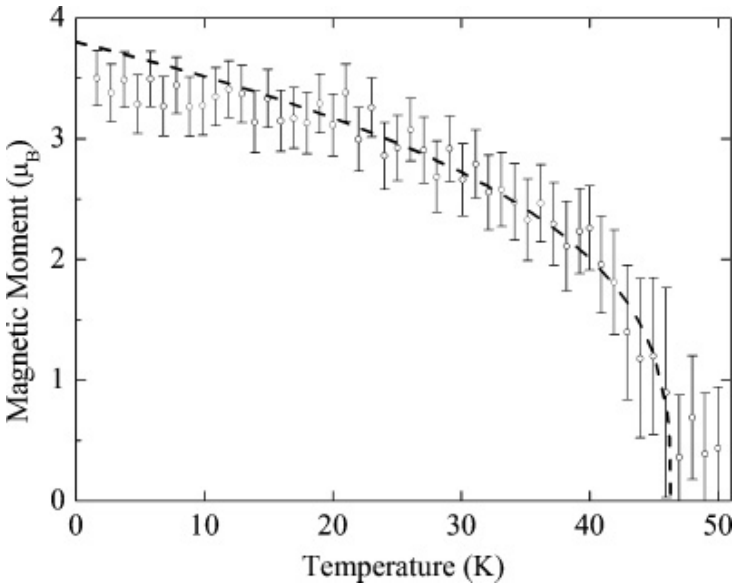


**Figure 3.11.** Variation of the ordered Mn moment (in the helical model of Figure 3.10.(b)) with temperature for $MnVO_3$, showing the critical law fit described in the text.

**Table 3.6.** Structural point groups for cycloidal structures of general formula $aD_\alpha + ibD_\beta$ (*a* and *b* are real coefficients.) The allowed direction of polarization is indicated in parentheses. A dot (.) means that the point group is nonpolar and no ferroelectric polarization can develop. Table taken from ref. 21.

| | $D_1$ | $D_2$ | $D_3$ | $D_4$ |
|---|---|---|---|---|
| $iD_1$ | $2mm(x)$ | $222(.)$ | $mm2(z)$ | $m2m(y)$ |
| $iD_2$ | $222(.)$ | $2mm(x)$ | $m2m(y)$ | $mm2(z)$ |
| $iD_3$ | $mm2(z)$ | $m2m(y)$ | $2mm(x)$ | $222(.)$ |
| $iD_4$ | $m2m(y)$ | $mm2(z)$ | $222(.)$ | $2mm(x)$ |

### 3.3.5. Band Structure Calculations

Electronic structure calculations within the local density approximation (LDA) were performed for the 300-K neutron model of $MnVO_3$ using the full-potential augmented planewave plus local-orbital method [23]. The muffin-tin sphere radii were 2.5, 2.0, and 1.5 Bohr for Mn, V, and O atoms, respectively. A cutoff energy of 12 Ryd was set for the plane-wave expansion of interstitial wave functions, and an 8 × 6 × 8 ***k***-mesh was used for integration over the first Brillouin zone. The calculated band structure (Figure 3.12) shows a large exchange splitting of the Mn 3*d* bands, giving rise to local $Mn^{2+}$ $S = 5/2$ spins, and the V 3*d* band has an apparent exchange splitting of ~1.0 eV. The $3d^1$ $V^{4+}$ band is almost completely spin polarized with an antiferromagnetic Mn-V exchange interaction, which was calculated to be more stable than the ferromagnetic Mn-V state by 20 meV/formula unit (f.u.). Thus, $MnVO_3$ is predicted to be a magnetic metal with localized majority $Mn^{2+}$ $S = 5/2$ spins and an itinerant minority spin $V^{4+}$ $3d^1$ band. However, an alternative magnetic ground state with a ferromagnetic Mn order and an A-type antiferromagnetic V order was found to have the same energy within 1 meV/f.u., suggesting that competing interactions are likely to be present in $MnVO_3$.

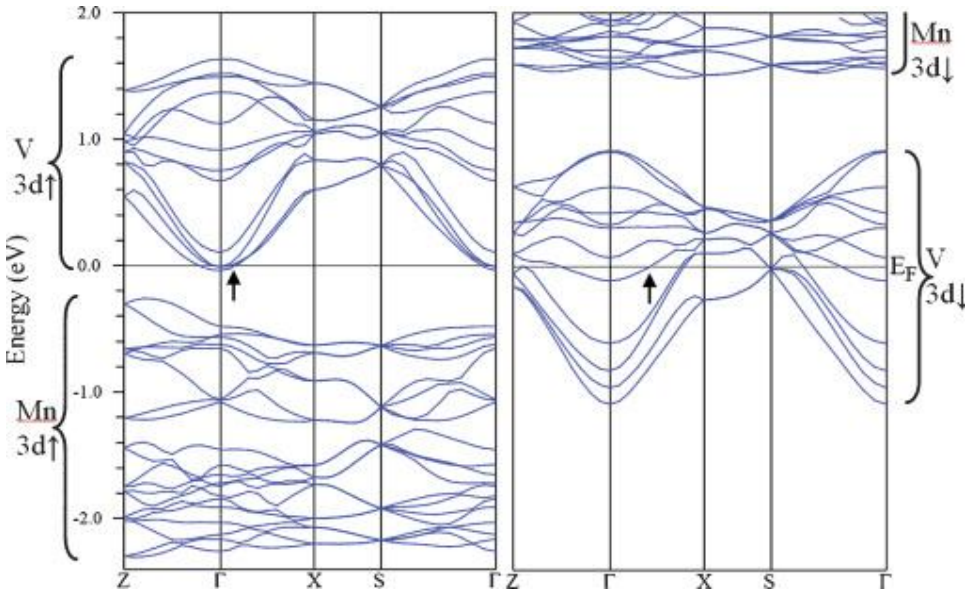


**Figure 3.12.** Spin up and down Mn 3*d* and V 3*d*($t_{2g}$) band dispersions (20 and 12 bands, respectively, for the *Pnma* cell containing four $MnVO_3$ units) from the LDA computed band structure. V 3*d*($t_{2g}$) bands crossing the Fermi energy at (*kx* 0 0) are marked by arrows on the Γ-X sections.

## 3.4. Discussion

Synchrotron x-ray studies revealed that the combined sample of several high pressure products contained two $MnVO_3$ components. This might be due to possible Mn/V disorder and some samples being non-stoichiometric.

The inconsistency in the results of ambient pressure resistivity measurements could be due to poor interparticle connections or grain boundaries caused by the $VO_2$ impurity and the existence of the two $MnVO_3$ components discovered in the synchrotron x-ray powder diffraction studies.

The results above show that $MnVO_3$ is a metallic oxide in which the V 3*d* band electrons remain itinerant down to at least 2 K over a wide pressure range and the $Mn^{2+}$ spins are localized and have magnetic transition to an incommensurate antiferromagnetic order at 46 K. The coupling mechanism between Mn spins is of particular interest because both insulating superexchange and itinerant electron RKKY scenarios are plausible. In an ideal cubic Mn*B*$O_3$ perovskite, each Mn cation

is connected to 12 next-nearest neighbors through linear Mn-O-Mn bridges that mediate the dominant antiferromagnetic superexchange interactions. These interactions are frustrated, but the *Pnma* distortion breaks the equivalence of many of the connections so that helical order can arise for a particular balance of superexchange strengths. However, the O 2*s* and 2*p* states that mediate Mn-O-Mn superexchange are also strongly hybridized with the V 3*d*($t_{2g}$) band, providing a mechanism for coupling the localized Mn $S$ = 5/2 spins to the V conduction electrons. The ($k_x$ 0 0) spin modulation results in a net magnetization at each V and O site as the surrounding Mn moments do not cancel to zero, although V atoms lie at the center of inversion symmetry in the *Pnma* structure. Hence, an RKKY interaction in which the Mn spins are indirectly coupled through their interaction with the V 3*d* conduction electrons is possible. This could favour the helical or SDW states. In an RKKY mechanism, the spin periodicity should match that of the conduction electrons at the Fermi level. LDA band structure in Figure 3.11 shows ($k_x$ 0 0) crossings of the Fermi surface by spin up and down V 3*d*($t_{2g}$) bands at $k_x$ = 0.15 and 0.45, respectively. Neither matches the observed $k_x$ = 0.29 spin modulation, although this does correspond to the difference between the two Fermi vectors. The present LDA results were obtained for a simple (0 0 0) ferromagnetic ordering of Mn moments, so a more self-consistent procedure is needed to evaluate whether the observed (0.29 0 0) magnetic vector matches a V 3*d*-band Fermi vector, because the V *d*-band structure is sensitive to the Mn exchange splitting and Mn-V spin coupling. Superexchange and RKKY couplings are not mutually exclusive - the Mn spin order in $MnVO_3$ may arise from cooperation or competition between the two interactions.

## 3.5. Conclusions

$MnVO_3$ has localized $Mn^{2+}$ $3d^5$ states in an unusual 8-coordination at the perovskite A sites and metallicity arising from the itinerant B site $V^{4+}$ $3d^1$ states. $MnVO_3$ is an unusual perovskite, because the ground state is determined by interactions of localized *A*-site $Mn^{2+}$ $3d^5$ and itinerant *B*-site$V^{4+}$ $3d^1$ electrons. Alternative helical and SDW models for the observed (0.29 0 0) Mn magnetic order are both physically plausible, and the exchange interactions are likely to involve both

Mn-O-Mn superexchange and RKKY coupling through the V *d*-band. Because of the nonpolar point group (222) and metallicity, no ferroelectric polarization was expected like in $TbMnO_3$ which has same space group. The existence of two $MnVO_3$ phases and the difficulties in conductivity measurements suggests that some samples of $MnVO_3$ were non-stoichiometric ($MnV_{1-x}Mn_xO_3$).

## 3.6. References


1. R. H. Mitchell, *Perovskites: Modern and Ancient*, Almaz Press Inc., Ontario (2002).
2. C. N. R. Rao, *Transition Metal Oxides*, 2nd Edition, John Wiley & Sons, (1998).
3. A. M. Glazer, *Acta Cryst.*, **B28**, 3384 (1972).
4. A. J.Williams, A. Gillies, J. P. Attfield, G. Heymann, H. Huppertz, M. J. Martinez-Lope and J. A. Alonso, Phys. Rev. B **73**, 104409 (2006).
5. J. S. Zhou, C. Q. Jin,Y.W. Long, L. X.Yang, and J. B.Goodenough, Phys. Rev. Lett. **96**, 046408 (2006).
6. L. O. SanMartin, A. J. Williams, J. Rodgers, J. P. Attfield, G. Heymann, and H. Huppertz, Phys. Rev. Lett. **99**, 255701 (2007).
7. S. A. J. Kimber, J. A. Rodgers,H.Wu, C. A. Murray, D. N. Argyriou, A. N. Fitch, D. I. Khomskii, and J. P. Attfield, Phys. Rev. Lett. **102**, 046409 (2009).
8. J. G. Cheng, J. S. Zhou, and J. B. Goodenough, Phys. Rev. B **80**, 174426 (2009).
9. I. A. Nekrasov, G. Keller, D. E. Kondakov, A. V. Kozhevnikov, Th. Pruschke, K. Held, D. Vollhardt, and V. I. Anisimov, Phys. Rev. B **72**, 155106 (2005).
10. T. Yoshida, M. Hashimoto, T. Takizawa, A. Fujimori, M. Kubota, K. Ono, and H. Eisaki, Phys. Rev. B **82**, 085119 (2010).
11. I. H. Inoue, C. Bergemann, I. Hase, and S. R. Julian, Phys. Rev. Lett. **88**, 236403 (2002).
12. B. L. Chamberland and P. S. Danielson, J. Solid State Chem. **10**, 249 (1974).

13. R. V. Shpanchenko, V. V. Chernaya, A. A. Tsirlin, P. S. Chizhov, D. E. Sklovsky, E. V. Antipov, E. P. Khlybov, V. Pomjakushin, A. M. Balagurov, J. E. Medvedeva, E. E. Kaul, and C. Geibel, Chem. Mater. **16**, 3267 (2004).
14. A. A. Belik, M. Azuma, T. Saito, Y. Shimakawa, and M. Takano, Chem. Mater. **17**, 269 (2005).
15. A. Kumar, L. W. Martin, S. Denev, J. B. Kortright, Y. Suzuki, R. Ramesh, and V. Gopalan, Phys. Rev. B **75**, 060101(R) (2007).
16. A. Kumar, N. J. Podraza, S. Denev, J. Li, L. W. Martin, Y. Chu, R. Ramesh, R. W. Collins, and V. Gopalan, Appl. Phys. Lett. **92**, 231915 (2008).
17. Y. Syono, S. Akimoto, and Y. Endoh, J. Phys. Chem. Solid. **32**, 243 (1971).
18. A.C. Larson and R.B. Von Dreele, Los Alamos National Laboratory Report no. LAUR 86-748 (1994) (unpublished).
19. J. Rodriguez-Carvajal, Phys. B **192**, 55 (1993).
20. M. Kenzelmann, A. B. Harris, S. Jonas, C. Broholm, J. Schefer, S. B. Kim, C. L. Zhang, S. W. Cheong, O. P. Vajk, and J. W. Lynn, Phys. Rev. Lett. **95**, 087206 (2005).
21. P. G. Radaelli and L. C. Chapon, Phys. Rev. B **76**, 054428 (2007).
22. A. B. Harris, Phys. Rev. B **76**, 054447 (2007).
23. P. Blaha, K. Schwarz, G. Madsen, D. Kvasnicka, and J. Luitz, WIEN2K code [http://www.wien2k.at].

# Chapter 4. Synthesis and characterisation of orthorhombic high-pressure $CoVO_4$

## 4.1. Introduction

Orthovanadates ($AVO_4$, where A is a trivalent element) have not been generally studied much except for some tetragonal zircon-type compounds such as $GdVO_4$ [1] and $YVO_4$ [2], which have recently become the object of great interest as promising optical materials for birefringent solid-state laser applications. Most of the orthovanadates ($AVO_4$ where *A* = Sm, Eu, Gd, Dy, La, Sc, Y, Ce, Pr, Nd, Tb, Ho, Er, Tm, Yb or Lu) crystallise in a tetragonal zircon type structure (space group: $I4_1/amd$) [3,4,5,6] Some exceptions to this structure are seen in triclinic $AlVO_4$ [7], tetragonal scheelite-type $BiVO_4$ (space group: $I4_1/a$) [8], monoclinic $InVO_4$ (space group: *C2/m*) [9] and orthorhombic $CrVO_4$ (space group *Cmcm*). $FeVO_4$ is the only orthovanadate besides $CoVO_4$ which has been reported [10] to crystallise in *Pbcn* space group. $FeVO_4$ exists also in triclinic, orthorhombic (space group *Cmcm*) and monoclinic wolframite phases depending on the pressure used in the synthesis [10]. Among the $ABO_4$ structure type there are only three other compounds crystallising in space group *Pbcn*, namely $ZrTiO_4$, $ZrSnO_4$ and $HfTiO_4$ [11,12]. Spinel structured $Li_xCoVO_4$ (x = 0.8, 1.0 or 1.2) has been much studied in batteries, but a compound with x = 0 has never been prepared [13,14].

The synthesis and characterisation of a previously unreported orthorhombic α-$PbO_2$ type $CoVO_4$ compound, which crystallises in *Pbcn* space group is reported here.

## 4.2. Experimental

The α-$PbO_2$ type $CoVO_4$ was first obtained accidentally when a precursor $CoV_2O_7$ was pressed at 10 GPa pressure and 1100°C temperature (Figure 4.1). The most prominent peaks in the X-ray diffraction profile matched well with orthorhombic $AVO_4$ type compounds, and it was concluded that the phase could be $CoVO_4$. The rest of the peaks gave a good match with corundum structured compounds, and the phase was identified as $CoVO_3$. To remove the secondary phase, $KClO_3$ (Aldrich, ≥ 99%) was added as an oxidiser. The best results were achieved by grinding stoichiometric quantities of $Co_3O_4$ (Aldrich, 99.995%) and $V_2O_5$ (Aldrich, 99.99%) in a mortar and adding double or triple excess of $KClO_3$ before pressing the mixture in the Walker module (see section 2.1.2) at 10 GPa and 1100°C for 5 – 15 min with quenching. The synthesis was also tried by first making the precursor $CoV_2O_7$ by heating $Co_3O_4$ (Aldrich, 99.995%) and $V_2O_5$ (Aldrich, 99.99%) in a furnace in air at 650°C for 21 hours and then adding the oxidiser before the above described high-pressure synthesis. The oxidiser $KClO_3$ was removed by washing with water. The yields of $CoVO_4$ were approximately 70 % by both methods. Magnetic susceptibility data were recorded using a Quantum Design SQUID magnetometer (see section 2.3) The synchrotron x-ray powder diffraction studies were carried out at ESRF on ID31 (see section 2.2.3) high resolution powder diffraction beamline using 0.399 Å wavelength. Powder neutron diffraction measurements were performed on a high intensity and resolution time-of-flight neutron diffractometer GEM (see section 2.2.3). The refinement of x-ray and neutron diffraction data was done using GSAS software package [15].

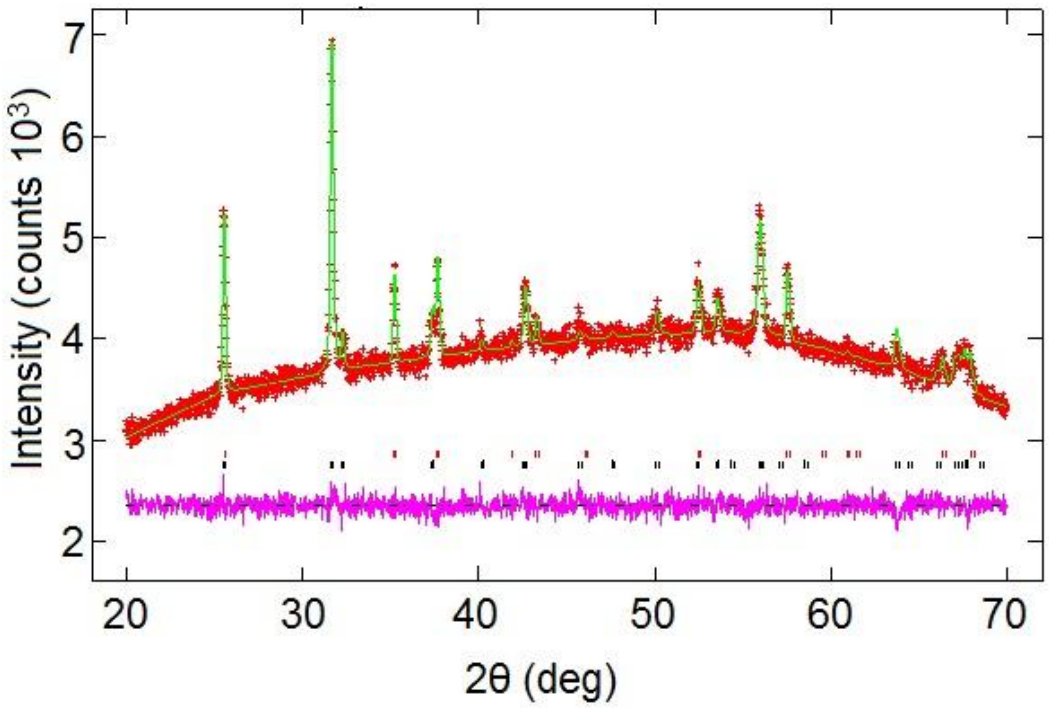


**Figure 4.1.** Laboratory powder x-ray diffraction profile for orthorhombic α-$PbO_2$ type $CoVO_4$. The upper Bragg reflection markers correspond to the corundum structured impurity phase and the lower ones to $CoVO_4$.

## 4.3. Results

### 4.3.1. Magnetisation measurements

The non-linear fit to the inverse susceptibility data at 0.5 Tesla between 150 and 334 K, (Figure 4.2) gave an effective magnetic moment of 3.53 $\mu_B$ and Weiss temperature of -11.8 K. The corundum structured $CoVO_3$ impurity phase, which accounted for approximately 30 % of the sample, was assumed to have similar magnetisation properties to $CoVO_3$ ilmenite with high-spin $Co^{2+}$. When $CoVO_4$ is taken to be non-magnetic with $Co^{3+}$ in a low spin state, the expected effective magnetic moment from the $CoVO_3$ impurity phase would be approximately 2.9 $\mu_B$. If $Co^{3+}$ in $CoVO_4$ were in a high spin state, we should expect an effective magnetic moment of approximately 5 $\mu_B$ from the mixture of the two phases.

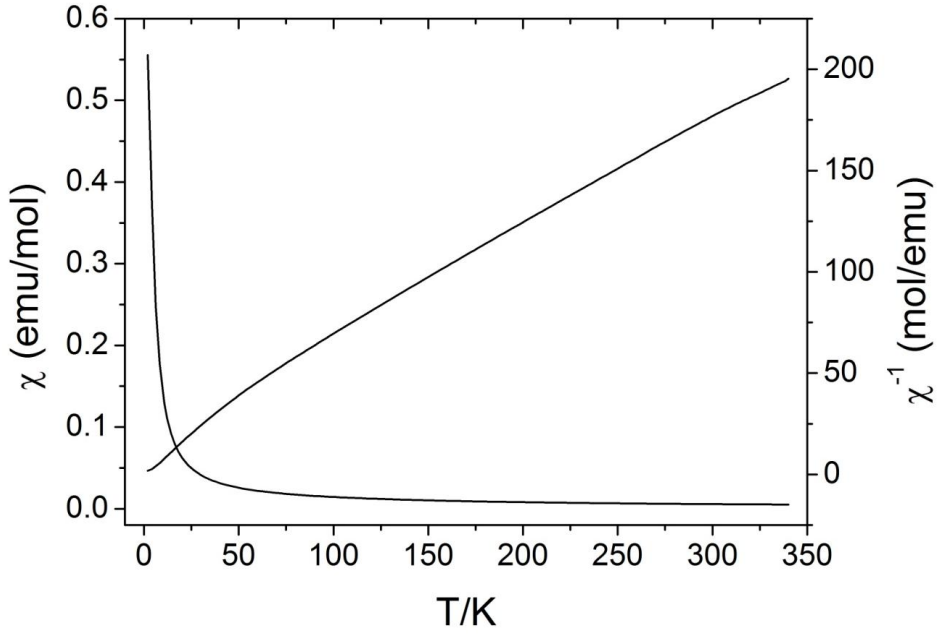


**Figure 4.2**. Magnetic susceptibility and inverse susceptibility measurements in a 0.5 T magnetic field for orthorhombic α-$PbO_2$ type $CoVO_4$ with corundum structured $CoVO_3$ impurity phase accounting for 30 % of the sample.

### 4.3.2. Neutron and Synchrotron X-ray powder diffraction

Besides determining the lattice parameters, the purpose of the neutron and synchrotron X-ray powder diffraction measurements was to find out the correct structure type for this new compound. From the refinements using the laboratory X-ray powder diffraction data, it could be concluded that tetragonal or triclinic $AVO_4$ type structures did not match with the new compound but it was not possible to see whether orthorhombic $PbO_2$ type structure (*Pbcn* space group) with cation disorder or monoclinic $FeWO_4$ type structure (*P2/c* space group) with cation order gave a better fit. The synchrotron x-ray powder diffraction profile from the instrument ID31 fitted in the monoclinic *P2/c* space group (Figure 4.3) showed that no splittings or superstructure peaks were present in the high d-spacing region, and that profile did not match well with the calculated model.

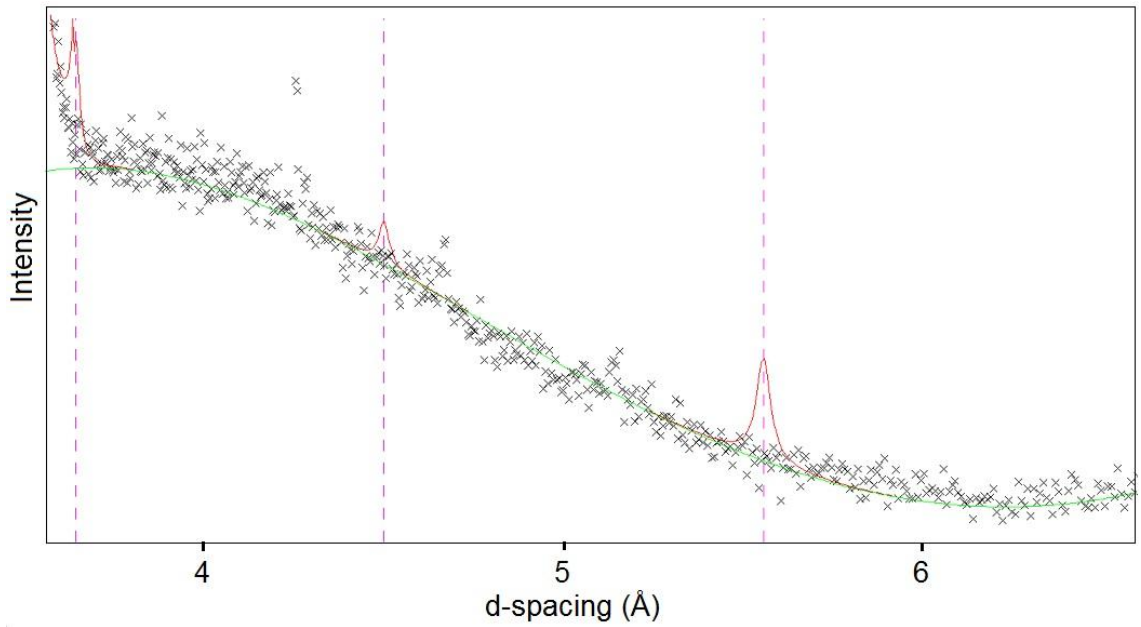


**Figure 4.3.** Expansion of the synchrotron X-ray powder diffraction profile from the instrument ID31 for orthorhombic α-$PbO_2$ type $CoVO_4$ using monoclinic wolframite type calculated model. The mismatch of the model (red lines) with the profile shows that $CoVO_4$ does not crystallise in a monoclinic P2/c space group.

Figure 4.4. presents the crystal structure of α-$PbO_2$ type $CoVO_4$ with corner and edge sharing zig-zag chains of $MO_6$ octahedra (M = Co or V) along the c-axis.

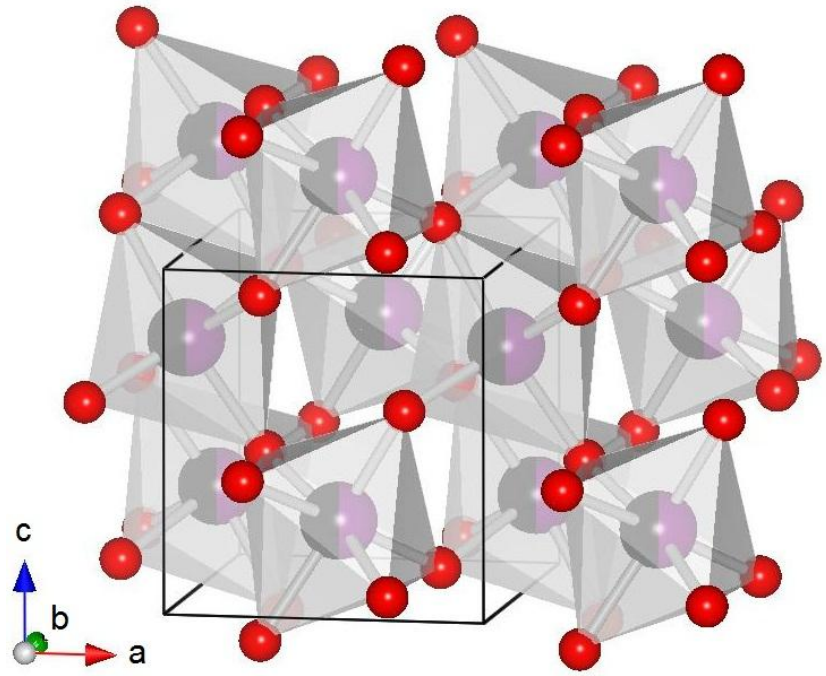


**Figure 4.4.** The structure of α-$PbO_2$ type $CoVO_4$. Larger spheres represent either vanadium or cobalt and smaller ones oxygen.

As the neutron scattering lengths for Co and V are very different (2.49 and -0.46 fm for Co and V respectively), the comparison of the refinements of the neutron diffraction data in *Pbcn* and *P2/c* space groups could also reveal the correct space group. When a *Pbcn* space group was used, the refinement converged easily, but with *P2/c* space group the values of the thermal displacement parameters were not converging. The fit to the neutron diffraction profile from the instrument GEM using *Pbcn* space group (Figure 4.5) was used for the determination of the lattice parameters, atomic coordinates and bond lengths (Tables 4.1 and 4.2).

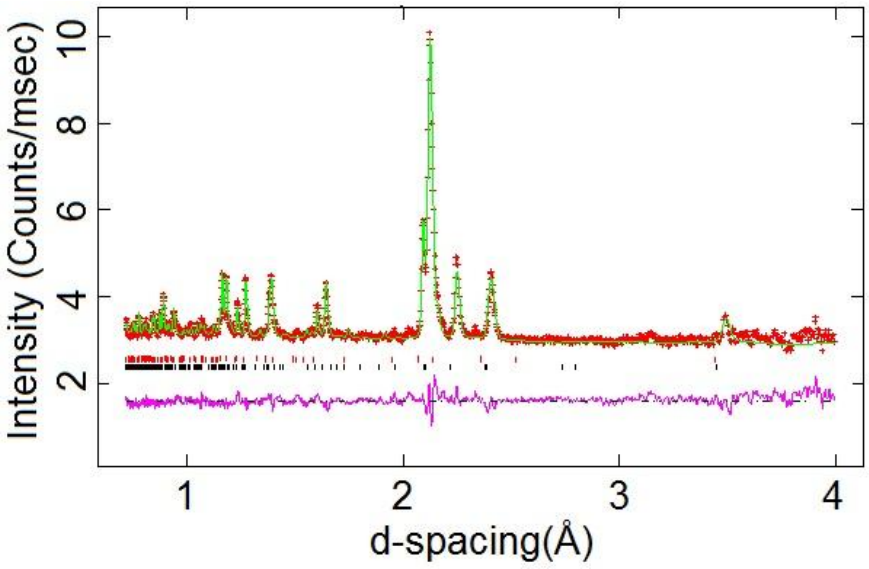


**Figure 4.5.** Fit to the neutron diffraction profile from the 63.6° detector of instrument GEM for orthorhombic α-$PbO_2$ type $CoVO_4$. The upper Bragg reflection markers correspond to the corundum structured impurity phase and the lower ones to $CoVO_4$.

**Table 4.1.** Refined lattice parameters, atomic coordinates and thermal displacement parameters from refinement of the $CoVO_4$ in space group *Pbcn* at 295 K at instrument GEM. Fitting residuals, $R_{wp}$, and $\chi^2$, were 0.027 and 1.406 respectively.

| a (Å) | b (Å) | c (Å) | Volume (Å$^3$) | |
|---|---|---|---|---|
| 4.4934(4) | 5.5436(6) | 4.8310(5) | 120.34(3) | |
| Atom | x | y | z | $U_{iso}$(Å$^2$) |
| Co/V | 0 | 0.6994(23) | 0.25 | 0.0088(2) |
| O | 0.7260(5) | 0.8857(6) | 0.0883(7) | 0.0088(2) |

The calculated bond lengths for Co/V-O, when $Co^{3+}$ is in high spin or low spin state are 1.9375 Å and 1.9025 Å respectively. The experimental mean value for Co/V-O bond is 1.976(7) Å as presented in Table 4.2.

**Table 4.2.** Selected interatomic distances (Å) for orthorhombic $CoVO_4$ from refinement at 300 K at instrument GEM. Mean distances are shown as <M-O>.

| $CoVO_4$ | 295 K |
|---|---|
| Bond | Length (Å) |
| Co/V-O × 4 | 1.787(7) |
| Co/V-O × 4 | 1.981(4) |
| Co/V-O × 4 | 2.160(10) |
| <Co/V-O> | 1.976(7) |
| Angle | Degrees |
| O-Co/V-O × 2 | 89.05(15) |
| O-Co/V-O × 2 | 98.34(17) |
| O-Co/V-O × 2 | 97.48(15) |
| O-Co/V-O | 109.4(7) |
| O-Co/V-O × 2 | 161.4(5) |
| O-Co/V-O × 2 | 82.28(33) |
| O-Co/V-O × 2 | 75.58(32) |
| O-Co/V-O | 72.8(4) |
| O-Co/V-O | 152.5(7) |
| Co/V-O-Co/V × 2 | 129.15(25) |
| Co/V-O-Co/V × 4 | 125.18(17) |
| Co/V-O-Co/V × 2 | 104.42(32) |

## 4.4. Discussion and conclusions

The experimental average Co/V-O bond length is considerably longer than the calculated values when $Co^{3+}$ is in high spin or low spin state. Co/V disorder is probably preventing a reliable determination of spin state from the mean bond distance. The magnetic susceptibility measurements gave an effective magnetic moment value which is closer to the value expected when the $Co^{3+}$ is in a low spin state, and most likely this is the spin state of $Co^{3+}$ in $CoVO_4$.

In comparison to other $AVO_4$ compounds with a transition metal in the *A*-site, $CoVO_4$ is the only compound that exists only as a high pressure phase. $CrVO_4$ is orthorhombic (space group C*mcm*) in ambient pressure and transforms to the rutile structure at high pressure [16]. The ambient pressure structure consists of infinite chains of *trans* edge-sharing $CrO_6$ octahedra which run parallel to the *c*-axis compared to the corner and edge sharing zig-zag chains of $MO_6$ octahedra (M = Co or V) along the c-axis in $CoVO_4$. Both $YVO_4$ and $ScVO_4$ have a zircon structure at ambient pressure and scheelite structure at high pressure [16]. In the zircon structure, the vanadium atom is tetrahedrally coordinated while the trivalent metal is coordinated to eight oxygen atoms [17]. The V-O bond lengths in zircon structured $YVO_4$ and $ScVO_4$, 1.64 and 1.74 Å [18] respectively are much shorter than the Co/V-O bonds in $CoVO_4$ which have a mean length of 1.98 Å. $FeVO_4$ is the only orthovanadate besides $CoVO_4$ which has been reported to crystallise in *Pbcn* space group but unfortunately this high pressure phase of $FeVO_4$ has not been much studied.

The previously unreported orthorhombic $CoVO_4$ crystallising in the *Pbcn* space group has been characterised by magnetisation, neutron and synchrotron x-ray powder diffraction studies. Improving the synthesis of $CoVO_4$ would be the next step for the study of this compound.

## 4.5. References

1. S. Miyazawa, Optoelectron. Rev. **11**, 77, (2003).
2. W. Ryba-Romanowski, Cryst. Res. Technol. **38**, 225 (2003).
3. D. Errandonea, R. Lacomba-Perales, J. Ruiz-Fuertes, A. Segura, S. N. Achary and A. K. Tyagi, http://arxiv.org/ftp/arxiv/papers/0905/0905.1206.pdf
4. D. F. Mullica, E. L. Sappenfield, M. M. Abraham, B. C. Chakoumakos and L. A. Boatner, Inorg. Chimica Acta **248**, 85 (1996).
5. A. T. Aldred, Acta Cryst. B **40**, 569 (1984).
6. B. C. Chakoumakos, M. M. Abraham and L. A. Boatner, J. Sol. State Chem. **109**,

197 (1994).

7. U. G. Nielsen, A. Boisen, M. Brorson, C. J. H. Jacobsen, H. J. Jakobsen and J. Skibsted, Inorg. Chem. **41**, 6432 (2002).
8. A. W. Sleight, H. Y. Chen, A. Ferreti, and D. E. Cox, Mater. Res. Bull. **14**, 1571 (1979).
9. M. Touboul, K. Melghit, P. Benard, and D. Loues, J. Sol. State Chem. **118**, 93 (1985).
10. Y. Oka, T. Yao, N. Yamamoto, Yutaka Ueda, S. Kawasaki, M. Azuma and M. Takano, J. Sol. State Chem. **123,** 54–59 (1996).
11. D. Errandonea, D. Santamaria-Perez, T. Bondarenko and O. Khyzhun, http://arxiv.org/ftp/arxiv/papers/1008/1008.4675.pdf
12. J. S. Lakshmi, J.I. Berlin, J. K. Thomas, P. V. Thomas and K. Joy, IOP Conference Series: Mat. Science Engineer. **23** 1 012030 (2011).
13. M. S. Bhuvaneshwari, S. S. Subramanian, ECS Trans. **1**, 26 (2006).
14. M. S. Bhuvaneshwari, S. S. Subramanian, S. Fujihara and S. Koji, Sol. State Ionics **177,** 1 (2006).
15. A.C. Larson and R.B. Von Dreele, Los Alamos National Laboratory Report no. LAUR 86-748 (1994) (unpublished).
16. O. Fukunaga and S. Yamaoka, Phys. Chem. Minerals **5**, 167 (1979).
17. V. Panchal, F. J. Manjon, D. Errandonea, P. Rodriguez-Hernandez, J. Lopez-Solano, A. Munoz, S. N. Achary and A. K. Tyagi, Phys. Rev. B **83** 064111 (2011).
18. W.O. Milligan and L. W. Vernon, J. Phys. Chem. **56** (1) 145–147 (1952).

# Chapter 5. Spin orders of monoclinic brannerite type $CoV_2O_6$ at different magnetisation states

## 5.1. Introduction

The structure of monoclinic $CoV_2O_6$ is closely related to that of brannerite, $UTi_2O_6$, both crystallising in space group C2/m. There exists also a triclinic brannerite type $CoV_2O_6$ polymorph [1]. Both polymorphs are one-dimensional materials with high spin $Co^{2+}$ in edge-sharing chains of $CoO_6$ octahedra along the b-axis, connected by chains of corner and edge sharing $VO_6$ octahedra in the monoclinic phase (Figure 5.1) and by $VO_6$ octahedra and $VO_4$ tetrahedra in the triclinic phase. $V^{5+}$ ions have been described as being 5 + 1 coordinated in monoclinic brannerites because the sixth oxygen atom is weakly bonded at distances of 2.4 - 2.8 Å [2].

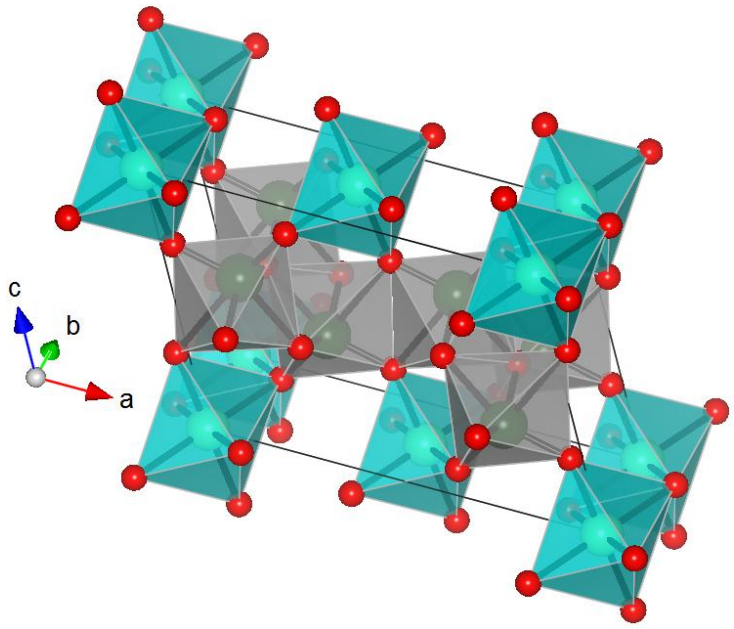


**Figure 5.1.** Structure of a monoclinic, brannerite type $CoV_2O_6$. Blue octahedra present $CoO_6$ and violet octahedra $VO_6$.

Mixed oxides containing magnetic and nonmagnetic transition metals are a good source of low-dimensional crystal structures as $d^0$ $V^{5+}$ in particular can adopt a range of coordinations. Large single-ion anisotropy leads to Ising-like behaviour of the high spin $Co^{2+}$ S = 3/2 spins in brannerite type $CoV_2O_6$. Low-dimensional lattices of Ising spin ions are of great interest for the variety of quantum magnetic ground states and unusual excitations that may emerge. Phenomena such as metamagnetism and intermediate magnetisation plateaus which are more commonly observed in frustrated triangular systems [3,4,5] have been predicted and observed experimentally also in spin-3/2 antiferromagnetic uniform chains [3,6]. Recently metamagnetism and 1/3 magnetization plateau (Figure 5.2) have been reported in brannerite type monoclinic and triclinic $CoV_2O_6$ polymorphs [1,7,8,9,10,11,12,13], both containing one-dimensional ferromagnetic chains of high spin $Co^{2+}$ ions.

Besides the $CoV_2O_6$ polymorphs, the magnetic properties of other brannerite type $MV_2O_6$ transition metal vanadates (M = Mn [8,14,15], Ni [8,9], Cu [8,9,16,17,18,19] have been widely studied. Moreover studies on the electrochemical [20] and catalytic [21] properties of brannerite type $CoV_2O_6$ have been published.

The field induced 1/3 magnetisation plateau in monoclinic $CoV_2O_6$ was first reported by He *et al.* [10] in 2009. Magnetodielectric coupling and magnetisation plateaus in the monoclinic $CoV_2O_6$ were studied by Singh *et al.* [12]. A Wang-Landau simulation in reference 13, treating the monoclinic lattice of $CoV_2O_6$ as a distorted triangular system, showed that the ⅓-magnetization plateau derives from the same field-induced ferrimagnetic state as observed in a regular frustrated antiferromagnetic triangular system, but with a different behaviour of the critical fields due to the relaxation of magnetic frustration by anisotropy. Lenertz *et al.* [11] have compared the magnetic properties of the monoclinic and triclinic phases of $CoV_2O_6$. They reported monoclinic $CoV_2O_6$ to have an antiferromagnetic transition at $T_N \approx 15$ K (triclinic $T_N \approx 7$ K). Two field induced transitions were found: to a 1/3 magnetisation plateau between 1.9 and 3.2 T (in triclinic between 0.45 and 0.6 T) and to a metamagnetic transition of full saturation magnetisation at 4 T (triclinic 0.61 T), both measured at 1.8 K. The saturation moment of 4.5 $\mu_B$ at 5 K and 4 T was considerably larger than the expected spin-only value of 3 $\mu_B$, for high spin $Co^{2+}$,

indicating a significant orbital contribution to the moment. For the triclinic phase a saturation moment of 2.8 $\mu_B$ at 5 K and 7 T was reported.

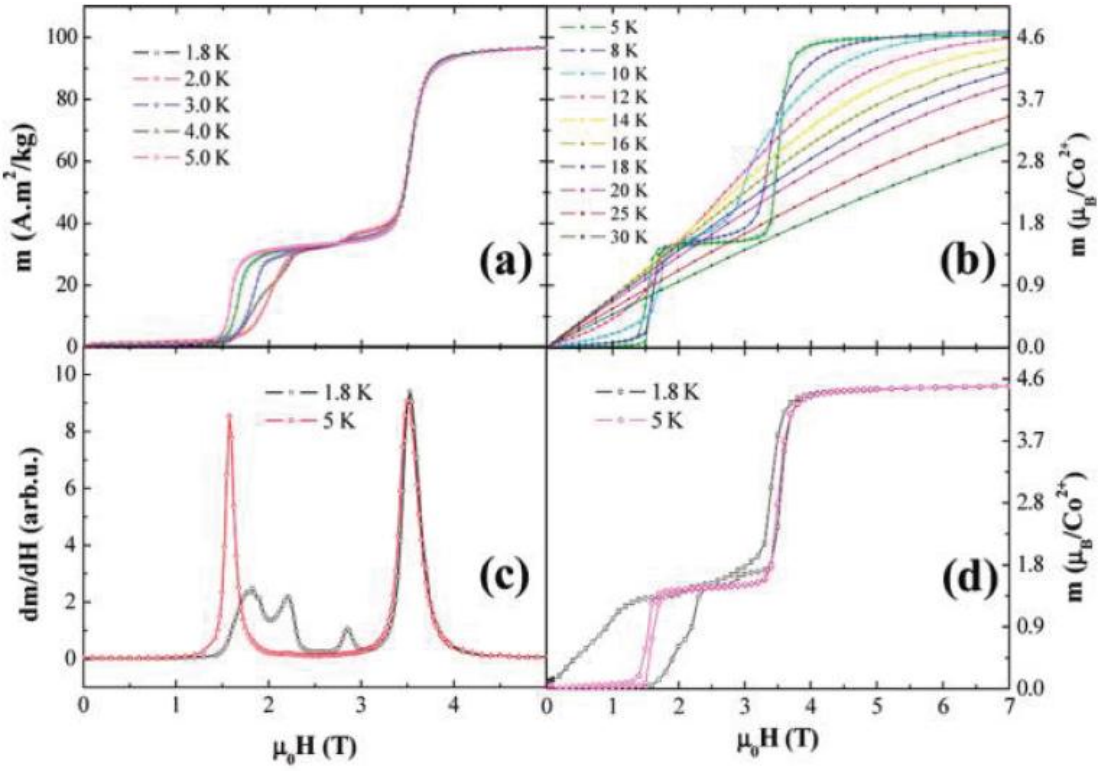


**Figure 5.2**. First magnetization curves of monoclinic $CoV_2O_6$ recorded while increasing the field from zero to saturation for temperatures below (a) and above (b) 5 K. Derivate of the first magnetization curve recorded at 1.8 and 5 K (c) and magnetization hysteresis loop recorded at 1.8 and 5 K (d). Figure taken from reference 11.

Magnetisation and neutron scattering measurements for the triclinic $CoV_2O_6$ phase have recently been reported [1]. Similar transitions to the monoclinic phase were found: an antiferromagnetic transition at $T_N$ = 6.3 K, onset of 1/3 magnetisation plateau at 0.36 T and a transition at 0.59 T to full magnetisation, both at 2 K. A saturation moment of 2.9 $\mu_B$ at 2 K and 9 T was reported. Inelastic neutron scattering showed that the magnetic excitations above $T_N$ are unusual solitons (localized excitations propagating in a system with constant velocity) rather than the static spin reversals predicted for a uniform ferromagnetic Ising spin chain. Below $T_N$, a ladder

of states due to the confining effect of the spin order was found, with weak confinement at 5 K < T < $T_N$ which may correspond to a crossover between two- and three-dimensional magnetic ordering. However, powder neutron diffraction showed that the low temperature magnetic order was incommensurate and the full spin structure was not reported.

Models for the spin order in the ⅓-magnetisation phase in monoclinic $CoV_2O_6$ have been predicted in recent papers [12,13]. The experimental spin structures of the off-field, ⅓-magnetization and the fully saturated phases are reported here.

The off-field magnetic structure was solved working with Dr. Angel Arevalo-Lopez.

## 5.2. Experimental

A 3 g polycrystalline sample of monoclinic $CoV_2O_6$ was synthesised by grinding stoichiometric quantities of cobalt (II) acetate tetrahydrate (Aldrich, 99.99 %) and $V_2O_5$ (Aldrich, 99.99 %) in a mortar and then heating in a furnace in air. The sample was heated for 16 h at 650 °C and then for 48 h at 725 °C, followed by quenching in liquid nitrogen. Quenching is needed to avoid formation of the triclinic form. Laboratory powder x-ray diffraction (see section 2.2.3) using Cu $K_\alpha$ radiation showed that only monoclinic $CoV_2O_6$ was present (Figure 5.3) in the sample. For the neutron diffraction measurements in magnetic field, the powder was cold pressed into pellets which were then placed in a vanadium sample can. Magnetic susceptibility data were recorded using a Quantum Design SQUID magnetometer (see section 2.3).

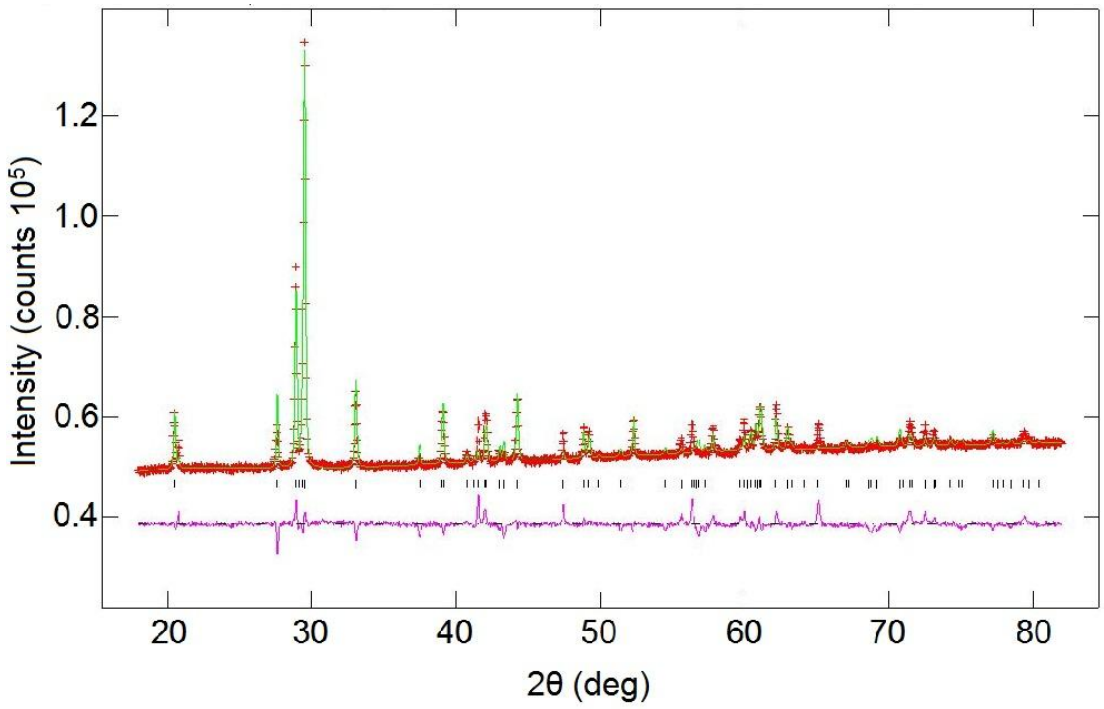


**Figure 5.3.** Laboratory powder x-ray diffraction profile for monoclinic $CoV_2O_6$.

Powder neutron diffraction patterns from the 3 g monoclinic $CoV_2O_6$ sample were measured using the high-resolution time-of-flight neutron diffractometer HRPD (see section 2.2.3) at the ISIS spallation source. Data were collected at 4 K, 10-50 K in 5 K intervals, and 60-300 K in 20 K intervals. Further powder neutron diffraction patterns in magnetic field were collected using the long-wavelength, time-of-flight neutron diffractometer WISH (see section 2.2.3) at ISIS. Data were collected at 2 K at a 0 → 2.5 T → 5.0 T → 0 sequence of applied magnetic field strengths. The final zero field data were recorded to check for any alignment of sample grains by the applied fields. Data were normalised using the MantidPlot program [22], which was also used for creating the figures, and crystal and magnetic structures were refined using the GSAS software package [23].

## 5.3. Results

### 5.3.1. Magnetisation measurements

Results on the magnetic susceptibility measurements were in line with the other studies [10,11,12] and showed monoclinic $CoV_2O_6$ to be a Curie-Weiss paramagnet at high temperatures and to have an antiferromagnetic transition at $T_N$ = 15 K (Figure 5.4). The inverse susceptibility curvature above $T_N$ reveals short range antiferromagnetic fluctuations, but a fit to inverse susceptibility data between 280 and 300 K gives a Weiss temperature of 42.1 K which shows that the strongest exchange interactions are ferromagnetic. The fitted paramagnetic moment of 6.09 $\mu_B$ is considerably larger than the spin-only value for high spin $Co^{2+}$ of 3.87 $\mu_B$, indicating that there is a large orbital contribution.

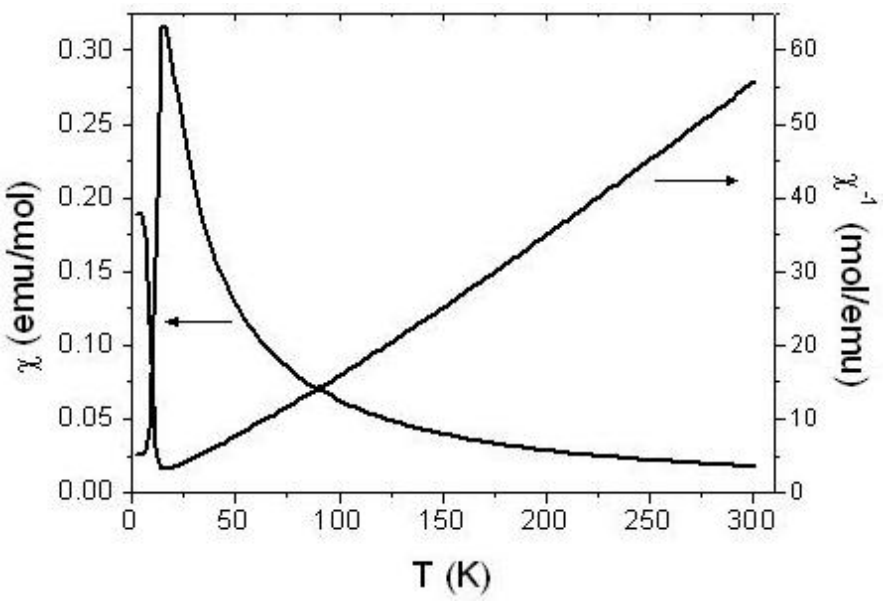


**Figure 5.4.** Magnetic susceptibility measurements for monoclinic $CoV_2O_6$ in a 1 T field.

### 5.3.2. Neutron powder diffraction

**a) Zero-field measurements at instrument HRPD**

The nuclear diffraction intensities were fitted well by refining the structure in space group *C2/m*, and no significant improvements were obtained by lowering the symmetry to acentric *C2* as was originally reported for monoclinic $CoV_2O_6$ [7]. Figure 5.5 shows the fits to the 300 K data.

Small spurious peaks at d-spacings of 1.1, 1.3, 1.8 and 2.1 Å are seen in the profile from the $2\theta = 90°$ detector bank, but not in the backscattering ($2\theta = 168°$) data, showing that the additional peaks are from parasitic scattering in the 90° detector flight path rather than an impurity phase. Possible Co/V inversion disorder was investigated but the cation sites were found to be fully occupied to within 2 % experimental uncertainties. Refined atomic coordinates, lattice and thermal displacement parameters and selected interatomic distances and bond angles from 4 and 300 K refinements are reported in Tables 5.1 - 5.3. Bond valence sums derived from the 300 K distances in Table 5.1. using standard $Co^{2+}$- O and $V^{5+}$- O parameters [24] are Co 1.96; V 5.24; O(1) 2.09; O(2) 2.01; and O(3) 2.12. The proximity of these values to the formal valences indicates that the crystal structure is accurately determined and is relatively unstrained despite the distorted octahedral coordinations around the two cation sites.

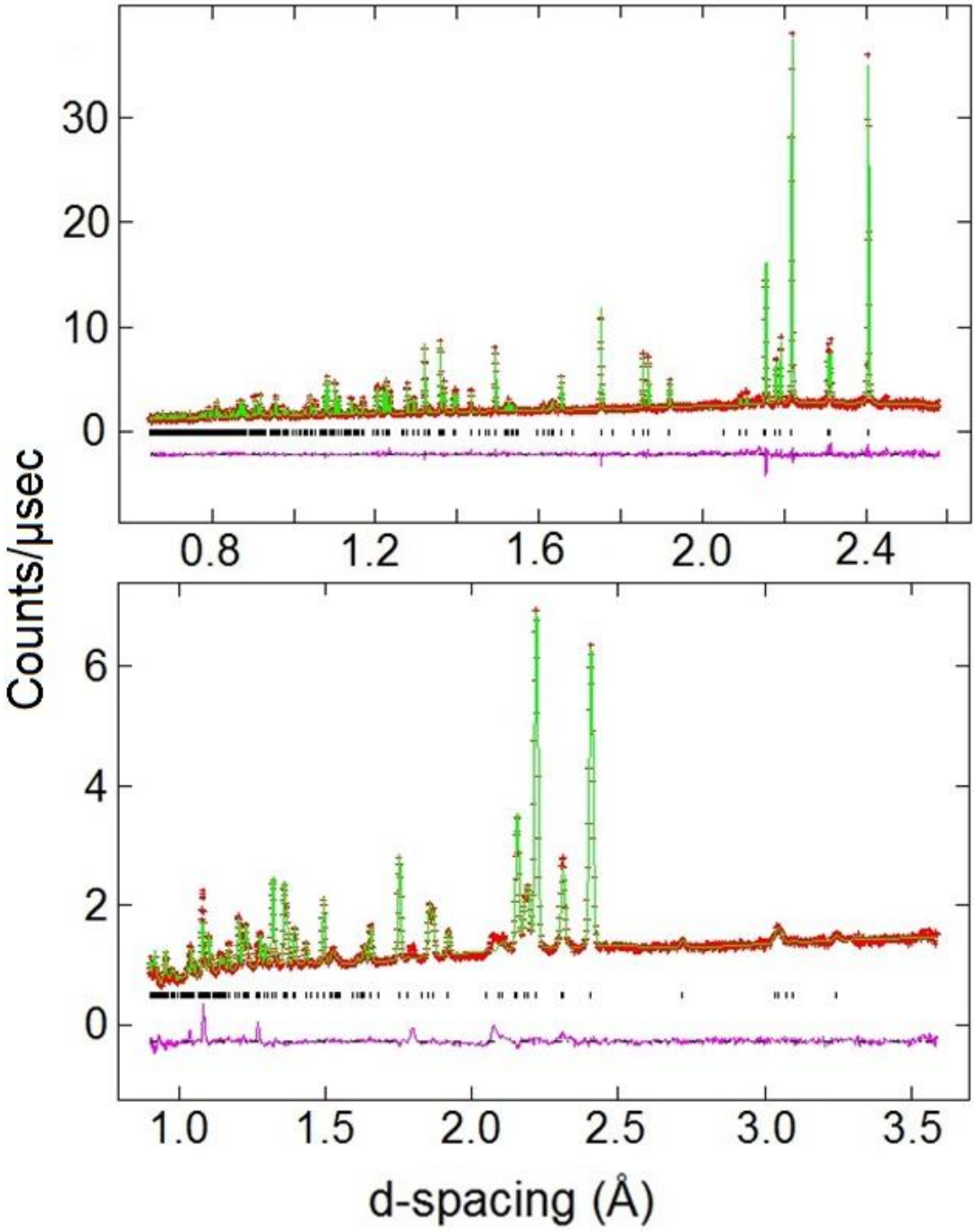


**Figure 5.5.** Fitted time-of-flight neutron diffraction profiles for monoclinic $CoV_2O_6$ at 300 K. The upper and lower plots are respectively from the backscattering ($2\theta$ = 168°) and 90° detector banks of instrument HRPD.

**Table 5.1.** Selected interatomic distances (Å) and bond angles for monoclinic $CoV_2O_6$ from refinements at 4 and 300 K. Mean distances are shown as <M-O>.

| | 4 K | 300 K |
|---|---|---|
| Co-O(1) × 4 | 2.198(2) | 2.206(2) |
| Co-O(2) × 2 | 1.969(2) | 1.964(2) |
| <Co-O> | 2.084(2) | 2.085(2) |
| V-O(1) | 1.660(15) | 1.631(16) |
| V-O(2) | 1.665(16) | 1.671(17) |
| V-O(2) | 2.578(15) | 2.661(15 |
| V-O(3) | 2.110(15) | 2.110(17) |
| V-O(3) × 2 | 1.860(5) | 1.867(6) |
| <V-O> | 1.956(12) | 1.968(13) |

**Table 5.2.** Bond angles (in degrees) for monoclinic $CoV_2O_6$ from refinements at 4 and 300 K.

| Angle | 4 K | 300 K |
|---|---|---|
| O(1)-Co-O(1) × 2 | 74.35(7) | 74.85(8) |
| O(1)-Co-O(1) × 2 | 105.65(7) | 105.15(8) |
| O(1)-Co-O(1) | 180 | 180 |
| O(1)-Co-O(1) | 180 | 180 |
| O(1)-Co-O(2) × 4 | 89.90(4) | 89.65(5) |
| O(1)-Co-O(2) × 4 | 90.10(4) | 90.35(5) |
| O(2)-Co-O(2) | 180 | 180 |
| O(1)-V-O(2) | 107.3(8) | 107.9(9) |
| O(1)-V-O(2) | 174.9(9) | 174.9(10) |
| O(1)-V-O(3) | 98.3(7) | 99.1(8) |
| O(1)-V-O(3) × 2 | 101.6(5) | 102.6(5) |
| O(2)-V-O(2) | 77.8(6) | 77.2(6) |
| O(2)-V-O(3) | 154.4(9) | 153.0(9) |
| O(2)-V-O(3) × 2 | 101.4(5) | 100.9(5) |
| O(2)-V-O(3) | 76.6(5) | 75.9(5) |
| O(2)-V-O(3) × 2 | 77.0(4) | 76.1(5) |
| O(3)-V-O(3) × 2 | 72.7(5) | 72.6(5) |
| O(3)-V-O(3) | 140.6(9) | 139.5(9) |
| Co-O(1)-Co | 105.65(7) | 105.15(8) |
| Co-O(1)-V × 2 | 122.13(19) | 122.75(21 |
| Co-O(2)-V | 134.2(5) | 134.4(5) |
| Co-O(2)-V | 123.6(4) | 122.8(4) |
| V-O(2)-V | 102.2(6) | 102.8(6) |
| V-O(3)-V × 2 | 107.3(5) | 107.4(5) |

**Table 5.3.** Refined lattice parameters, atomic coordinates and thermal displacement parameters from refinement of the $CoV_2O_6$ structure in monoclinic space group *C2/m* at 4 K (lower values) and 300 K (upper values). Fitting residuals, $R_{wp}$, and $\chi^2$, were 0.044 and 3.60 at 4 K and 0.044 and 3.53 at 300 K.

| a (Å) | b (Å) | c (Å) | β (°) | Volume (Å$^3$) |
|---|---|---|---|---|
| 9.2531(2) | 3.5040(1) | 6.6201(1) | 111.617(1) | 199.545(5) |
| 9.2291(1) | 3.5027(1) | 6.5972(1) | 112.084(0) | 197.616(5) |
| Atom | x | y | z | $U_{iso}$ (Å$^2$) |
| Co | 0 | 0 | 0 | 0.0090(10) |
| | | | | 0.0069(8) |
| V | 03055(19) | 0.5 | 0.3388(26) | 0.0090(10) |
| | 0.3090(18) | | 0.3430(24) | 0.0069(8) |
| O(1) | 0.1536(2) | 0.5 | 0.1131(3) | 0.0110(6) |
| | 0.1536(2) | | 0.1105(3) | 0.0070(4) |
| O(2) | 0.4640(2) | 0.5 | 0.2744(4) | 0.0110(6) |
| | 0.4667(2) | | 0.2779(3) | 0.0070(4) |
| O(3) | 0.1916(2) | 0.5 | 0.5622(4) | 0.0110(6) |
| | 0.1912(2) | | 0.5620(3) | 0.0070(4) |

No structural phase transitions were observed in monoclinic $CoV_2O_6$ between 4 and 300 K, but a magnetostriction has been discovered below the $T_N$ = 15 K magnetic ordering temperature. The anomaly is observed in all of the lattice parameters as shown in Figure 5.6. The main changes are an anomalous increase in the *b*-axis length, parallel to the chains of edge-sharing $CoO_6$ octahedra, and decreases in *c*, the monoclinic angle (plotted as –β) and the cell volume as $CoV_2O_6$ is cooled below 15 K ($T_N$). This provides evidence for a strong coupling of the spin order to the lattice.

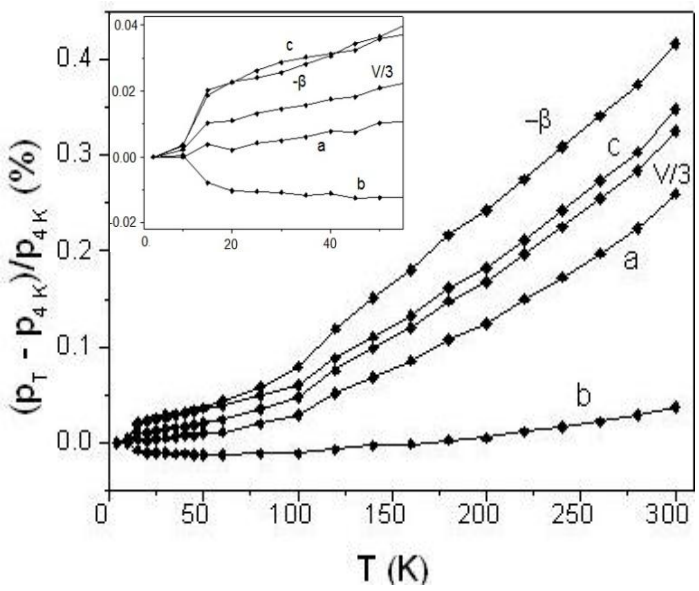


**Figure 5.6.** Plot of lattice parameter changes against temperature for monoclinic $CoV_2O_6$. $\Delta p/p = (p_T - p_{4K})/ p_{4K}$ changes are shown for crystallographic parameters p = a, b, c, -β and V/3 (the latter is used for ease of comparison against the cell lengths). Changes are relative to the 4 K values shown in Table 5.1. Inset expansion shows the changes below 50 K.

Magnetic diffraction peaks appear in neutron diffraction patterns below 15 K as shown in Figure 5.7. These are indexed by the (0 0 ½) propagation vector and no additional incommensurate peaks were observed. A good fit to the magnetic intensities (Figure 5.8) was obtained using a collinear antiferromagnetic model in magnetic group C'2'/m' applied to the a x b x 2c magnetic supercell. $Co^{2+}$ moments lie in the *ac*-plane. The refined *a, c* and resultant moment values are $\mu_a$ = 2.20(8), $\mu_c$ = 4.24(6) and $\mu$ = 4.77(4) $\mu_B$ at 4 K; and $\mu_a$ = 2.12(10), $\mu_c$ = 3.97(10) and $\mu$ = 4.50(5) $\mu_B$ at 10 K. The resultant values are in good agreement with the saturation moment of 4.5 $\mu_B$ reported from high field magnetization measurements at 5 K [14]. The orbital contribution to the $Co^{2+}$ moment in monoclinic $CoV_2O_6$ is unusually large although other examples of ordered moments in excess of the spin-only value of 3 $\mu_B$ are reported, e.g., 3.5 $\mu_B$ in $BiCoOPO_4$ [18] and 3.4 and 3.8 $\mu_B$ in $Co_2(OH)PO_4$ [19].

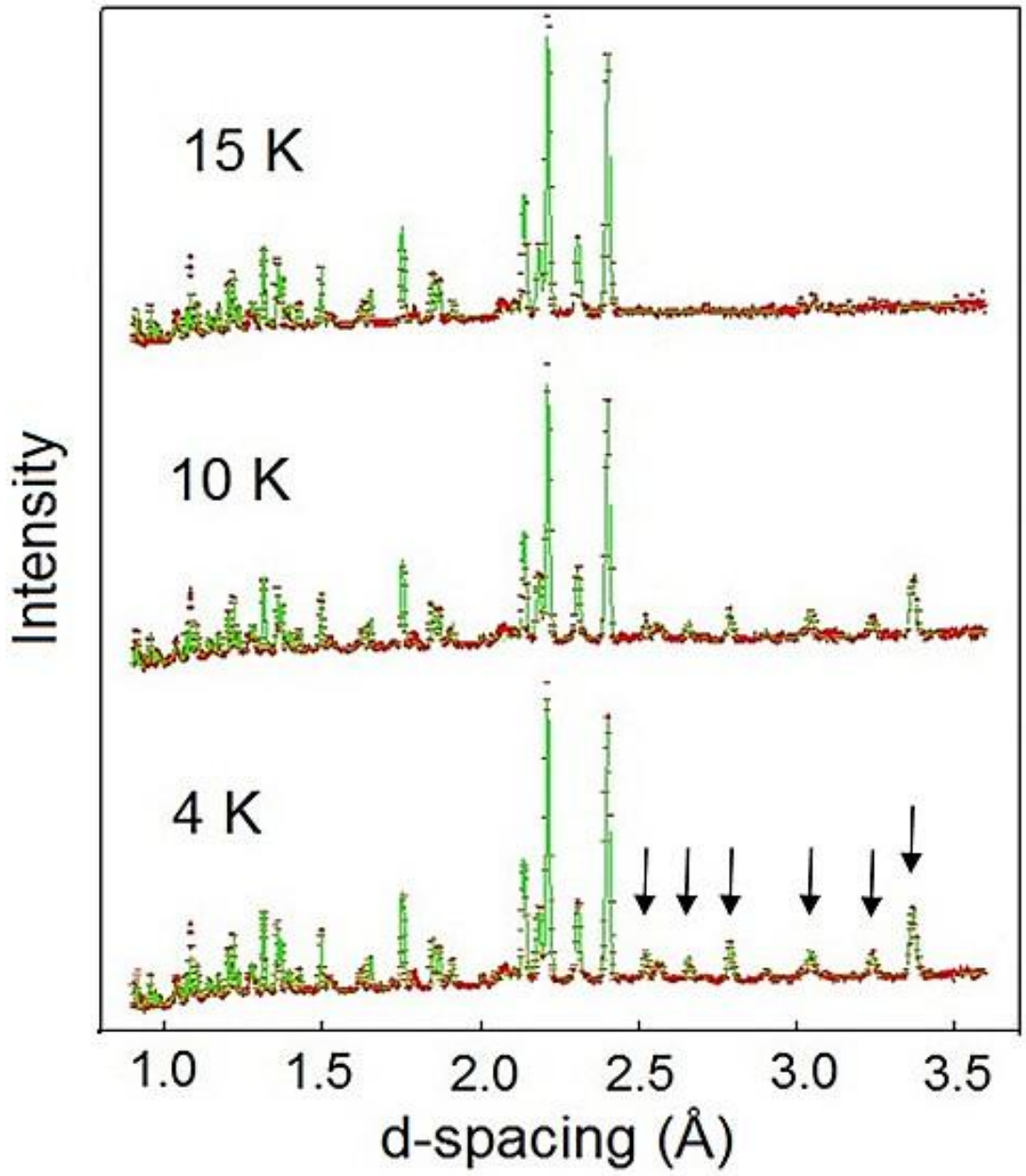


**Figure 5.7.** Time-of-flight powder neutron diffraction profiles from the HRPD backscattering detector for monoclinic $CoV_2O_6$ at 4, 10 and 15 K revealing magnetic peaks (arrowed) at the two lowest temperatures. Rietveld fits of the crystal and magnetic structure models are shown.

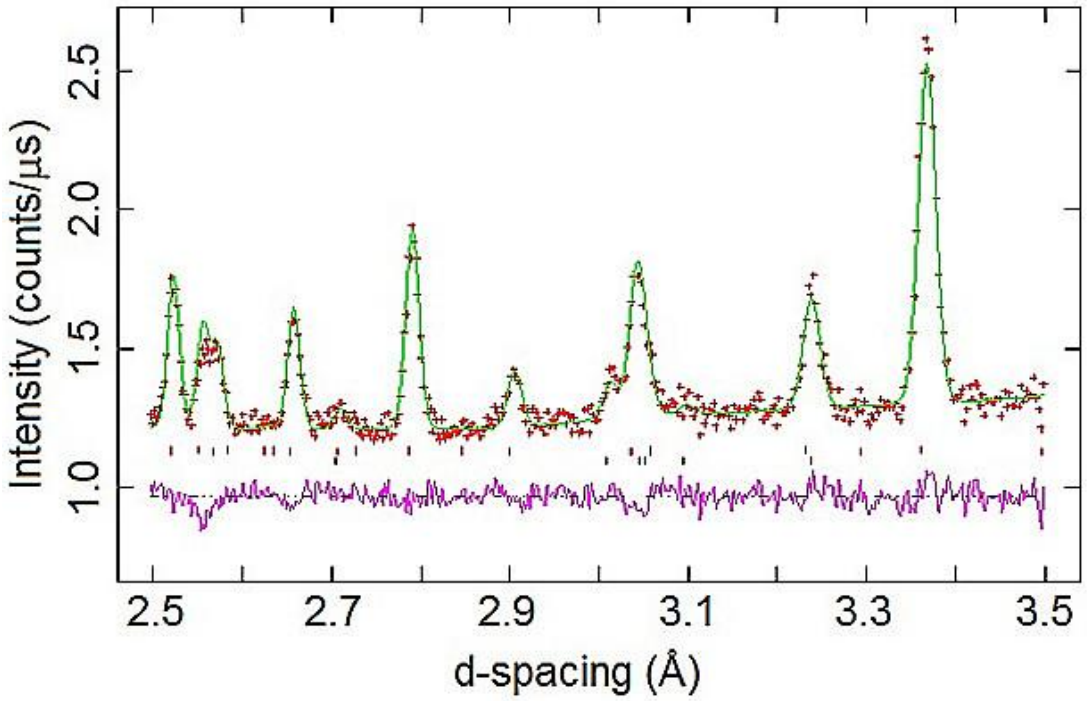


**Figure 5.8.** Expansion of the time-of-flight powder neutron diffraction profile from the HRPD backscattering detector for monoclinic $CoV_2O_6$ at 4 K showing crystal/magnetic structure reflection markers as lower/upper tickmarks, and the difference between observed and calculated profiles below.

The crystal and magnetic structures of monoclinic $CoV_2O_6$ are shown in Figure 5.9. Moments are approximately perpendicular to *a* in the *ac*-plane and are ferromagnetically coupled within the chains of edge-sharing $CoO_6$ octahedra parallel to *b*. Each ferromagnetic chain is coupled antiferromagnetically to four neighbours and ferromagnetically to two in the quasi-triangular *ac*-plane packing of the brannerite structure.

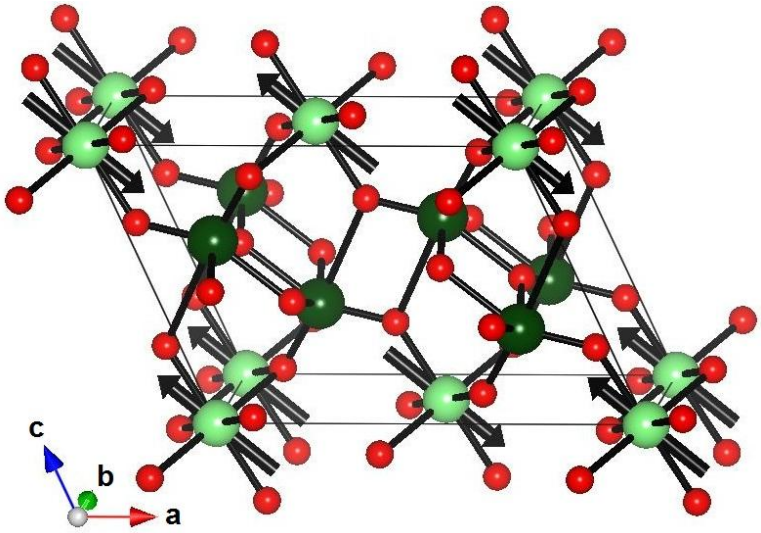


**Figure 5.9**. The crystal and magnetic structures of monoclinic $CoV_2O_6$ shown for the nuclear *C2/m* cell with arrows indicating the ordered magnetic moment directions at the $Co^{2+}$ ions.

**b) Zero- and in-field measurements at instrument WISH**

The changes in magnetic neutron diffraction intensities of $CoV_2O_6$ at 2 K with applied magnetic field are shown in Figure 5.10. In zero field, all of the magnetic *hkl* Bragg peaks have half-integer values of *l* when indexed on the nuclear cell of the crystal structure which has space group symmetry *C2/m*. This condition is equivalent to applying propagation vector (0 1 ½) (or (1 0 ½)) to the C-centred monoclinic cell, or (0 0 ½) to a primitive cell with the same lattice parameters. A small degree of field texturing was evident by comparing the initial and final zero field data sets (Figure 5.10).

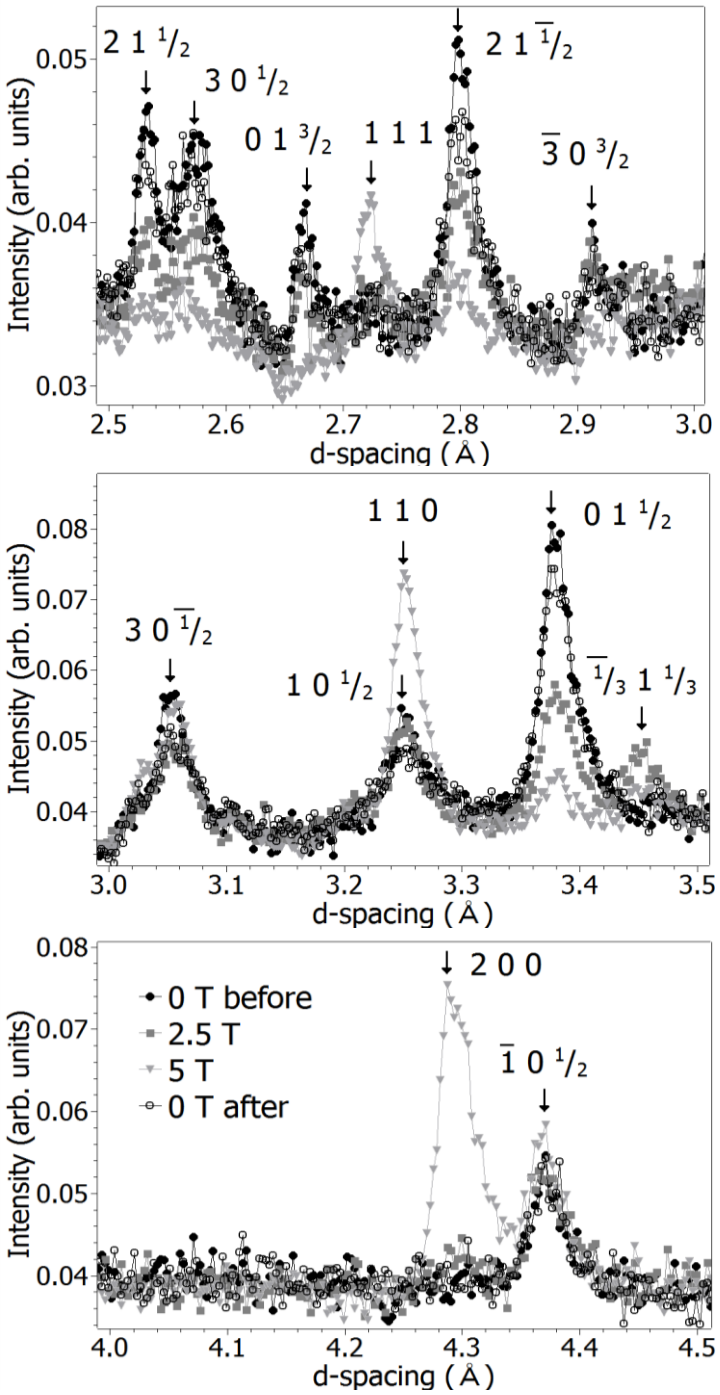


**Figure 5.10.** Magnetic neutron powder diffraction peaks from monoclinic $CoV_2O_6$ at 2 K for the 0 T → 2.5 T → 5.0 T → 0 T sequence of applied magnetic fields. Magnetic peaks are labelled with *hkl* indices relative to the nuclear cell; peaks with half-integral/third-integral/integral values of *l* originate from the antiferromagnetic/⅓-magnetization/ferromagnetic magnetic phases shown respectively in Figures 5.11.(a) -5.11.(c).

The spin structure at zero field, shown in Figure 5.11.(a) and explained in the previous section 5.3.2.a), is antiferromagnetic with equal numbers of spin-up and spin-down ferromagnetic chains.

A ⅓-magnetisation plateau between 1.9 and 3.2 T was previously reported for monoclinic $CoV_2O_6$ [10,11]. When a field of 2.5 T is applied, the neutron intensities due to the antiferromagnetic ground state are suppressed, and a prominent new peak indexed as $\bar{1}/3$ 1 1/3 on the C2/m cell appears (Figure 5.9). Although the ($^{-1}/_3$ 1 1/3) propagation vector suggests that the magnetic cell is nine times larger than the nuclear C2/m cell, a smaller cell with vectors $a = a_n + c_n$, $b = b_n$, and $c = 3c_n$ can be used, where $a_n$, $b_n$, $c_n$ are the nuclear cell vectors. This has three times the volume of the nuclear cell, and corresponds to a quasi-orthorhombic triple superstructure of the quasi-hexagonal brannerite subcell. There are two spin-up ferromagnetic chains for every one spin-down chain, giving the exact resultant ⅓-magnetisation. The majority-spin chains have three parallel and three antiparallel neighbours in the quasi-hexagonal packing, while the minority-spin chains have six antiparallel neighbours (Figure 5.11.(b)).

In an applied field of 5 T, above the upper limit for the ⅓-magnetisation plateau, the magnetic peaks from both the antiferromagnetic and the ferrimagnetic superstructures are suppressed, and additional intensities at positions of nuclear reflections such as 110, 111, and 200 are observed. These correspond to a simple ferromagnetic order of spin chains with propagation vector (0 0 0), as shown in Figure 5.11.(c).

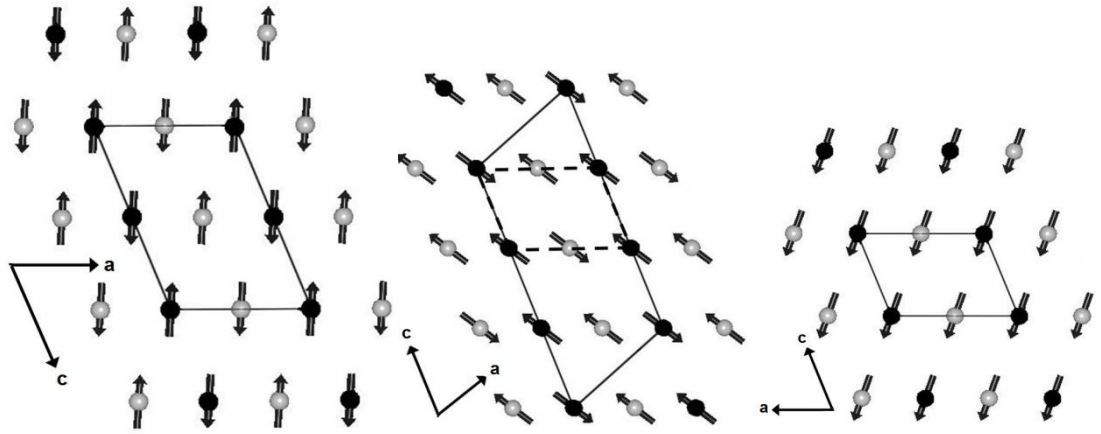


(a) (b) (c)

**Figure 5.11**. Fitted models for (a) the zero field antiferromagnetic, (b) the ferromagnetic ⅓-magnetization, and (c) the fully saturated ferromagnetic phases of $CoV_2O_6$ at 2 K. $Co^{2+}$ spins are parallel to the (010) plane in all phases. Majority up spins point towards the bottom right corner in (b). Magnetic unit cells and axes are shown, and the structural cell is also indicated by broken lines on (b) for comparison. The $Co^{2+}$ spin chains are perpendicular to the (010) plane and Co atoms at heights $y$ = 0 or ½ are shown with dark or light fill.

The crystal structure of monoclinic $CoV_2O_6$ and the above spin structures were fitted to the neutron diffraction data at the different field strengths (Figures 5.12 and 5.13). Lattice parameters and atomic positions for the magnetic phases were constrained to those of the nuclear phase.

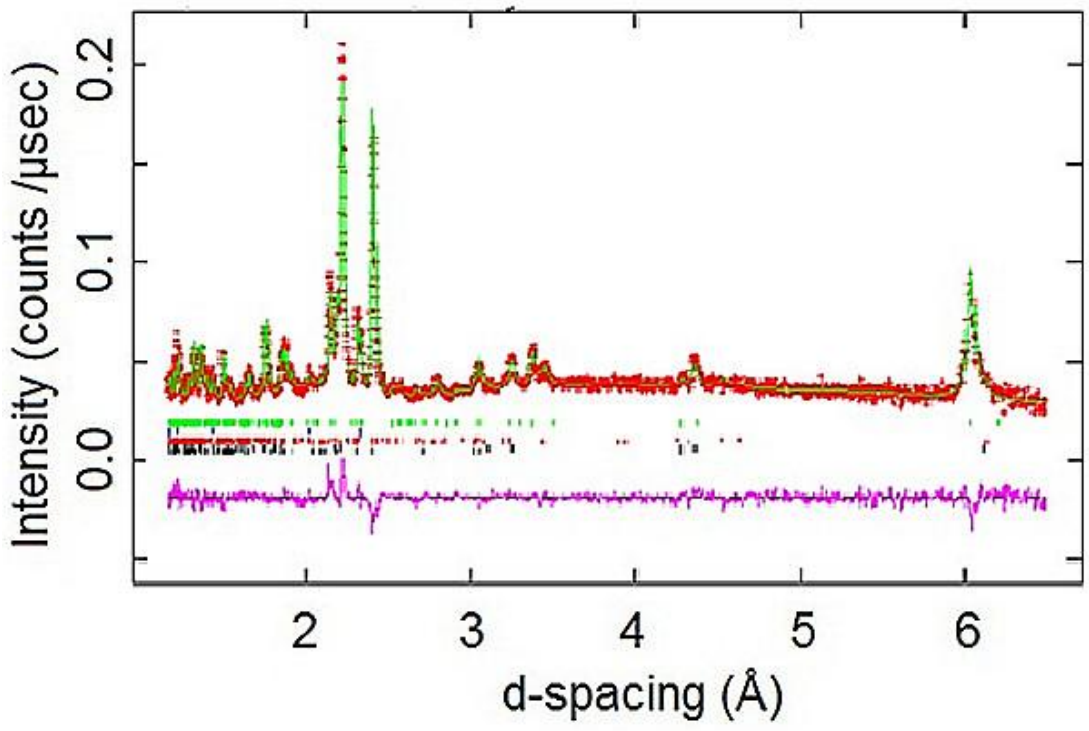


**Figure 5.12.** Fit to the neutron profile from the 90° detector bank of diffractometer WISH for CoV2O6 at 2 K and 2.5 T. Bragg reflection markers correspond to the nuclear phase, the 1⁄3-magnetization ferrimagnetic spin structure, aluminum (from the collimator), and the antiferromagnetic phase, respectively, from bottom to top. The overall fitting residuals were reduced-$\chi^2$ = 3.70, weighted-profile residual $R_{wp}$ = 0.056 and profile residual $R_p$ = 0.039.

Co-existing magnetic phases were observed (antiferromagnetic and ⅓ magnetisation phases at 2.5 T; all three spin ordered phases at 5 T) and fitted to the high field data. This reflects the use of an unaligned powder of magnetically anisotropic $CoV_2O_6$.

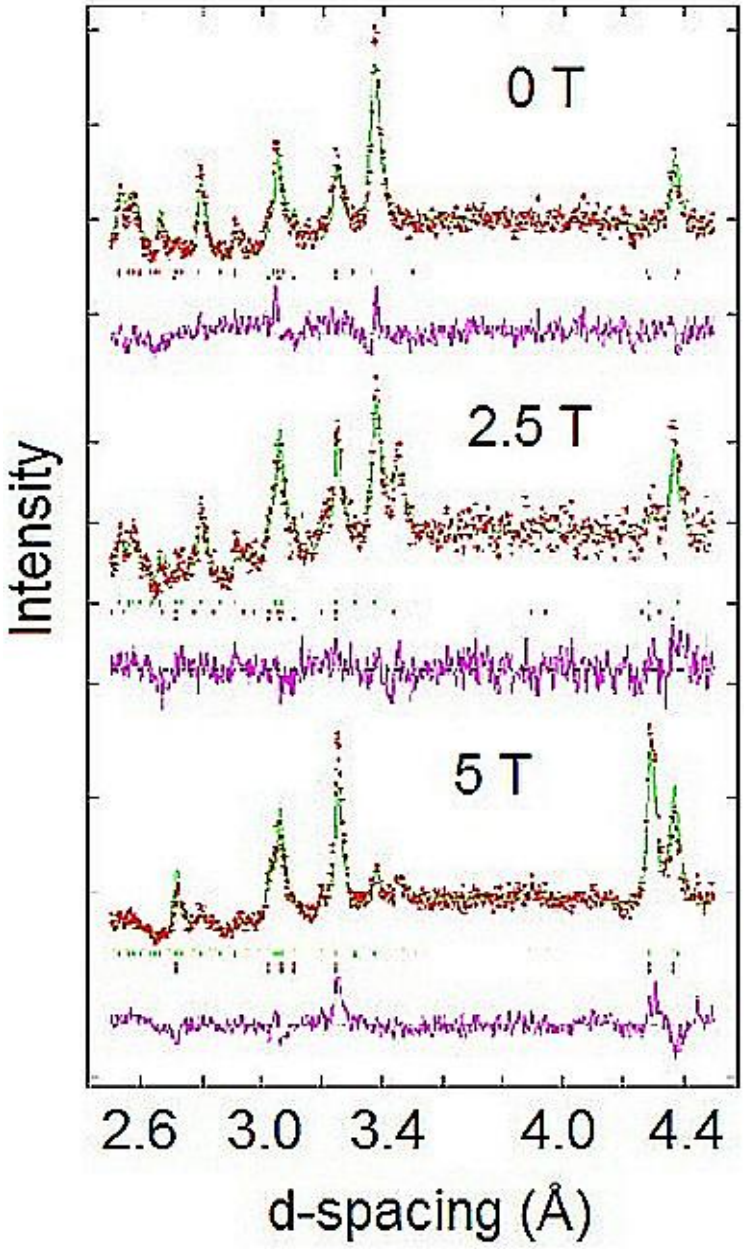


**Figure 5.13.** Fits to the prominent magnetic peaks in the range of Figure 5.6 from the 90° detector bank of diffractometer WISH for $CoV_2O_6$ at 2 K for applied fields of 0, 2.5 and 5.0 T. Discrepancies due to field texturing of the sample are evident in the 5.0-T fit.

The refinements of the three magnetic phases showed that the $Co^{2+}$ magnetic moments always have collinear order in the *ac*-plane, close to the *c*-direction which was reported as the easy axis from single crystal magnetization studies [10]. No spin components parallel to *b* were observed. Variations between moment directions in

the three refined structures (Figure 5.11) probably reflect refinement errors due to slight field-texturing of the sample (Figures 5.10 and 5.13). Single crystal neutron data would be needed to confirm accurate moment directions. The magnitudes of the ordered moments from the 0, 2.5 and 5.0 T data fits were 4.4(1), 4.4(1) and 5.0(2) $\mu_B$ respectively. These are consistent with the 4.8 $\mu_B$ value from the measurement at HRPD for the same sample at zero field. The ordered $Co^{2+}$ moments in monoclinic $CoV_2O_6$ significantly exceed the ideal spin-only value of 3 $\mu_B$, providing evidence for a strong orbital contribution.

The changes in 2 K lattice parameters (Table 5.3) provides evidence for a magnetostriction in $CoV_2O_6$ as the spin orders evolve. Figure 5.14 shows the percentage changes in cell parameters and volume. The overall volume increase as magnetic field increases from 0 to 5 T is mainly driven by an expansion of the ferromagnetic spin chains parallel to *b*, with smaller changes in the *ac*-plane. These displacements probably reflect small changes in the geometries of the Co-O-Co and Co-O-V-O-Co pathways that mediate the superexchange interactions. However, the refined atomic coordinates did not show any field variation, or differ significantly from those measured at HRPD at 4 K.

**Table 5.3.** Refined lattice parameters and volume for the *C2/m* unit cell of monoclinic $CoV_2O_6$ at 2 K as a function of magnetic field strength.

| $H$ (T) | 0 | 2.5 | 5.0 |
|---|---|---|---|
| $a$ (Å) | 9.2442(5) | 9.2368(5) | 9.2391(5) |
| $b$ (Å) | 3.5000(1) | 3.5044(1) | 3.5044(1) |
| $c$ (Å) | 6.5997(3) | 6.6036(3) | 6.6055(3) |
| $\beta$ (°) | 112.092(5) | 112.039(4) | 112.030(4) |
| $V$ (Å$^3$) | 197.85(2) | 198.13(2) | 198.26(2) |

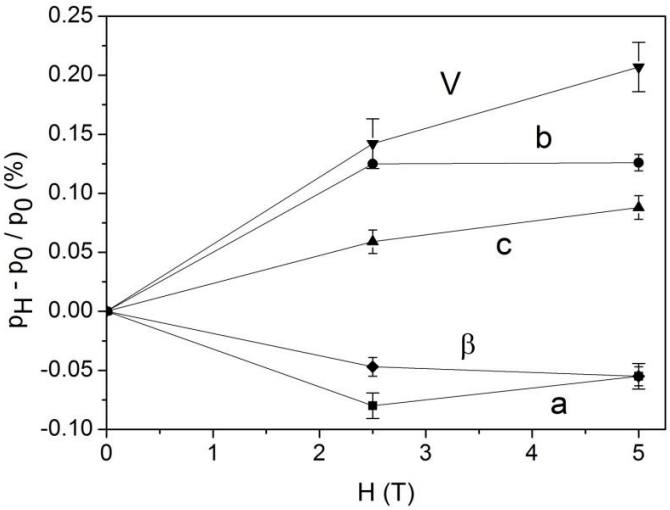


**Figure 5.14.** Field-induced changes in the lattice parameters ($p \equiv a$, $b$, $c$, β or $V$; subscripts refer to applied magnetic field) of $CoV_2O_6$ at 2 K.

## 5.4. Discussion

These neutron diffraction studies confirm that monoclinic $CoV_2O_6$ adopts the *C2/m* brannerite structure, with no significant cation disorder between Co and V sites in a sample quenched from 725 °C. No structural phase transitions are observed between 4 and 300 K, but the structure shows a magnetostrictive anomaly at the $T_N$ = 15 K magnetic transition. This is most likely due to spin–orbit effects at the high spin $Co^{2+}$ ions which couple the spin-order to the lattice. The large orbital contributions to the high temperature paramagnetic and low temperature ordered moments support this conclusion. The magnetostriction expands the lattice in the direction of the ferromagnetically ordered $Co^{2+}$ chains on cooling, but decreases the interchain distances slightly resulting in an overall volume contraction. A strong spin-orbit coupling is also evidenced by the substantial tetragonal compression of the $CoO_6$ octahedra which have four long (2.21 Å) and two short (1.96 Å) Co-O bonds (Table 5.2). A Jahn-Teller distortion, quenching the orbital moment, would require tetragonal elongation resulting in four short and two long bonds. The $VO_6$ octahedra are highly distorted, having two short (1.63 and 1.67 Å) V-O bonds in a cis-configuration with long (2.11 Å) and very long (2.66 Å) bonds opposite. This is

equivalent to an off-centre displacement of V in the ac-plane, relative to the centre of the $VO_6$ octahedron. These $V^{5+}$ $d^0$-cation displacements are antiferroelectrically ordered in the non-polar *C2/m* $CoV_2O_6$ structure.

The zero-field magnetic structure of monoclinic $CoV_2O_6$ is antiferromagnetic as there are equal numbers of spin-up and spin-down chains parallel to *b*. Each chain is connected through Co-O-V-O-Co pathways to six neighboring chains, with antiferromagnetic couplings to four chains (at $\pm\boldsymbol{a}/2$ and $\pm\boldsymbol{c}$) and ferromagnetic coupling to the other two (at $\pm(\boldsymbol{a}/2 + \boldsymbol{c})$). The isostructural $MnV_2O_6$ [14] has the same (0 0 ½) order of spins although in that material the spins are parallel to *b* whereas they are perpendicular to *b* in $CoV_2O_6$. The same *ab*-plane spin order was reported for triclinic $CuV_2O_6$, but the interchain alignment in the *c*-direction was unclear [17]. The observed magnetic structure of monoclinic $CoV_2O_6$ confirms that the intrachain interactions are ferromagnetic, in keeping with the positive value of Weiss temperature, and with previous results for triclinic $CoV_2O_6$ although here the incommensurate long-range spin-ordered structure has not yet been determined [1].

Ferromagnetic $Co^{2+}$ chains with moments confined to the *ac*-plane are present also in the phases of monoclinic $CoV_2O_6$ obtained in the applied fields of 2.5 and 5 T. Strong spin-orbit (and hence spin-lattice) coupling is evidenced by the large values of the ordered moment, and magnetostrictions as spin order varies with field or temperature. Although the brannerite structure is not derived from a hexagonal lattice type, and Co atoms are present at two different positions in the chain direction (indicated by dark or light fill on Figure 5.11), the observed interchain spin orders in the *ac*-plane are typical for a quasi-triangular antiferromagnetic lattice. The triangles of interchain couplings are parallel to [100], [001] and [101] directions, using the lattice vectors of the antiferromagnetic phase in Figure 5.11(a) throughout for convenience. In the antiferromagnetic zero field phase, spin chains are antiparallel to neighbours in the [100] and [001] directions, but parallel along [101]. The ferrimagnetic ⅓-magnetisation phase has antiparallel couplings in the [100] direction but ‘up-up-down’ repeat sequences in the [001] and [101] directions. These orders are consistent with antiferromagnetic interaction magnitudes $J_{100} > J_{001} > J_{101}$ on the triangular lattice, with frustration of the weakest $J_{101}$ interactions in the zero field phase.

A recent simulation of the phase diagram for geometrically frustrated triangular antiferromagnets [25] has shown that other collinear intermediate-magnetization phases may be realized in addition to the 1/3-magnetization order, and several of these have been observed in the delafossite $CuFeO_2$ [26]. Reported magnetization measurements [11] for monoclinic $CoV_2O_6$ at low temperatures (below 5 K) showed, in addition to the 1/3-magnetization plateau, steps at 1/5 and 2/5 of saturation that may correspond to additional phases with more complex orders of spin-up and -down chains. A collinear 1/5-magnetization state with a large stability domain is shown in the computed phase diagram [25], although a 2/5 state is not featured. Hence, it appears likely that new field-induced states of the frustrated triangular antiferromagnetic lattice may be accessible in monoclinic $CoV_2O_6$.

## 5.5. Conclusions

Antiferromagnetic order has been observed below $T_N$ = 15 K in monoclinic brannerite type $CoV_2O_6$. No structural transition is observed down to 4 K, but a magnetostriction accompanying antiferromagnetic order is discovered. The 1/3-magnetization phase in monoclinic $CoV_2O_6$ arises from the accidental near equivalence of antiferromagnetic interchain exchange interactions that lead to spin orders typical of a frustrated two-dimensional triangular lattice. $Co^{2+}$ moments have a large orbital component and are collinearly ordered, near parallel to the *c* axis, in the antiferromagnetic, 1/3-magnetization, and fully saturated ferromagnetic phases. Spin-lattice coupling leads to a magnetostriction and volume expansion as field increases. Further ordered phases such as a 1/5-magnetization state may be observable at other field strengths in monoclinic $CoV_2O_6$.

## 5.6. References


1 . S. A. J. Kimber, H. Mutka, T. Chatterji, T. Hofmann, P. F. Henry, H. N. Bordallo, D. N. Argyriou and J. P. Attfield, Phys. Rev. B **84**, 104425 (2011).

2. M. Gondrand, A. Collomb, J.C. Joubert and R.D. Shannon, J. Solid State Chem. **11,** 1-9 (1974).

3. M. Hase, M. Kohno, H. Kitazawa, N. Tsujii, O. Suzuki, K. Ozawa, G. Kido, M. Imai and X. Hu, Phys. Rev. B **73**, 104419 (2006).

4. H. Kikuchi, Y. Fujii, M. Chiba, S. Mitsudo, T. Idehara, T. Tonegawa, K. Okamoto, T. Sakai, T. Kuwai and H. Ohta, Phys. Rev. Lett. **94,** 227201 (2005).

5. N. Bellido, C. Simon and A. Maignan, Phys. Rev. B **77**, 054430 (2008).

6. K. Okamotoa and A. Kitazawa, J. Phys. Chem. Sol. **62** 365-368 (2001).

7. B. Jasper-Tonnies and H. Muller-Buschbaum, Z. Anorg. Allg. Chem. **508**, 7 (1984).

8. K. Mocala and J. Ziolkowski, J. Solid State Chem. **69,** 299 (1987).

9. M. Belaiche, M. Bakhache, M. Drillon, A. Derrory and S. Vilminot, Physica. B **305**, 270 (2001).

10. Z. He, J. Yamaura, Y. Ueda, and W. Cheng, J. Am. Chem. Soc. **131**, 7554 (2009).

11. M. Lenertz, J. Alaria, D. Stoeffler, S. Colis and A. Dinia, J. Phys. Chem. C **115**, 17190 (2011).

12. K. Singh, A. Maignan, D. Pelloquin, O. Perez and Ch. Simon, J. Mater. Chem. **22**, 6436 (2012).

13. X Yao, J. Phys. Chem. A, **116**, 2278 (2012).

14. A. J. Kimber and J. P. Attfield, Phys. Rev. B **75,** 064406 (2007).

15. Z. Chuan-Cang, L. Fa-Min, D. Peng, C. Lu-Gang, Z. Wen-Wu and Z. Huan, Chin. Phys. B **19**, 6 067503 (2010).

16. C. Calvo and D. Manolescu, Acta Cryst. B **29**, 1743 (1973).

17. A.N. Vasilev, L.A. Ponomarenko, E.V. Antipov, Yu.A. Velikodny, A.I. Smirnov, M. Isobe, Y. Ueda, Phys. B **284-288**, 1615-1616 (2000).

18. J. Kikuchi, K. Ishiguchi, K. Motoya, M. Itoh, K. Inari, N. Eguchi and J. Akimitsu, J. Phys. Soc. Jpn. **69,** 2660-2668 (2000).

19. A.V. Prokofieva, R.K. Kremerb, W. Assmus, J. Crystal Growth **231,** 498–505 (2001).
20. E. Baudrin, S. Laruelle, S. Denis, M. Touboul, J. M. Tarascon, Solid State Ionics **123**, 139 (1999).
21. A. Xu, Q. Lin, M. Ji, B. Zhaorigetu, React. Kinet. Catal. Lett. **93**, 273 (2008).
22. http://www.mantidproject.org/Main_Page
23. A.C. Larson and R.B. Von Dreele, Los Alamos National Laboratory Report no. LAUR 86-748 (1994) (unpublished).
24. I.D. Brown, D. Altermatt, Acta Crystallogr. **B41,** 244–247 (1985).
25. R. S. Fishman, Phys. Rev. Lett. **106**, 037206 (2011).
26. S. Kanetsuki, S. Mitsuda, T. Nakajima, D. Anazawa, H. A. Katori, and K. Prokes, J. Phys.: Condens. Matter **19**, 145244 (2007).

# Chapter 6. Magnetic properties and spin orders of columbite type high-pressure $CoV_2O_6$ and $NiV_2O_6$

## 6.1. Introduction

The structure of high-pressure $CoV_2O_6$ and $NiV_2O_6$ (Figure 6.1) is similar to that of columbite [(Fe,Mn)$Nb_2O_6$], a mineral that is an ore of niobium. Compounds in this group crystallise in orthorhombic *Pbcn* space group. $CoV_2O_6$ has triclinic or monoclinic [1,2,3,4,5] and $NiV_2O_6$ triclinic [2,6] brannerite type structures at ambient pressure. The transition from brannerite to columbite structure involves an increase of vanadium coordination from 5 + 1 to 6 [7,8], a change from a cubic close-packed to a hexagonal close-packed oxygen network, a retention of part of the structure of the $VO_6$ sheets, and a collapse of the $MO_6$ (M = Co or Ni) rutile-like chains into α-$PbO_2$ chains. The volume change resulting from the transition is of the order of 8 % [7]. As in the corresponding brannerite structures the $MO_6$ octahedra

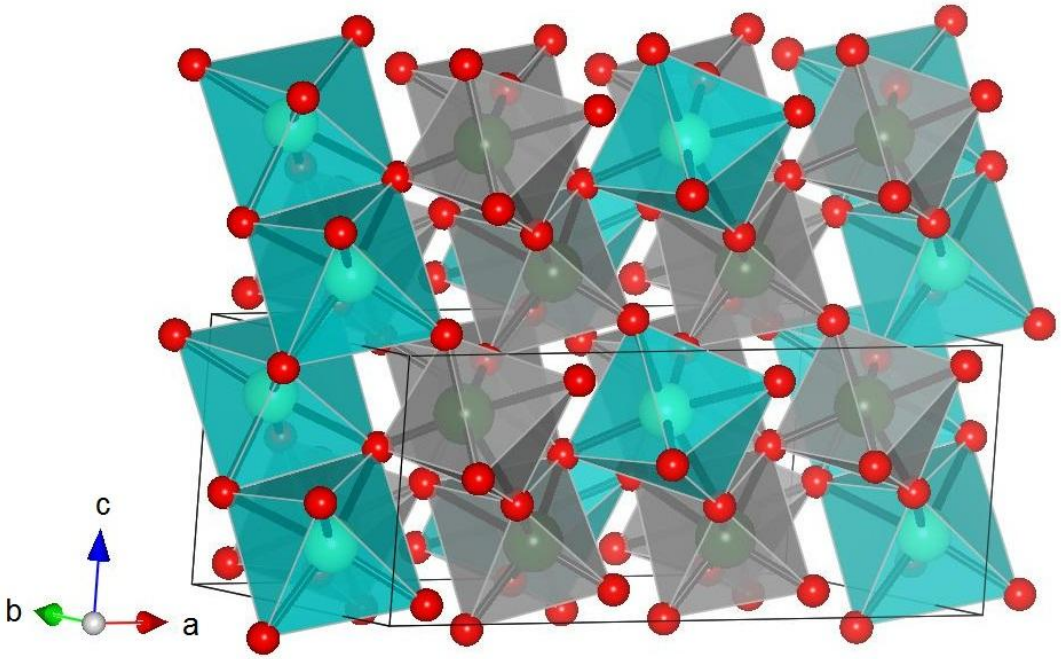


**Figure 6.1**. Columbite structure. Blue octahedra present $MO_6$ (M = Co or Ni) and violet octahedra $VO_6$.

are connected by chains of corner and edge sharing $VO_6$ octahedra but now the chains of $MO_6$ octahedra are along the c-axis in zig-zag formation while in the $CoV_2O_6$ brannerites they are in straight lines along the b-axis and in triclinic $NiV_2O_6$ in straight lines along the c-axis.

Columbite type $CoV_2O_6$ and $NiV_2O_6$ have been synthesised earlier [7,9] but have not been much characterised. The columbite $NiV_2O_6$ was reported to have an antiferromagnetic transition with $T_N$ = 2.5 K, an effective magnetic moment of $\mu_{eff}$ = 3.6(3) $\mu_B$, which is typical for $Ni^{2+}$, and a Weiss temperature of -17(2) K [9]. The M-H plot at 1.8 K showed a metamagnetic transition, from an antiferromagnetic to a ferromagnetic state at ~1.5 Tesla [9].

Besides $CoV_2O_6$ and $NiV_2O_6$, several columbite type $MV_2O_6$ (M = Cu, Zn, Mg, Mn and Cd) phases have been synthesised [7] but they have not been further studied. The triclinic brannerite type materials $CoV_2O_6$ and $NiV_2O_6$ have been reported to be antiferromagnetic with $T_N$ = 6.3 and 16.4 K respectively and to show metamagnetic type transitions [2,5,9]. Both monoclinic and triclinic brannerite type $CoV_2O_6$ phases exhibit a 1/3 magnetisation plateau at low temperatures [3,4,5].

Some $ANb_2O_6$ compounds (A = Mn[10,11], Fe[12,13], Ni[12] or Co[14]) with columbite structure have been synthesised in ambient pressure and their magnetic properties have been reported. $MnNb_2O_6$ has been reported to order antiferrromagnetically below $T_N$ = 4.4 K [10]. Heid *et al.* [12] have reported $FeNb_2O_6$ and $NiNb_2O_6$ to exhibit antiferromagnetic order below 4.9 K and 5.7 K respectively, with a canted magnetic structure. Yaeger *et al.* [13] have observed an antiferromagnetic ordering for $FeNb_2O_6$ at $T_N$ = 5.5 K. For $CoNb_2O_6$ magnetic transitions at 2.9 and 1.95 K have been reported; at 1.4 K a coexistence of two magnetic phases with propagation vectors (0, 0.5, 0) and (0.5, 0.5, 0), was observed [14].

The $AB_2O_6$ compounds are considered to be prototype materials since they exhibit low dimensional magnetic characteristics. Whereas tetragonal $ATa_2O_6$ phases are model two-dimensional magnetic systems, the orthorhombic $ANb_2O_6$ phases exhibit weakly interacting one-dimensional magnetic chains [14]. We report here the magnetic properties and spin orders of columbite type high-pressure $CoV_2O_6$ and

$NiV_2O_6$ compounds. The magnetisation measurements were done working with Dr. Anna Kusmartseva.

## 6.2. Experimental

In both cases the high pressure product was made from an ambient pressure polymorph. The monoclinic $CoV_2O_6$, the synthesis of which is described in the previous chapter, was used as a precursor for the synthesis of columbite $CoV_2O_6$. For the synthesis of columbite $NiV_2O_6$ a triclinic $NiV_2O_6$ precursor was synthesised by grinding stoichiometric quantities of NiO (Aldrich, 99.99%) and $V_2O_5$ (Aldrich, 99.99%) in a mortar and then heating in a furnace in air at 650°C for 21 hours. The precursors were then pressed in the Walker module (see section 2.1.2) at 6 GPa and 900°C for 15 min with quenching. The fits to the data from laboratory powder x-ray diffraction measurements were made using the columbite structure type with *Pbcn* space group (Figures 6.2 and 6.3).

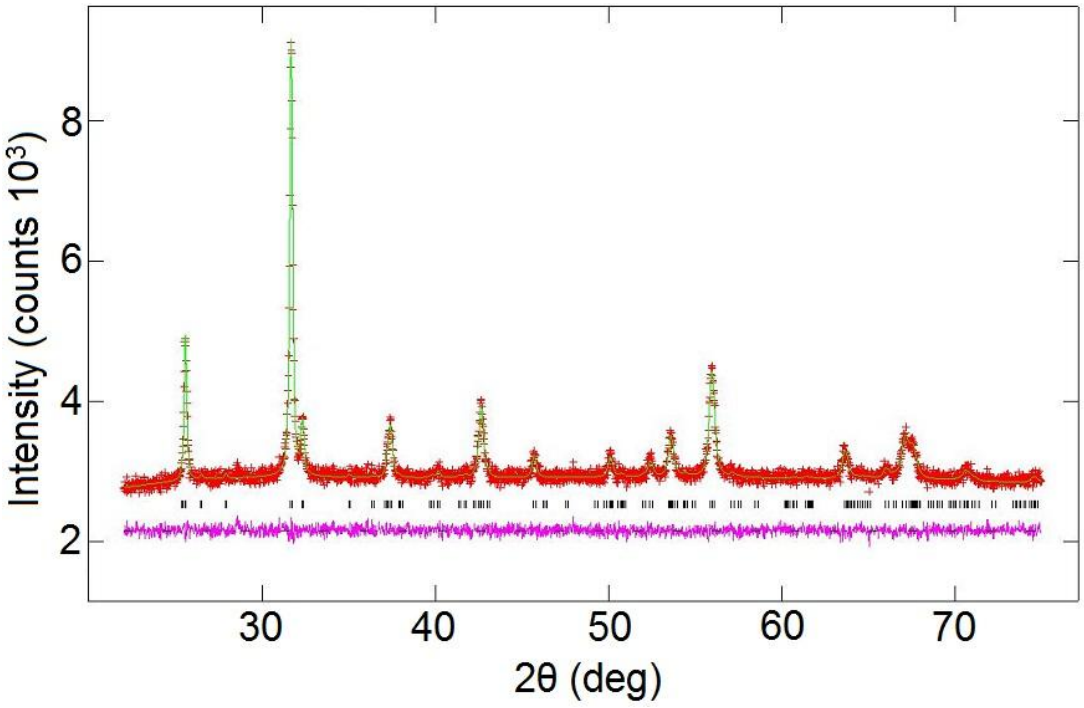


**Figure 6.2.** Laboratory powder x-ray diffraction profile for columbite $CoV_2O_6$

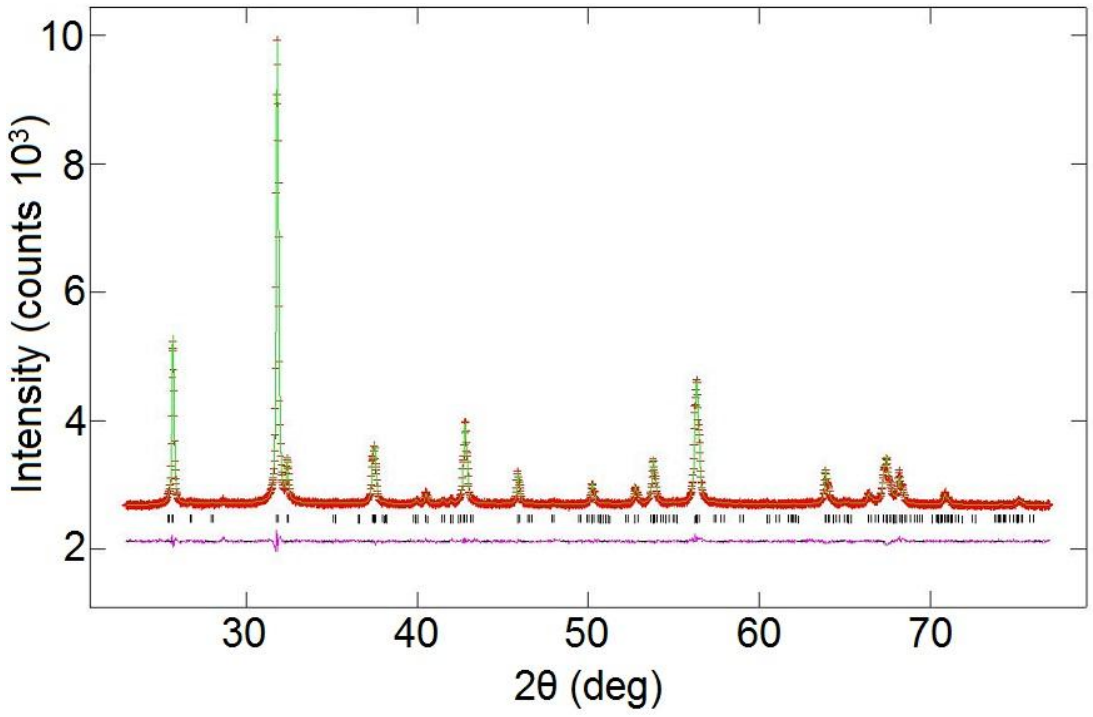


**Figure 6.3.** Laboratory powder x-ray diffraction profile for columbite $NiV_2O_6$

For the neutron powder diffraction measurements several high-pressure products were combined to give 96 mg of $CoV_2O_6$ and 88 mg of $NiV_2O_6$. Neutron diffraction data were collected on two instruments. Measurements without magnetic field were performed on high intensity and resolution time-of-flight neutron diffractometer GEM (see section 2.2.3) at the ISIS spallation source. Data were collected at 1.5 K, 10 K and 295 K for $NiV_2O_6$ and at 1.6 K, 10 K and 300 K for $CoV_2O_6$. Further powder neutron diffraction patterns were collected in magnetic field using the long-wavelength, time-of-flight neutron diffractometer WISH (see section 2.2.3) at ISIS. Data were collected for both samples at 1.7 K. For $CoV_2O_6$ the measurements were carried out at a 0 → 0.1 → 1.0 → 2 T sequence of applied magnetic field strengths and for $NiV_2O_6$ at a 0 → 1 → 2 → 3 → 4 T sequence. For the neutron diffraction measurements in magnetic field, the powder was cold-pressed into pellets which were then placed in a vanadium sample can. The neutron diffraction data were normalised using the MantidPlot program [15], which was also used for creating the figures 6.17 - 6.20, and crystal and magnetic structures were refined using the GSAS software package [16].

Magnetic susceptibility and hysteresis data were recorded using a Quantum Design SQUID magnetometer (see section 2.3).

## 6.3. Results

### 6.3.1. Magnetisation measurements

For the columbite type $CoV_2O_6$ the susceptibility measurements were first performed at 1 T (Figure 6.4) and then again at 500 Oe (Figure 6.5) to see if the small discontinuency at around 3 K on the inverse susceptibility plot that might be a magnetic transition would turn more prominent at a lower field. However the possible transition did not appear any more obvious in a lower field. At 500 Oe, the measurements were done both in zero field cooling and field cooling modes and no significant difference in the curves was observed.

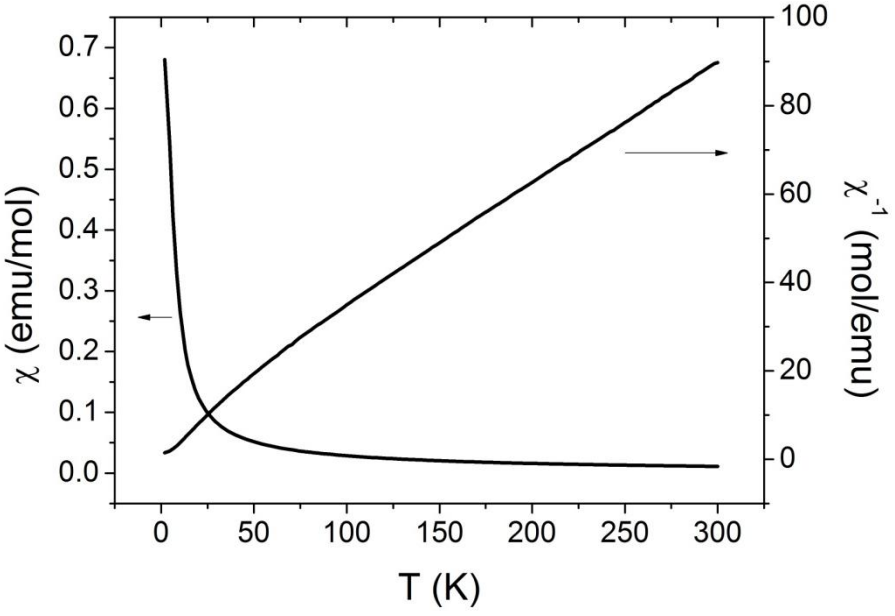


**Figure 6.4.** Plots of magnetic susceptibility and inverse magnetic susceptibility against temperature in 1 Tesla field for the columbite type high-pressure $CoV_2O_6$

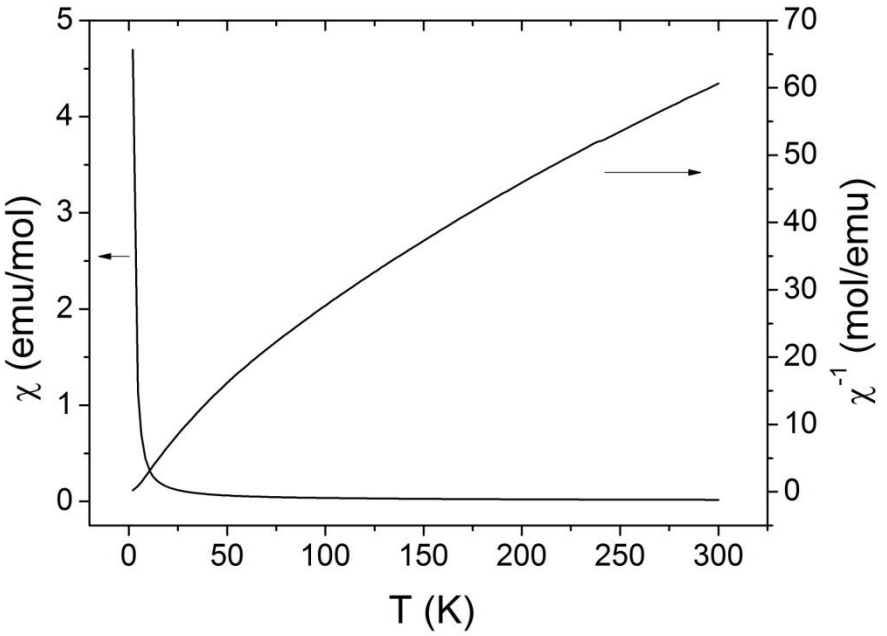


**Figure 6.5.** Plots of magnetic susceptibility and inverse magnetic susceptibility against temperature in 500 Oe field for the columbite type high-pressure $CoV_2O_6$

The linear fit to the inverse susceptibility data at 1 Tesla between 180 and 280 K, $\chi^{-1} = 8.20572 + 0.27221T$, gives an effective moment of 5.43 $\mu_B$, which is considerably larger than the spin-only value for high spin $Co^{2+}$ of 3.87 $\mu_B$, indicating that there is a large orbital contribution to the moment. The same fit gives a Weiss temperature of -30.1 K indicating that the dominant exchange interactions are antiferromagnetic. The M-H hysteresis measurement at 1.8 K (Figure 6.6) shows the existence of a ferromagnetic order but it is difficult to estimate from the susceptibility plots when exactly it takes place. Further hysteresis measurements for the $CoV_2O_6$ were carried out (Figure 6.7) to find out at which temperature the transition appears. The M-H plot at 2, 4, 6, 8, 10, 15, 20 and 25 K showed that the transition starts to develop at temperatures between 15 and 20 K.

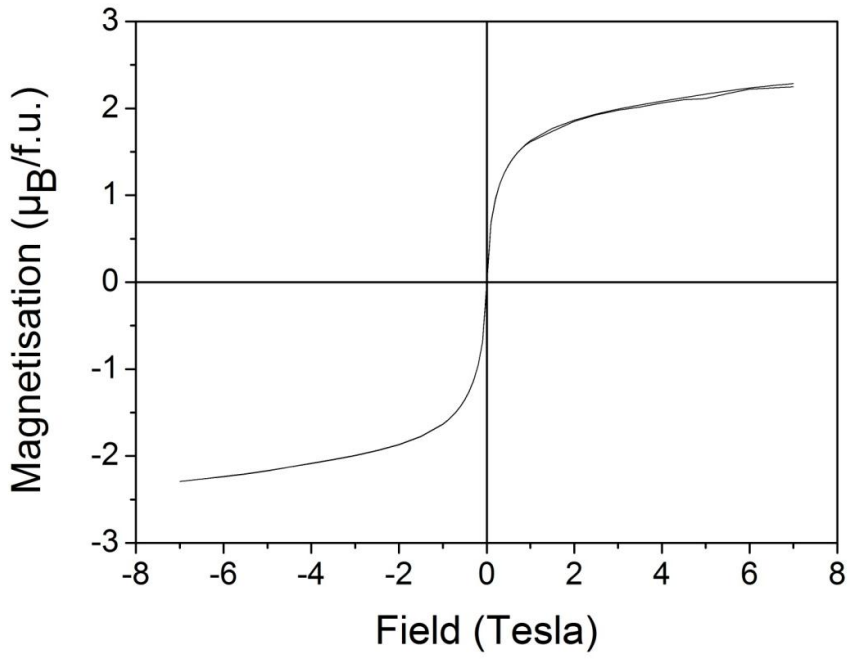


**Figure 6.6.** Hysteresis measured at 1.8 K for the columbite type high-pressure $CoV_2O_6$ showing a magnetic order.

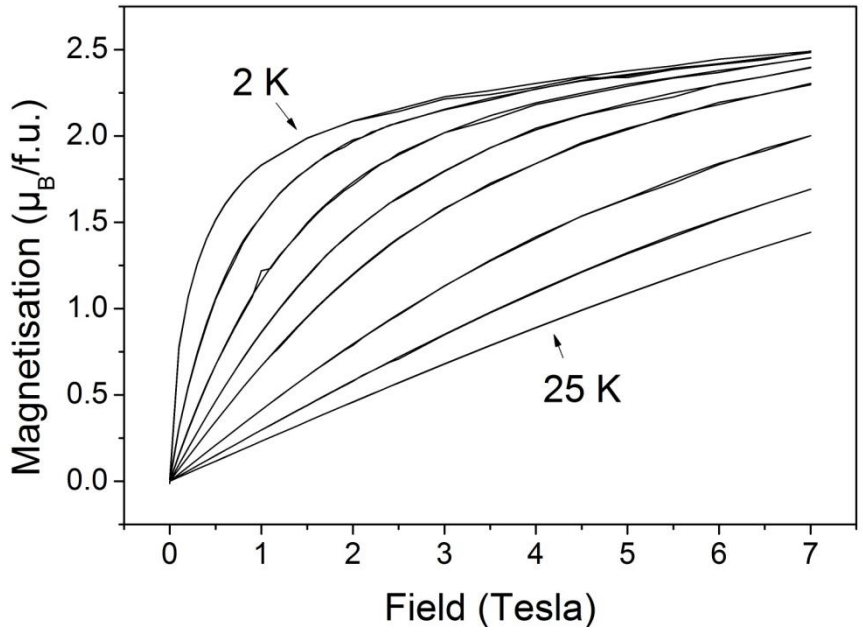


**Figure 6.7.** Hysteresis measured at 2, 4, 6, 8, 10, 15, 20 and 25 K (from top to bottom) for the columbite type high-pressure $CoV_2O_6$ showing the temperature dependence of the ferromagnetic order.

For the $NiV_2O_6$ the plots of magnetic susceptibility and inverse magnetic susceptibility against temperature in 500 Oe field (Figure 6.8) revealed a magnetic transition at 3.2 K. Susceptibility measurements were carried out only up to 20 K as measurements from base temperature up to room temperature had been earlier done by Kimber [9], who reported that a Curie-Weiss fit to the inverse susceptibility in the range 200 < T < 300 K gave an effective magnetic moment of $\mu_{eff}$ = 3.6(3) $\mu_B$, typical for $Ni^{2+}$, and a Weiss temperature of -17(2) K.

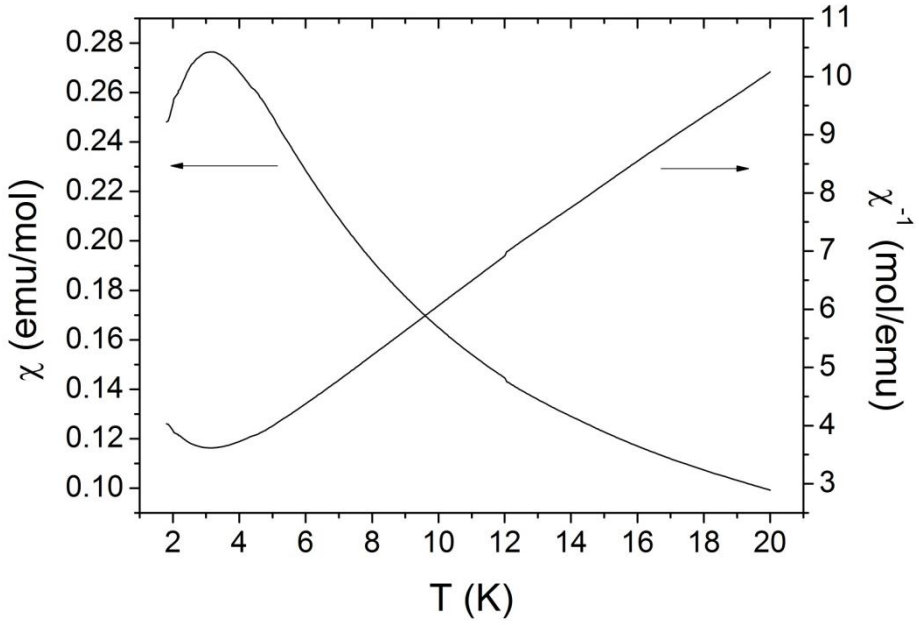


**Figure 6.8.** Plots of magnetic susceptibility and inverse magnetic susceptibility against temperature in 500 Oe field for the columbite type high-pressure $NiV_2O_6$

Further susceptibility measurements were carried out at 0.25, 0.5, 1, 1.5, 2, 2.5 and 3 T between 2 and 10 K (Figure 6.9) to see how the transition behaves at higher magnetic fields. The different behaviour in the plots between 1 and 1.5 Tesla corresponds to the first turn in the metamagnetic M-H hysteresis plot (Figure 6.10) at approximately 1 T field.

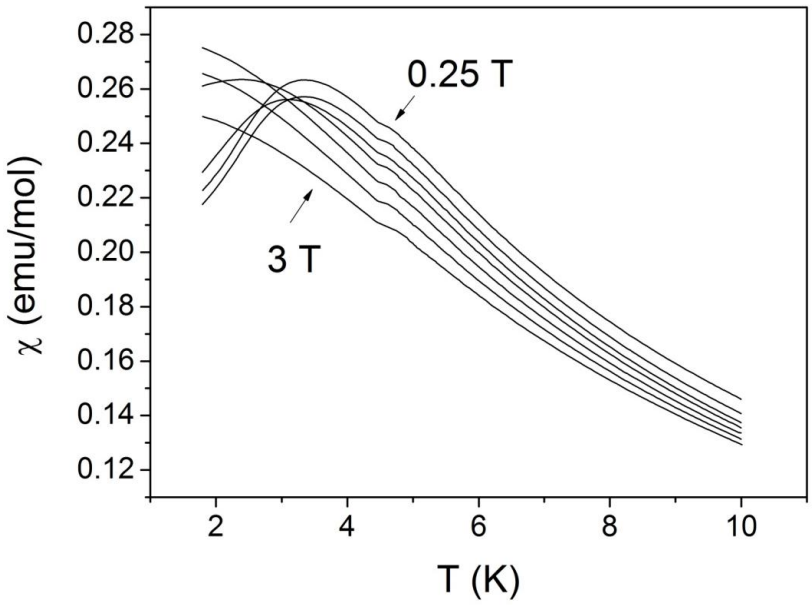


**Figure 6.9.** Plot of magnetic susceptibility at 0.25, 0.5, 1, 1.5, 2, 2.5 and 3 T (from top to bottom) against temperature for the columbite type high-pressure $NiV_2O_6$.

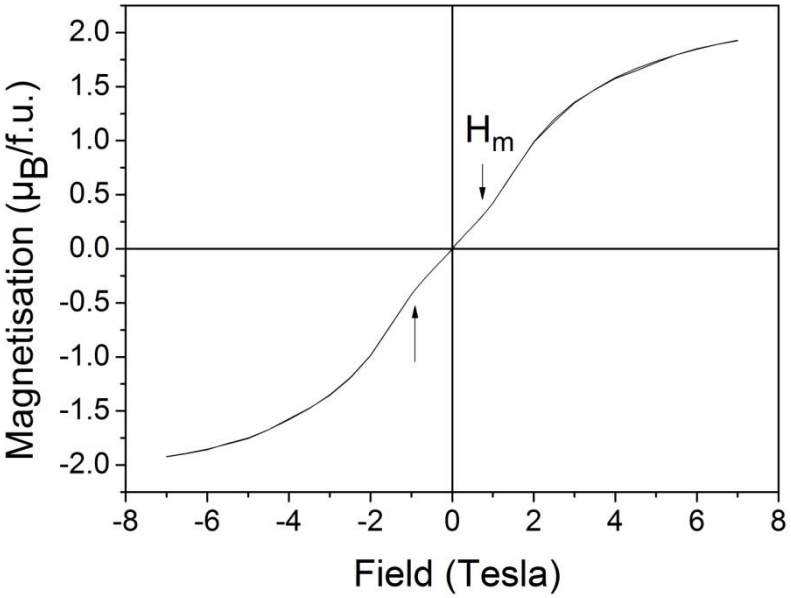


**Figure 6.10.** Hysteresis measured at 1.8 K for the columbite type high-pressure $NiV_2O_6$ showing a metamagnetic transition at $H_m$.

The metamagnetic transitions were further studied at higher temperatures of 3, 4, 5, 6 and 8 K (Figures 6.11 and 6.12). The measurements revealed some metamegnetism

up to 3 K but not at higher temperatures. In the expansion (Figure 6.12) the magnetic field where the metamagnetism starts is marked as $H_m$.

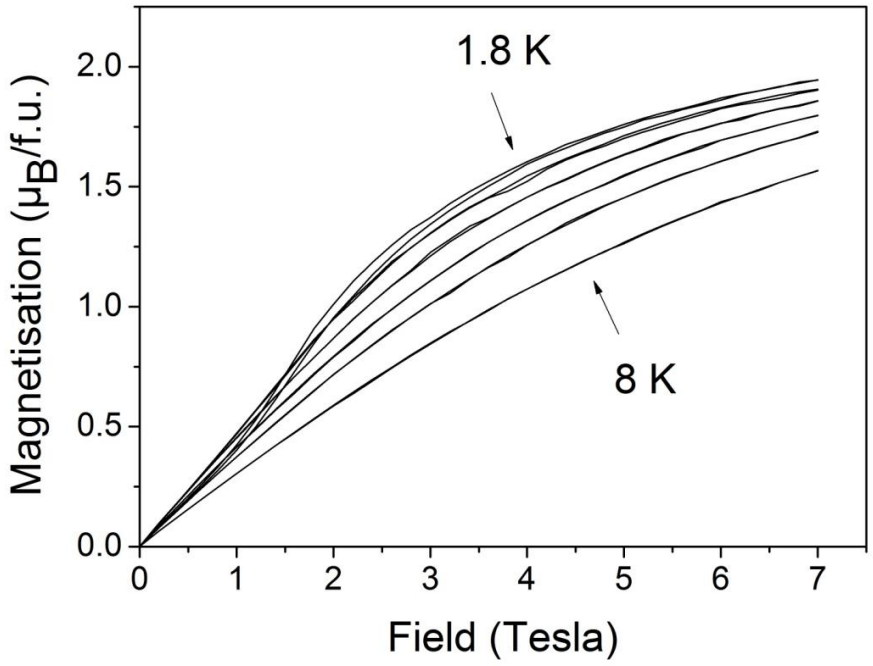


**Figure 6.11.** Hysteresis measured at 1.8, 3, 4, 5, 6 and 8 K (from top to bottom) for the columbite type high-pressure $NiV_2O_6$ showing the temperature dependence of the metamagnetic transition.

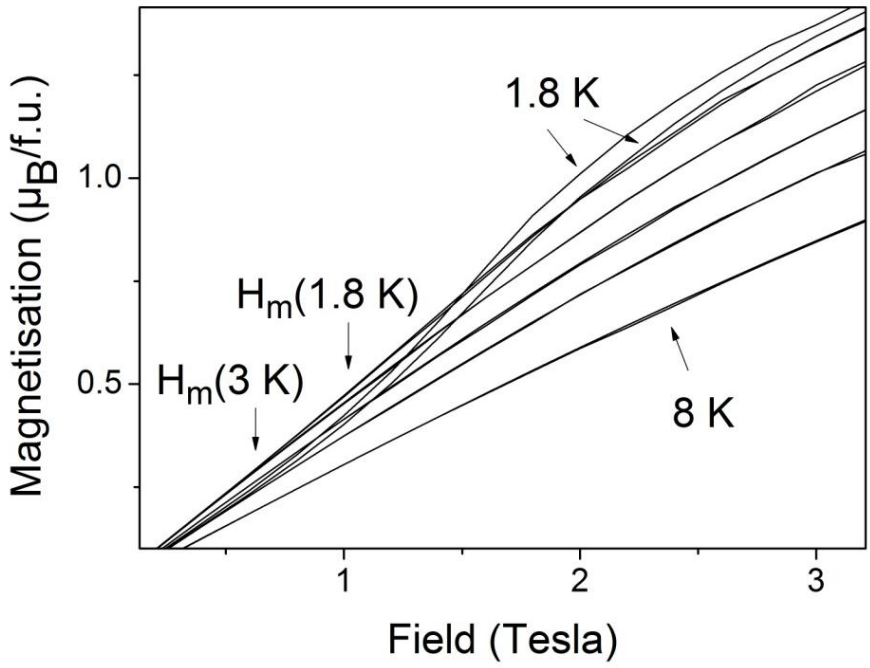


**Figure 6.12.** Expansion of the hysteresis measured at 1.8, 3, 4, 5,6 and 8 K (from top to bottom) for the columbite type high-pressure $NiV_2O_6$. The two arrows on the left end of the field-axis are showing the starting points of metamagnetism in different temperatures.

### 6.3.2. Neutron powder diffraction

**a) Zero-field measurements at instrument GEM**

The fits (Figures 6.13 and 6.14) to the data collected at base temperatures (1.6 K for $CoV_2O_6$ and 1.5 K for $NiV_2O_6$) did not reveal any magnetic peaks. Since the scans were long enough (~ 9 hours) for the observation of the possible magnetic peaks, it can be assumed that order of moments of normal magnitude does not exist in zero field. Refined lattice parameters, atomic coordinates and thermal displacement parameters for $CoV_2O_6$ and $NiV_2O_6$ are presented in Tables 6.1 and 6.2. Selected interatomic distances and bond angles can be found in Tables 6.3 and 6.4.

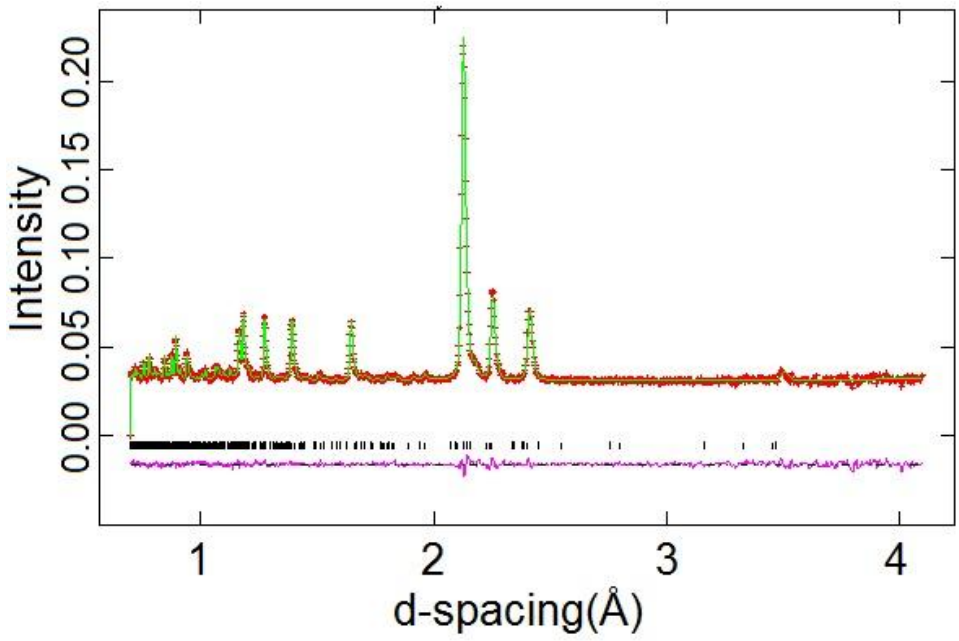


**Figure 6.13.** Fit to the neutron profile from the 63.6° detector bank of diffractometer GEM at 1.6 K for the columbite type $CoV_2O_6$.

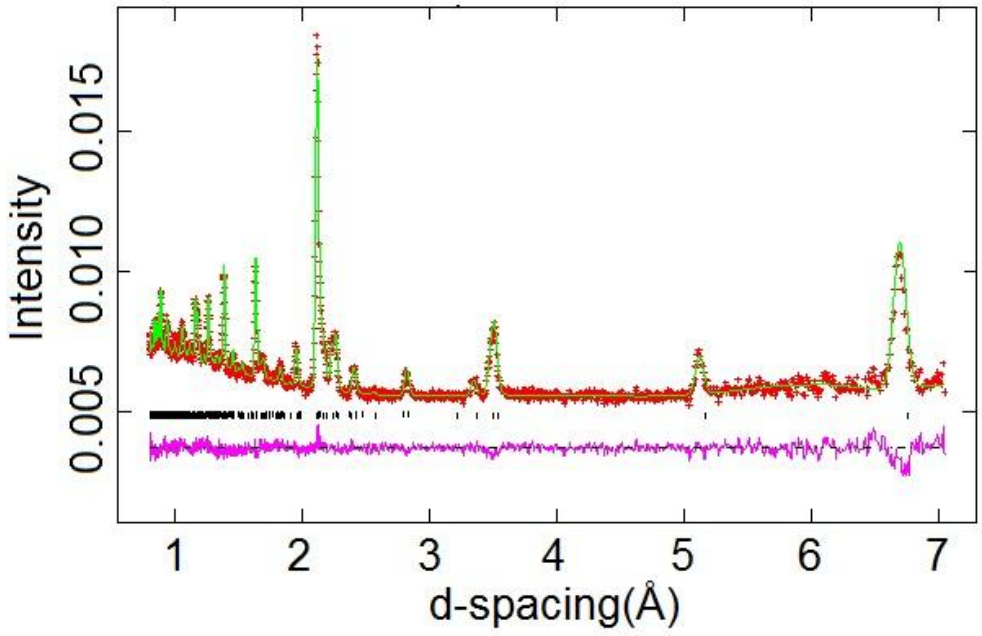


**Figure 6.14.** Fit to the neutron profile from the 35.0° detector bank of diffractometer GEM at 1.5 K for the columbite type $NiV_2O_6$.

**Table 6.1.** Refined lattice parameters, atomic coordinates and thermal displacement parameters from refinement of the $CoV_2O_6$ structure in space group *Pbcn* at 1.6 K (lower values) and 300 K (upper values). Fitting residuals, $R_{wp}$, and $\chi^2$, were 0.021 and 2.206 at 1.6 K and 0.028 and 0.913 at 300 K.

| a (Å) | b (Å) | c (Å) | Volume ($Å^3$) | |
|---|---|---|---|---|
| 13.4941(20) | 5.5736(9) | 4.8082(8) | 361.6(2) | |
| 13.4795(28) | 5.5689(12) | 4.8014(11) | 360.4(3) | |
| Atom | x | y | z | $U_{iso}$($Å^2$) |
| Co | 0 | 0.3186(20) | 0.25 | 0.0038(2) |
| | | 0.3235(23) | 0.25 | 0.0024(2) |
| V | 0.1590(32) | 0.1924(69) | 0.7469(108) | 0.0038(2) |
| | 0.1624(37) | 0.1869(75) | 0.7494(126) | 0.0024(2) |
| O(1) | 0.0967(2) | 0.1030(7) | 0.0544(8) | 0.0038(2) |
| | 0.0955(2) | 0.1065(7) | 0.0573(10) | 0.0024(2) |
| O(2) | 0.4153(3) | 0.1245(8) | 0.0987(8) | 0.0038(2) |
| | 0.4154(3) | 0.1251(90 | 0.0988(9) | 0.0024(2) |
| O(3) | 0.7549(3) | 0.1344(9) | 0.0829(12) | 0.0038(2) |
| | 0.7551(3) | 0.1319(10) | 0.0802(14) | 0.0024(2) |

**Table 6.2.** Refined lattice parameters, atomic coordinates and thermal displacement parameters from refinement of the $NiV_2O_6$ structure in space group *Pbcn* at 1.5 K (lower values) and 300 K (upper values). Fitting residuals, $R_{wp}$, and $\chi^2$, were 0.019 and 1.857 at 1.5 K and 0.023 and 0.953 at 300 K.

| a (Å) | b (Å) | c (Å) | Volume ($Å^3$) | |
|---|---|---|---|---|
| 13.3725(17) | 5.5344(7) | 4.8162(7) | 356.4(2) | |
| 13.3601(13) | 5.5278(6) | 4.8128(5) | 355.4(10) | |
| Atom | x | y | z | $U_{iso}$($Å^2$) |
| Ni | 0 | 0.3369(4) | 0.25 | 0.0044(4) |
| | | 0.3374(3) | 0.25 | 0.0034(3) |
| V | 0.1648(19) | 0.1941(46) | 0.7850(83) | 0.0044(4) |
| | 0.1640(15) | 0.1918(36) | 0.7785(71) | 0.0034(3) |
| O(1) | 0.0956(2) | 0.1076(5) | 0.0624(6) | 0.0027(2) |
| | 0.0953(2) | 0.1083(4) | 0.0633(5) | 0.0013(2) |
| O(2) | 0.4167(2) | 0.1284(6) | 0.1020(6) | 0.0027(2) |
| | 0.4169(3) | 0.1279(5) | 0.1012(5) | 0.0013(2) |
| O(3) | 0.7546(2) | 0.1295(7) | 0.0921(8) | 0.0027(2) |
| | 0.7546(2) | 0.1296(5) | 0.0909(6) | 0.0013(2) |

**Table 6.3**. Selected interatomic distances (Å) for orthorhombic $NiV_2O_6$ and $CoV_2O_6$ and from refinements at base temperature and 300 K. Mean distances are shown as <M-O>.

| $NiV_2O_6$ | 1.5 K | 295 K | $CoV_2O_6$ | 1.6 K | 300 K |
|---|---|---|---|---|---|
| Bond | Length (Å) | | Bond | Length (Å) | |
| Ni-O(1) × 2 | 2.008(3) | 2.015(3) | Co-O(1) × 2 | 1.994(8) | 2.008(7) |
| Ni-O(2) × 2 | 2.080(3) | 2.086(4) | Co-O(2) × 2 | 2.155(11) | 2.178(10) |
| Ni-O(2) × 2 | 2.032(2) | 2.037(4) | Co-O(2) × 2 | 2.046(4) | 2.054(4) |
| <Ni-O> | 2.040(3) | 2.046(4) | <Co-O> | 2.065(8) | 2.080(7) |
| V-O(1) | 1.713(32) | 1.690(40) | V-O(1) | 1.79(6) | 1.77(5) |
| V-O(1) | 2.160(19) | 2.190(23) | V-O(1) | 2.08(5) | 2.07(4) |
| V-O(2) | 1.700(28) | 1.712(34) | V-O(2) | 1.65(5) | 1.60(4) |
| V-O(3) | 2.176(24) | 2.172(30) | V-O(3) | 2.25(4) | 2.31(4) |
| V-O(3) | 1.683(20) | 1.657(24) | V-O(3) | 1.80(5) | 1.81(5) |
| V-O(3) | 2.113(29) | 2.142(35) | V-O(3) | 1.96(6) | 1.99(5) |
| <V-O> | 1.924(26) | 1.927(31) | <V-O> | 1.92(6) | 1.93(5) |

**Table 6.4.** Selected bond angles for orthorhombic $NiV_2O_6$ and $CoV_2O_6$ from refinements at 1.5 and 295 K ($NiV_2O_6$) and 1.6 and 300 K ($CoV_2O_6$).

| $NiV_2O_6$ | 1.5 K | 295 K | $CoV_2O_6$ | 1.6 K | 300 K |
|---|---|---|---|---|---|
| Angle | Degrees | | Angle | Degrees | |
| O(1)-V-O(1) | 87.1(9) | 86.5(11) | O(1)-V-O(1) | 87.2(20) | 87.5(18) |
| O(1)-V-O(2) | 102.7(11) | 102.7(14) | O(1)-V-O(2) | 101.6(25) | 104.6(23) |
| O(1)-V-O(3) | 79.5(12) | 79.8(15) | O(1)-V-O(3) | 75.6(18) | 73.8(15) |
| O(1)-V-O(3) | 104.2(16) | 106.3(20) | O(1)-V-O(3) | 96.6(28) | 96.4(24) |
| O(1)-V-O(3) | 154.9(11) | 153.7(14) | O(1)-V-O(3) | 156.2(24) | 153.5(22) |
| O(1)-V-O(2) | 86.5(10) | 85.2(12) | O(1)-V-O(2) | 91.6(24) | 93.1(21) |
| O(1)-V-O(3) | 74.0(6) | 73.4(7) | O(1)-V-O(3) | 75.9(13) | 74.6(12) |
| O(1)-V-O(3) | 159.2(12) | 158.5(15) | O(1)-V-O(3) | 160.2(25) | 156.6(21) |
| O(1)-V-O(3) | 72.0(8) | 70.7(9) | O(1)-V-O(3) | 76.4(19) | 75.7(16) |
| O(2)-V-O(3) | 160.3(12) | 158.3(15) | O(2)-V-O(3) | 167.2(30) | 167.6(27) |
| O(2)-V-O(3) | 107.5(12) | 107.9(15) | O(2)-V-O(3) | 106.5(22) | 108.1(21) |
| O(2)-V-O(3) | 90.0(15) | 88.8(18) | O(2)-V-O(3) | 96.1(28) | 96.7(25) |
| O(3)-V-O(3) | 90.7(11) | 91.7(13) | O(3)-V-O(3) | 86.2(20) | 84.3(16) |
| O(3)-V-O(3) | 81.5(7) | 81.0(8) | O(3)-V-O(3) | 83.7(16) | 82.0(13) |
| O(3)-V-O(3) | 92.3(11) | 92.1(14) | O(3)-V-O(3) | 93.5(23) | 91.7(20) |
| O(1)-Ni-O(1) | 101.77(13) | 101.94(16) | O(1)-Co-O(1) | 105.4(6) | 106.5(5) |
| O(1)-Ni-O(2) × 2 | 89.69(7) | 89.73(9) | O(1)-Co-O(2) × 2 | 88.53(16) | 88.35(14) |
| O(1)-Ni-O(2) × 2 | 94.89(8) | 94.92(11) | O(1)-Co-O(2) × 2 | 96.02(22) | 96.51(19) |
| O(1)-Ni-O(2) × 2 | 91.94(7) | 91.89(9) | O(1)-Co-O(2) × 2 | 93.71(21) | 94.10(18) |
| O(1)-Ni-O(2) × 2 | 168.44(10) | 168.21(13) | O(1)-Co-O(2) × 2 | 165.9(5) | 165.0(4) |
| O(2)-Ni-O(2) × 2 | 85.51(8) | 85.40(9) | O(2)-Co-O(2) × 2 | 82.64(31) | 81.95(28) |
| O(2)-Ni-O(2) × 2 | 86.14(9) | 86.24(12) | O(2)-Co-O(2) × 2 | 84.84(31) | 84.16(27) |
| O(2)-Ni-O(2) | 78.91(12) | 78.65(15) | O(2)-Co-O(2) | 77.6(5) | 76.9(4) |
| O(2)-Ni-O(2) | 169.17(16) | 169.19(21) | O(2)-Co-O(2) | 163.9(7) | 162.2(6) |

**b) Zero- and in-field measurements at instrument WISH**

Due to the small sample sizes the aluminum from the collimator gave very prominent peaks which needed to be removed from the data in order to get a good fit. Also, several spurious peaks were found and removed. Full Rietveld refinement of the structure was not possible due to the poor quality of the data (small samples and short scans) and the only aim of the fit was to solve the magnetic structure and refine the magnetic moments. The lattice parameters were fixed to the values taken from the refinement for the data from instrument GEM for the same samples. The magnetic structure was refined in the same *Pbcn* space group as the crystal structure.

Additional intensities were found for both compounds in all applied magnetic fields apart from the 0.1 T measurement for the $CoV_2O_6$. The existence of the magnetic peaks is shown clearly through the pictures generated on MantidPlot [15] software. The intensities were plotted against Q ($Q = 2\pi/d$) to make the differences between scans in various magnetic fields look distinct. Figures 6.15 and 6.16 present the plots for $CoV_2O_6$ and $NiV_2O_6$ respectively. For the $NiV_2O_6$ an illustrative plot was made by plotting the differences between various magnetic field and zero field neutron data rather than comparing directly the data in different fields.

To find out whether the additional intensities were due to the field texturing of the sample, reflections having the same orientation with the assumed magnetic peaks were searched for. Additional intensities should be seen at these reflections as well if they appear due to the field texturing. In the case of $NiV_2O_6$ the reflection at 3.35 Å having similar orientation (hkl 400) as the assumed magnetic peak at 6.6 Å (hkl 200) did not show greater intensity in magnetic field like the peak at 6.6 Å which proves that the additional intensity at 6.6 Å in field was not due to the field texturing of the sample. In the neutron diffraction profile of $CoV_2O_6$ there were no reflections having similar orientation to the assumed magnetic peaks and this proof of the origin of the additional intensities could not be acquired.

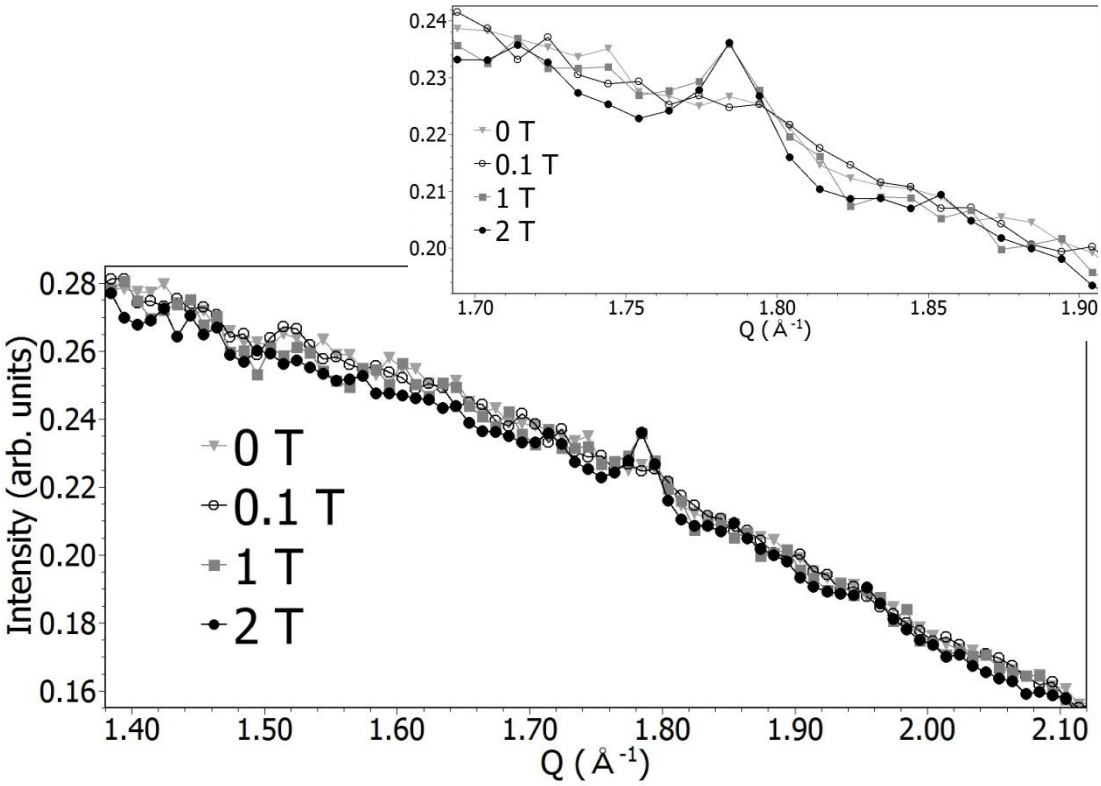


**Figure 6.15.** Intensities vs. Q for the neutron data from the 153° detector bank of diffractometer WISH for the orthorhombic $CoV_2O_6$ at 1.7 K in different magnetic fields. The smaller figure is showing an expansion of the Q range 1.7 – 1.9 $Å^{-1}$.

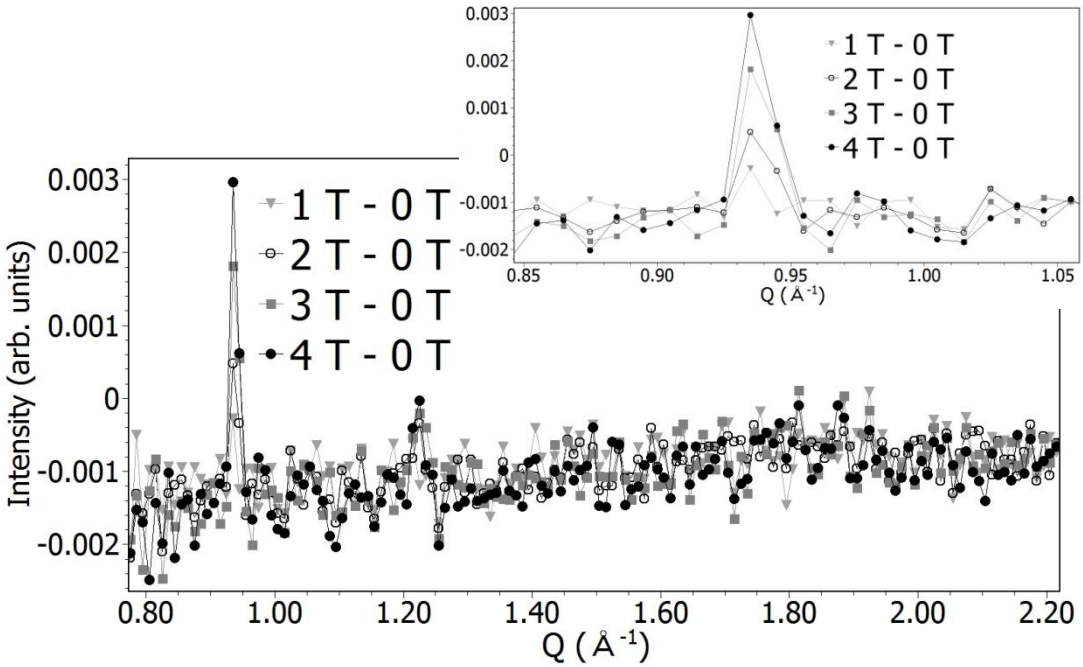


**Figure 6.16.** Intensities vs. Q for the differences between the intensities of various magnetic field and zero field neutron data from the 58° detector bank of diffractometer WISH for the orthorhombic $NiV_2O_6$ at 1.7 K. The smaller figure is showing an expansion of the Q range 0.85 – 1.05 $Å^{-1}$.

The fits to the neutron profiles at 1.7 K are presented in Figures 6.17 and 6.18. For $CoV_2O_6$ it was possible to get a reliable magnetic moment values only for the data measured at 2 T. This scan was considerably longer than those at 0.1 and 1 T and the quality of the data was better.

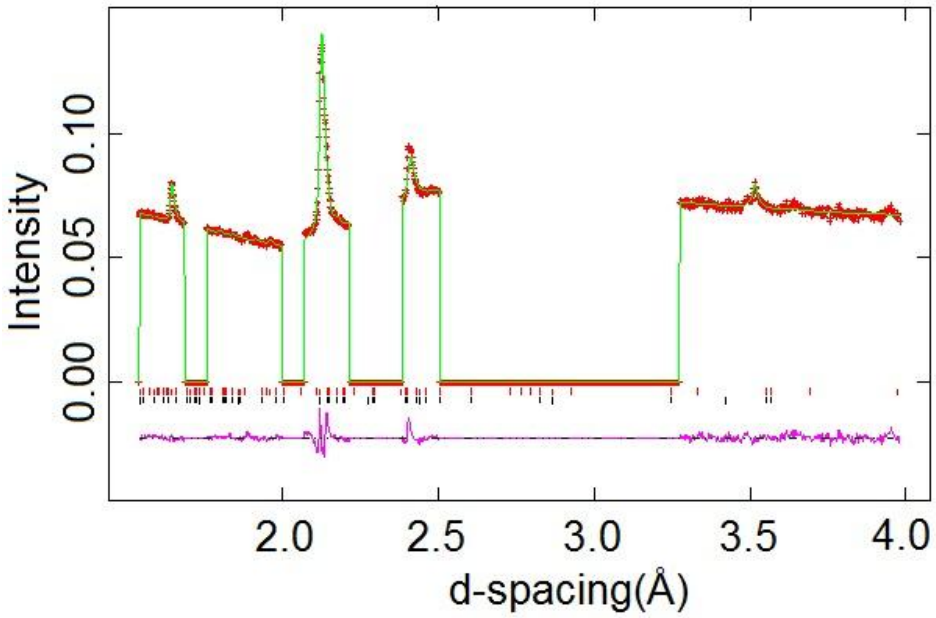


**Figure 6.17.** Fit to the neutron profile from the 153° detector bank of diffractometer WISH for the orthorhombic $CoV_2O_6$ at 1.7 K and 2 T showing crystal/magnetic structure reflection markers as lower/upper tickmarks. Parts of the profile had to be removed because they contain spurious scattering.

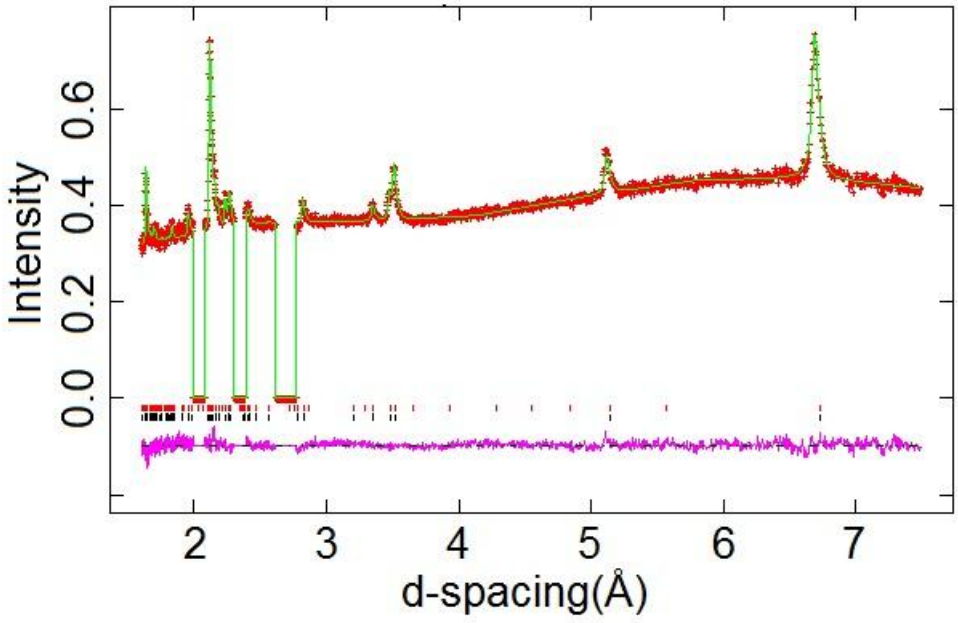


**Figure 6.18.** Fit to the neutron profile from the 58° detector bank of diffractometer WISH for the orthorhombic $NiV_2O_6$ at 1.7 K and 4 T showing crystal/magnetic structure reflection markers as lower/upper tickmarks. Parts of the profile had to be removed because it contained spurious scattering.

The models for the magnetic structures at various magnetic fields (Figures 6.19 and 6.20) were obtained by refining the data in different magnetic space groups derived from the *Pbcn* space group and choosing the one with the best goodness-of-fit values. For the magnetic structure of the $CoV_2O_6$ there were two equally good options (Table 6.5) exhibiting a canted magnetic structure (Figure 6.19). The fitting residuals $\chi 2$ and $R_{wp}$ were almost the same and so was the total magnetic moment. The model 1) on the left corresponds to the model 1 in table 6.5 and model 2) to the model 2 in the same table. The only difference between the models was that in the model 1 the moment along the a-axis was much bigger than the one along the c-axis ($m_a$ = 2.09 $\mu_B$, $m_c$ = -1.25 $\mu_B$) while in the model 2 the moment along the c-axis was bigger ($m_a$ = 1.16 $\mu_B$, $m_c$ = -2.23 $\mu_B$). Better quality data are needed to find out which structure is the real one.

In the case of $NiV_2O_6$ it was possible to determine the magnetic moments for all the different data sets. The only magnetic structure supported by the refinement results was a ferromagnetic order shown in Figure 6.20.

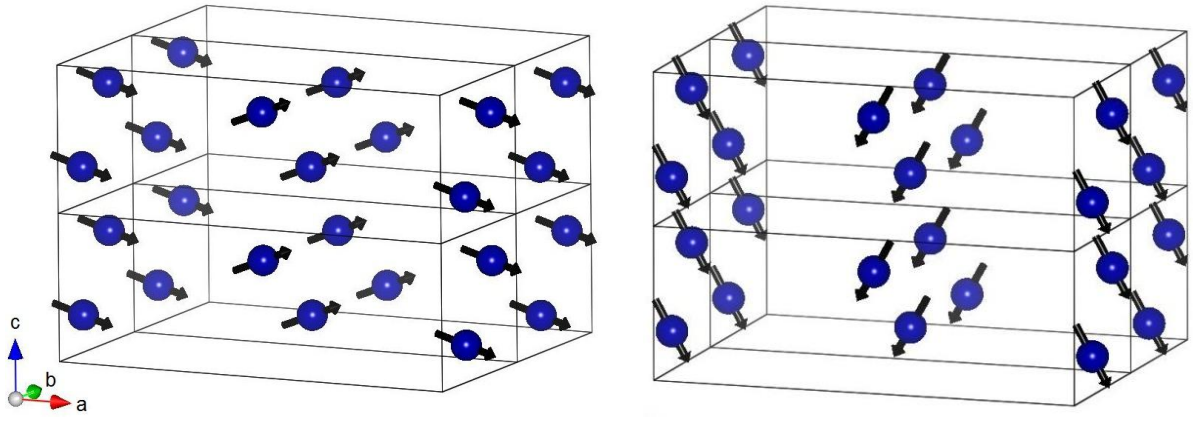


**1)** **2)**

**Figure 6.19**. The two options for the magnetic structure of the orthorhombic $CoV_2O_6$ at 2 T magnetic field.

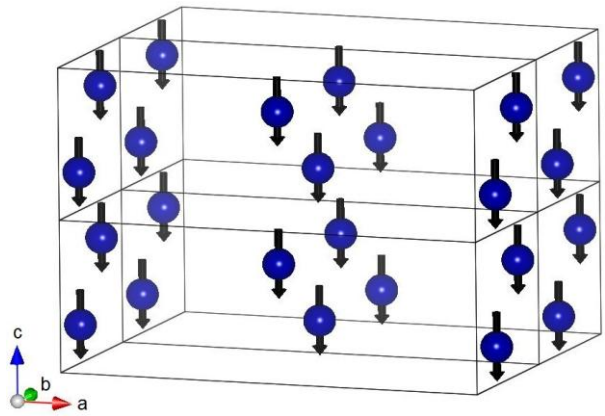


**Figure 6.20.** The magnetic structure of the orthorhombic $NiV_2O_6$ at magnetic fields of 1 – 4 T.

**Table 6.5.** Total magnetic moments and fitting residuals for the orthorhombic $CoV_2O_6$ and $NiV_2O_6$ in different magnetic fields.

| Magnetic field (Tesla) | total moment ($\mu_\beta$) | $\chi 2$ | $R_{wp}$ |
|---|---|---|---|
| $CoV_2O_6$ 2 T model 1 | 2.43(42) | 4.282 | 0.0224 |
| $CoV_2O_6$ 2 T model 2 | 2.52(41) | 4.380 | 0.0226 |
| $NiV_2O_6$ 4 T | 2.19(7) | 1.052 | 0.0167 |
| $NiV_2O_6$ 3 T | 1.86(11) | 2.111 | 0.0237 |
| $NiV_2O_6$ 2 T | 1.82(16) | 2.087 | 0.0235 |
| $NiV_2O_6$ 1 T | 0.86(15) | 1.261 | 0.0183 |

## 6.4. Discussion and conclusions

The magnetic transitions in orthorhombic high-pressure $CoV_2O_6$ and $NiV_2O_6$ take place at slightly lower temperatures than in their ambient pressure forms. Neither of the compounds exhibit 1/3 magnetisation plateaus which are present in their ambient pressure phases. The canted magnetic structures in orthorhombic $CoV_2O_6$ at 2 T magnetic field have also been observed for orthorhombic $FeNb_2O_6$ and $NiNb_2O_6$ [12]. The total magnetic moments achieved from the Rietveld refinements were on the same level with the values achieved in the magnetisation measurements, which were not yet quite saturated at 7 T. For $NiV_2O_6$ the total magnetic moments were getting bigger from 1 to 4 T measurements but not in a consistent manner. $V^{5+}$ ions have been described as being 5 + 1 coordinated in the monoclinic brannerites because the sixth oxygen atom is weakly bonded at distances of 2.4 - 2.8 Å [17], and as expected the mean V – O bond lengths in the orthorhombic high pressure $CoV_2O_6$ were shorter than in the monoclinic ambient pressure $CoV_2O_6$, 1.92 and 1.93 Å at 1.6 and 300 K compared to 1.96 and 1.97 Å at 4 and 300 K in the monoclinic phase. The Co – O bond lengths were similar in both phases.

The neutron diffraction studies in zero field confirm that high-pressure orthorhombic $CoV_2O_6$ and $NiV_2O_6$ adopt a columbite structure with a *Pbcn* space group. Ferromagnetic chains of $MO_6$ octahedra (M = Co or Ni) are running along the c-axis in zig-zag formation. Better quality data from neutron diffraction measurements in magnetic field are needed to resolve the inconsistencies in the results for spin orders.

## 6.5. References


1. B. Jasper-Tonnies and H. Muller-Buschbaum, Z. Anorg. Allg. Chem. **508**, 7 (1984).
2. M. Belaiche, M. Bakhache, M. Drillon, A. Derrory and S. Vilminot, Physica. B **305**, 270 (2001).
3. Z. He, J. Yamaura, Y. Ueda, and W. Cheng, J. Am. Chem. Soc. 131, 7554 (2009).
4. M. Lenertz, J. Alaria, D. Stoeffler, S. Colis and A. Dinia, J. Phys. Chem. C **115**, 17190 (2011).
5. S. A. J. Kimber, H. Mutka, T. Chatterji, T. Hofmann, P. F. Henry, H. N. Bordallo, D. N. Argyriou and J. P. Attfield, Phys. Rev. B **84**, 104425 (2011).
6. A. Le Bail, M.A. Lafontaine, European J. Sol. State Inorg. Chem. **27**, 671-680 (1990).
7. M. Gondrand, A. Collomb, J. C. Joubert and R. D. Shannon, J. Sol. State Chem. **11**, 1 (1974).
8. K. Mocala and J. Ziolkowski, J. Sol. State Chem. **69**, 299-311 (1987).
9. S. A. J. Kimber, Thesis: Spin and orbital ordering in ternary transition metal oxides. University of Edinburgh, (2008).
10. O. V. Nielsen, B. Lebech, F. K. Larsens, L. M. Holmes and A. A. Ballman, J. Phys. C: Sol. State Phys., **9**, (1976).
11. S. Klein and H. Weitzel, Acta Crystallogr. A **32,** 587 (1976).
12. C. Heid, H. Weitzel, F. Bourdarot, R. Calemczuk, T. Vogt and H. Fuess, J. Phys. Condens. Matter **8,** 10609–10625 (1996).
13. I. Yaeger and H. Morrish, Phys. Rev. B, **16** 5 (1977).
14. P. W. C. Sarvezuk, E. J. Kinast, C. V. Colin, M. A. Gusmao, J. B. M. da Cunha and O. Isnard, J. Appl. Phys. **109**, 07E160 (2011).
15. http://www.mantidproject.org/Main_Page
16. A.C. Larson and R.B. Von Dreele, Los Alamos National Laboratory Report no. LAUR 86-748 (1994) (unpublished).
17. M. Gondrand, A. Collomb, J.C. Joubert and R.D. Shannon, J. Solid State Chem. **11,** 1-9 (1974).

# Chapter 7. Conclusions and further work

Five different transition metal ternary vanadates have been synthesized and characterized. Apart from the monoclinic $CoV_2O_6$ all the compounds were made by high pressure synthesis.

In the $MnVO_3$ perovskite the unpaired d-electron of $V^{4+}$ gives rise to itinerant electron conductivity. In the other compounds vanadium is in a $V^{5+}$ oxidation state with an empty 3*d* shell, and as the d electrons in Co and/or Ni atoms are localized, these compounds are insulating.

Apart from the $MnVO_3$ all the structure types of the compounds are closely related. In the $CoVO_4$ and the orthorhombic $CoV_2O_6$ and $NiV_2O_6$ the $MO_6$ (*M* = Co or Ni or V) octahedra are in a zig-zag formation along the c-axis like in the α-$PbO_2$ type. In the monoclinic brannerite type $CoV_2O_6$ and the orthorhombic $CoV_2O_6$ and $NiV_2O_6$ the $MO_6$ (*M* = Co or V) octahedra are connected by chains of corner and edge sharing $VO_6$ octahedra but in the monoclinic $CoV_2O_6$ the $MO_6$ octahedra are in straight lines along the b-axis instead of being in zig-zag formation along the c-axis like in the orthorhombic $CoV_2O_6$ and $NiV_2O_6$. The $MnVO_3$ perovskite has Mn atoms in an unusual 8-coordination at the perovskite *A* site while the *B* site V is in an octahedral coordination like in the other compounds reported in this thesis.

Except for the $CoVO_4$ all the compounds have the *A*-site cation in a high spin state with unpaired *d* electrons and consequently they exhibit a low temperature magnetic order. In the monoclinic $CoV_2O_6$ the ferromagnetic chains are coupled antiferromagnetically to four neighbours and ferromagnetically to two in the quasi-triangular *ac*-plane packing of the brannerite structure. A Weiss temperature of 42.1 K shows that the strongest exchange interactions are ferromagnetic. Monoclinic $CoV_2O_6$ exhibits also an intermediate 1/3 magnetisation plateau that is not present in the orthorhombic $CoV_2O_6$. The magnetic order of the orthorhombic $CoV_2O_6$ and $NiV_2O_6$ appear only in an applied magnetic field. $CoV_2O_6$ has a field-induced canted antiferromagnetic structure and the Weiss temperature of - 30.1 K indicates that the dominant exchange interactions are antiferromagnetic. In case of the orthorhombic $NiV_2O_6$ a ferromagnetic order is observed in applied fields although the Weiss temperature was -17 K. In the $MnVO_3$ perovskite the incommensurate

antiferromagnetic order can be explained to arise from insulating superexchange and/or itinerant electron RKKY interactions.

Improving the synthesis of $CoVO_4$ would be the next important step for the study of this compound. Further experiments and calculations of the magnetic interactions would be needed to elucidate the physics of the $MnVO_3$ ground state in which the exchange interactions are likely to involve both Mn-O-Mn superexchange and RKKY coupling through the V d-band. Further intermediate magnetisation states may be found in higher applied magnetic fields in monoclinic $CoV_2O_6$. Better quality neutron diffraction data measured in magnetic field are needed to clear out the inconsistencies in the results for spin orders and magnetic moments in orthorhombic $CoV_2O_6$ and $NiV_2O_6$.

# Appendix

## A. Publications

The following articles related to the work reported in chapters 3 and 5 have been published:

Incommensurate spin order in the metallic perovskite $MnVO_3$
M. Markkula, A. M. Arevalo-Lopez, A. Kusmartseva, J. A. Rodgers, C. Ritter, H. Wu, and J. P. Attfield1, Phys. Rev. B **84**, 094450 (2011).

Neutron diffraction study of monoclinic brannerite-type $CoV_2O_6$
M. Markkula, A. M. Arevalo-Lopez and J. P. Attfield, J. Solid State Chem. **192** 390–393 (2012).

Field-induced spin orders in monoclinic $CoV_2O_6$
M. Markkula, A. M. Arevalo-Lopez and J. P. Attfield, Phys. Rev. B **86**, 134401 (2012).